Effects of Wide Range Bending Strain on Critical Current of Bronze Route Nb_3Sn Superconducting Strands

Submitted By
Joseph King

In partial fulfillment of the requirements for the degree of

MASTER OF SCIENCE IN MECHANICAL ENGINEERING

School of Engineering
Tufts University
Medford, Massachusetts

May 2012

Author: Joseph King
Department of Mechanical Engineering
Tufts University

Certified By: Dr. Luisa Chiesa
Assistant Professor
Department of Mechanical Engineering
Tufts University
Research Advisor

Certified By: Dr. Makoto Takayasu
Research Scientist
Plasma Science and Fusion Center,
MIT

Certified By: Dr. Gary Leisk
Lecturer and Research Assistant
Professor
Department of Mechanical Engineering
Tufts University

ABSTRACT

Superconducting Niobium-Tin (Nb_3Sn) plays important roles in magnet design for high energy physics and fusion reactor applications. Nb_3Sn is capable of carrying significant amounts of current and producing strong magnetic fields, making it an ideal choice for several components of the tokamak magnetic confinement system in the ITER experimental fusion reactor. Despite its great superconducting properties, Nb_3Sn demonstrates degraded electrical properties when subjected to strain. After being cabled into a Cable-in-Conduit Conductor, Nb_3Sn wires are subjected to a complex strain state during heat treatment and operation. The focus of this research was to examine a simpler subunit of the system by isolating the effects of pure bending strain on the critical current of a single Nb_3Sn strand. Though there are several processes for manufacturing Nb_3Sn wires, the samples tested in this study were bronze route wires from European Advanced Superconductors (EAS) and Hitachi Cable, Ltd.

Pure bending experiments with three distinct sample holders to cover a nominal bending range of 0.0-1.4% in a 4.2 K, 15 T environment at the National High Magnetic Field Laboratory were performed. Samples from both manufacturers exhibited critical current degradation as high as 60%, but this degradation was not permanent. Data analysis, additional test runs and finite element analysis concluded that multiple strain cycles did not further degrade critical current performance and that the sample holders accurately applied the desired strain to the Nb_3Sn wires.

ACKNOWLEDGEMENTS

The work done on this thesis would not have been possible without the help of several key individuals. First, my advisor Dr. Luisa Chiesa deserves my gratitude for her integral role, particularly her guidance and support throughout the entire process. I would also like to thank Dr. Makoto Takayasu for his help; his time, expertise and wealth of knowledge were major contributions to the research. I appreciate that both Dr. Chiesa and Dr. Takayasu were always available to answer my questions and to challenge me to offer my own insight. Dr. Gary Leisk provided a fresh prospective of the subject matter and my writing.

A few fellow graduate students were also very helpful during the research and writing process. Philip Mallon offered a great deal of help in the laboratory during the preparation phase that made the experiments run smoothly. His finite element modeling also provided a basis for the analysis performed in this research. Tiening Wang was always available to answer any questions I had regarding the ANSYS software package. David Bader offered invaluable constructive criticism and input during the writing and presentation process.

My mother, Kathi Keenan, and fiancée, Claire Carrabba, have my thanks for the countless sacrifices they have made for my sake.

This work was supported in part by the U.S. Department of Energy under GRANT DE-SC0004062. A portion of this work was performed at the National High Magnetic Field Laboratory, which is supported by NSF, the State of Florida and the DOE.

TABLE OF CONTENTS

LIST OF FIGURES

NOMENCLATURE

A –	amperes
B –	magnetic field
°C –	degrees Celsius
CICC –	Cable-in-Conduit Conductor
DAQ –	data acquisition
E –	electric field
EAS –	European Advanced Superconductors
FEA –	finite element analysis
ft –	feet
H_c –	critical magnetic field
HIT –	Hitachi Cable, Ltd.
hr –	hours
HTS –	high temperature superconductor
I –	current
I_c –	critical current
I_{c0} –	baseline critical current
J_c –	critical current density
K –	Kelvin
kg –	kilograms
km –	kilometers
l –	length
LTS –	low temperature superconductor
m –	meters
mm –	millimeters
Nb_3Sn –	Niobium-Tin
NbTi –	Niobium-Titanium
NHMFL –	National High Magnetic Field Laboratory
T –	tesla
T_c –	critical temperature
V –	volts or voltage
µV –	microvolts

Effects of Wide Range Bending Strain on Critical Current of Bronze Route Nb_3Sn Superconducting strands

1. INTRODUCTION

Niobium-Tin (Nb_3Sn) is a superconducting compound that is commonly used in magnet applications. Due to its high critical current and magnetic field properties, the Nb_3Sn investigated in this research has applications in the ITER experimental fusion reactor currently being developed and built in Cadarache, France. Despite its usefulness for high field magnets, Nb_3Sn has a major drawback in its sensitivity to strain. During manufacture and operation in cables, Nb_3Sn strands experience a variety of strains, including axial, transverse and bending. The focus of this research is the effects of bending strain on a single strand of Nb_3Sn manufactured by the bronze route process. This chapter will introduce superconductivity, the ITER project and various characteristics of Nb_3Sn superconductors.

1.1 Superconductivity

1.1.1 History of Superconductors

Superconductivity is the ability for a material to transport electric current without any resistive losses. The phenomenon was first discovered in 1911 by Heike Kamerlingh Onnes when he reduced the temperature of a mercury sample to the temperature of liquid helium, around 4 K, and noticed the resistance disappeared [1]. In the following decades, more superconducting materials were discovered and additional insight into the underlying principles of superconductivity was achieved.

Perhaps the next most significant advancement in the comprehension of

superconductivity was the proposal of the BCS (Bardeen-Cooper-Schrieffer) theory by Americans John Bardeen, Leon Cooper and John Schrieffer in their 1957 paper "Theory of Superconductivity" [2]. Proposed in the paper was the concept of electrons teaming up into Cooper pairs in the superconducting state. The idea was that the pairing of electrons would allow them to easily surpass obstacles, such as impurities, in the lattice structure. Though electrons are typically strongly repelled by each other due to their like charges, Cooper pairs are produced due to an electron-phonon interaction. When one electron passes by positively charged ions in the lattice structure, those positive charges are attracted to the passing electron, causing a lattice distortion with a greater local positive charge. This increased positive charge attracts a second electron and produces a Cooper pair. The electron pairing interaction is weak and easily broken by thermal energy, thus requiring cryogenic temperatures [3].

1.1.2 Behavior of Superconductors

Superconducting materials exhibit no electrical resistance only when certain criteria are met. Critical current density (J_c), critical temperature (T_c) and critical magnetic field (H_c) are the maximum value criteria that define superconductivity. The criteria are considered to create a critical surface under which conditions must be under for superconductivity. See Figure 1 for a graphical representation of this concept for two common superconductors, Nb_3Sn and Niobium-Titanium (NbTi).

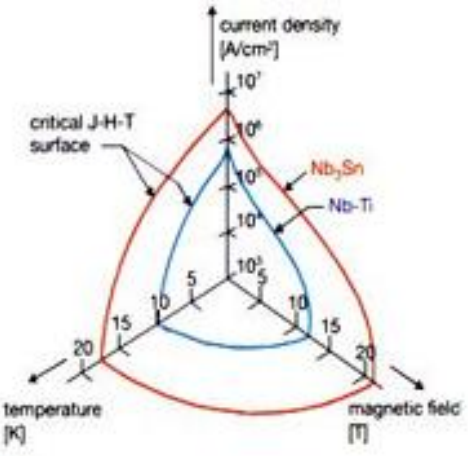

Figure 1 - Critical Surface for Common Superconductors [4]

The critical temperature of superconductors is used to divide superconductors into two different classifications: low temperature superconductors (LTS) and high temperature superconductors (HTS). The idea of 'high temperature' is a relative term as no known superconductors have a critical temperature near room temperature. HTS conductors have critical currents above the boiling point of liquid nitrogen at atmospheric pressure, 77 K. LTS have critical temperatures lower than that point; a bath of liquid helium, with a boiling point of 4.2 K at atmospheric pressure, is commonly used to easily maintain temperatures below the critical temperature of an LTS.

Another categorizing characteristic of superconductors is the ability or inability to fully exclude the penetration of magnetic flux. The Meissner effect describes this behavior difference between superconductors and perfect conductors. When a superconductor is lowered below its critical temperature, it will cancel any applied magnetic field, regardless if that field is applied before or after the temperature reduction. This occurs with superconductors because the external

field induces a surface current that produces an internal field that perfectly counteracts the applied external field. As seen in the two left columns of Figure 2, perfect conductors would internally exclude the field if it is applied after the temperature reduction; if it is applied before the temperature is reduced, a perfect conductor would retain the magnetic field even after the external field is removed. See Figure 2 for a diagram of the Meissner effect, where B and the associated lines represent the magnetic field.

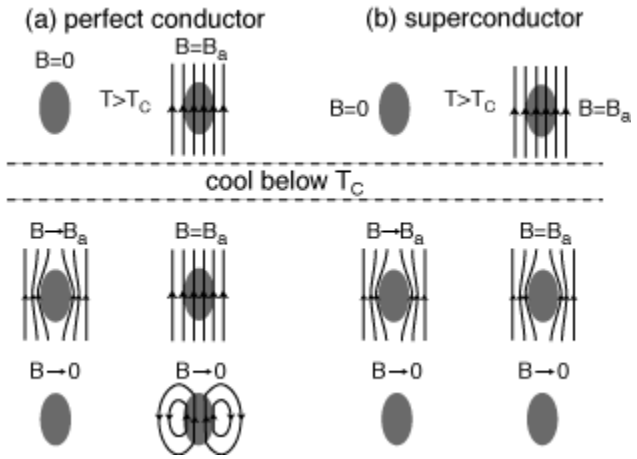

Figure 2 - Meissner Effect [5]

Although the Meissner effect applies to all superconductors, the manner in which the effect manifests itself at high fields defines two types of superconductors. Type I superconductors have a single critical field value, H_c, which is less than 1 T, at which point the Meissner effect completely breaks down and superconductivity is lost, returning the material to the resistive or normal state. Type II superconductors, on the other hand, have two critical field values, H_{c1} and H_{c2}. Below H_{c1}, the superconductor exhibits perfect magnetic flux exclusion. Above H_{c1} but below H_{c2}, known as the mixed state, partial flux penetration

occurs, but superconductivity is maintained. Above H_{c2}, which is an order of magnitude greater than H_c, superconductivity is lost. The increase in critical field range makes Type II superconductors much more applicable for magnet applications. Figure 3 and Figure 4 plot the difference between Type I and Type II superconductors.

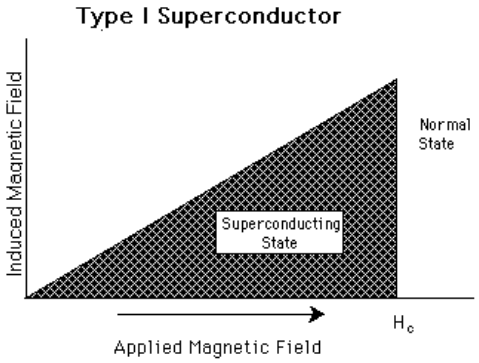

Figure 3 - Type I Superconductor [3]

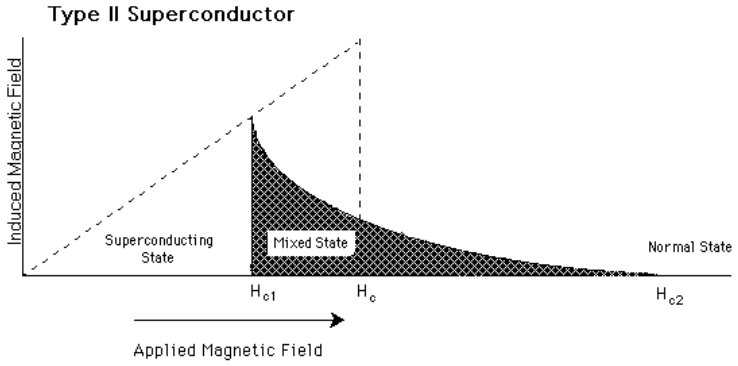

Figure 4 - Type II Superconductor [3]

1.2 Nb_3Sn Superconductors

Nb_3Sn is a Type II LTS with a critical temperature of 18.2 K and a critical field (H_{c2}) of 24.5 T at 4.2 K. Its high critical field at liquid helium temperatures makes Nb_3Sn an attractive option for magnets for high energy physics and fusion

applications. Another commonly used superconductor for magnets is NbTi, but Nb_3Sn outperforms NbTi in all three critical criteria, allowing for greater current densities and magnetic fields. The major drawback to Nb_3Sn superconductors is its sensitivity to strain, showing degraded critical current performance with applied strain, a characteristic that NbTi does not share. The potential performance advantages of Nb_3Sn if strain effects can be minimized make the superconductor a key focus of research.

Unlike typical wires, Nb_3Sn has a complex and variable design. Large 40-100 kg billets of the desired cross sectional design are produced, and then drawn into 10-30 km long wires of the desired diameter. The Nb_3Sn wires studied in this research have a diameter of 0.82 mm. See Figure 5 for an example of a Nb_3Sn billet before being drawn. The cross-section design and materials in the billets vary by the manufacturing process and company.

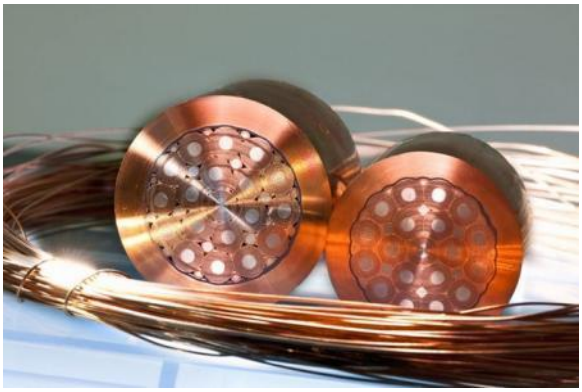

Figure 5 - Nb_3Sn Billet Example [6]

These billets and subsequently drawn wires do not yet contain the superconducting Nb_3Sn compound. For the superconducting compound to chemically form, the wires must undergo a heat treatment with temperatures as

high as 650 °C. Once heat treated, the wire becomes very brittle and sensitive to strain.

Several different approaches exist to produce the Nb_3Sn superconducting filaments within the wires. Bronze route, internal-tin and powder-in-tube are the most common manufacturing techniques, but there are others. In all cases, the differences are in the composition of the billets and wires. Bronze route samples provided by European Advanced Superconductors (EAS) and Hitachi Cable, Ltd. were tested in this research. Superconducting Nb_3Sn wires can have a wide range of performance characteristics depending on which manufacturing technique was used.

Bronze route Nb_3Sn strands are made with a series of niobium filaments within a bronze matrix in the filament area. The filament area is surrounded by a diffusion barrier and an outer layer of copper. The bronze matrix, an alloy of tin and copper, provides the tin necessary to react with the niobium to form the superconducting Nb_3Sn filaments. It also acts as a structural component for the wire. An example of a schematic of a bronze route wire is shown in Figure 6.

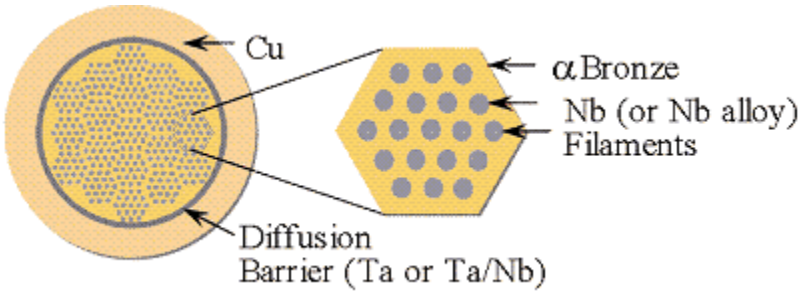

Figure 6 - Schematic of Bronze Route Nb_3Sn Wire

The cross-section shown in Figure 6 would be drawn to the desired wire diameter. The final step in producing a bronze route Nb_3Sn superconductor is the heat treatment process. Exact specifications for heat treatment can vary by manufacturer, but typically temperatures typically exceed 600 °C and the entire heat treatment process can take 500 hours or longer.

1.3 ITER

The importance of determining the performance characteristics of Nb_3Sn superconductors ultimately depends on the applications of the technology. The driving motivation behind this research is for the experimental fusion reactor being designed and constructed by ITER.

The ITER fusion reactor is an experimental device currently under development. The project is a multinational effort that includes the cooperation of the European Union, United States, Russia, China, South Korea, Japan and India. The long term goal of the ITER reactor is to prove the feasibility of large scale fusion power plants. After the conclusion of the 10 year construction phase, around 2020, the plan is to begin a 20 year lifecycle with new fusion reactor plants being implemented by 2050 [7]. A cut-away schematic of the nearly 30 m tall ITER reactor is shown in Figure 7.

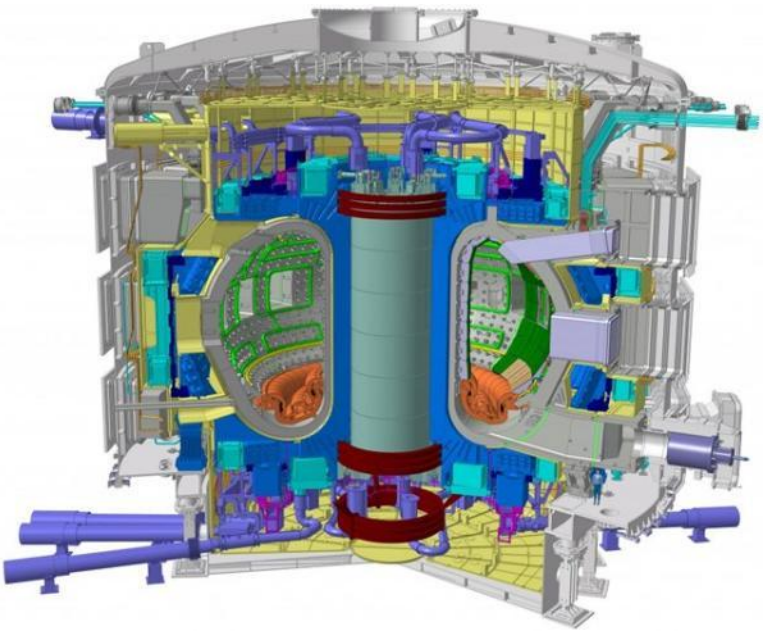

Figure 7 - Cutaway View of ITER Experimental Reactor [6]

The ITER reactor design utilizes magnetic confinement to contain and heat plasma to achieve fusion ignition. A tokamak, or toroidal magnet system, uses a series of pulsed magnets to confine plasma at temperatures on the order of 10^8 K. Some of these magnets use NbTi cables, while others, most notably the central solenoid, use a Nb_3Sn cable-in-conduit conductor (CICC), shown in cross-section in Figure 8. The cross sectional dimension of the CICC is on the order of 45 mm.

Figure 8 - CICC Cross-section [4]

The CICC design for the central solenoid magnets of the ITER fusion reactor consists of more than 1000 strands. More than 800 superconducting strands, mixed with pure copper strands, are cabled into progressively larger subcables until the final CICC is created. The final cabling stage wraps six petal shaped subcables around a steel spring central channel. The channel provides a means for liquid helium to be forced to flow through as a coolant. The final step of CICC production is wrapping the entire cable in a stainless steel 316 jacket. See Figure 9 for a photograph of the cabling stages.

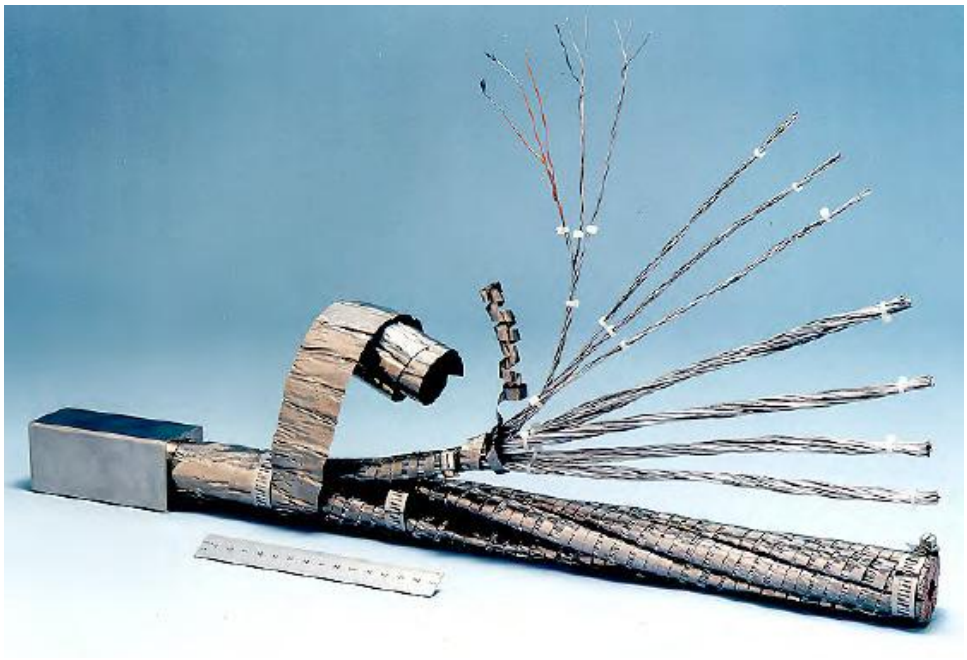

Figure 9 - CICC Cabling

The geometry of the CICC has the benefit of bundling a large quantity of superconducting strands while providing mechanical support and cooling. The strain state that exists during operation, however, is made complex by the interaction of many cabled strands. Since Nb_3Sn is sensitive to strain, accurately determining the strain state during operation and its effect on the performance of Nb_3Sn is critical for the design of dependable magnets for ITER.

1.4 Strain

Since the CICC configuration creates such a complicated series of interaction among over 1000 wires and the surrounding materials, simply analyzing a full cable is not feasible. Instead, the problem must be simplified to understand the underlying behaviors of the Nb_3Sn strands. This can be accomplished by isolating types of loading as well as single strands or subcables. Testing single strand samples of the superconductor is the simplest subdivision and can be

expected to provide a basis for scaling results up to a full CICC configuration. Experiments and analysis can then be expanded to a three strand subcable, a configuration that is still simple compared to larger subcables, but that introduces cabling effects that may not be possible to analyze for a single strand.

The loading that a single strand may experience during operation in a CICC needs to be determined. Two important things to consider are the loading and support on any strand. The main source of loading during operation is the Lorentz force due to the interaction of current and magnetic field. The Lorentz force acts on the CICC perpendicular to both the current and magnetic field. The strands in the CICC are supported by other strands at some points, by the jacket or central spring at others. Within the cabling, there are portions of the strands that are unsupported, as shown as a schematic in Figure 10. In Figure 10, F represents the Lorentz force, L represents the spacing caused by cabling and *f* represents a frictional component. At the unsupported points it becomes clear that the strands experience bending strain. Also present are axial strain and transverse strain, caused by thermal contraction and a Lorentz force that result in strands being compressed between other strands.

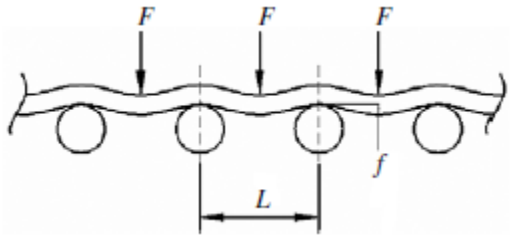

Figure 10 - Schematic of Loading [8]

1.5 Thesis Objective and Scope

The primary goal of this thesis is to perform pure bending tests across a range of 0.0-1.4% nominal bending strain on single strand bronze route Nb_3Sn samples from two manufacturers and analyze the critical current results. Nominal bending strain values were calculated at the surface of single strand test samples as the ratio of the wire radius to the radius of curvature. Samples from European Advanced Superconductors (EAS) and Hitachi Cable, Ltd. were tested in this study. The results contribute to the understanding of bending strain effects on bronze route Nb_3Sn wires and may be useful in developing empirical models of these effects.

A second significant aim of this research is to establish a preliminary investigation into the performance of the test's sample holders. Due to extreme operating conditions of 4.2 K and 15 T and the inability to directly measure strain, experimental data analysis and finite element analysis are two tools used in this research to better understand the strain state imparted on the test strands by the sample holders. The scope of this thesis includes the first steps toward possible design revisions of the sample holders in subsequent research efforts.

2. PURE BENDING EXPERIMENTS

In recent years, pure bending experiments have been run using various test fixtures and superconducting wire types. This chapter will describe some of these experiments and outline the test apparatus and procedure for the experiments run for this research. All the experiments to be described in this chapter were designed for and run in the 190 mm bore 20 T resistive magnet at the National High Magnetic Field Laboratory (NHMFL) in Tallahassee, Florida.

2.1 Previous Experiments

Harris first designed a pure bending experiment in 2005 [9]. The probe, gearing and general procedure from his experiment comprise the basis of the experiments run for this research. The probe was a structural component that centered the experiment in the magnet at the NHMFL. The probe contained all necessary components to control the experiment from outside the cryogenic environment of the testing area, including an input shaft and leads for the input current and voltage taps for measurements. A schematic is shown in Figure 11.

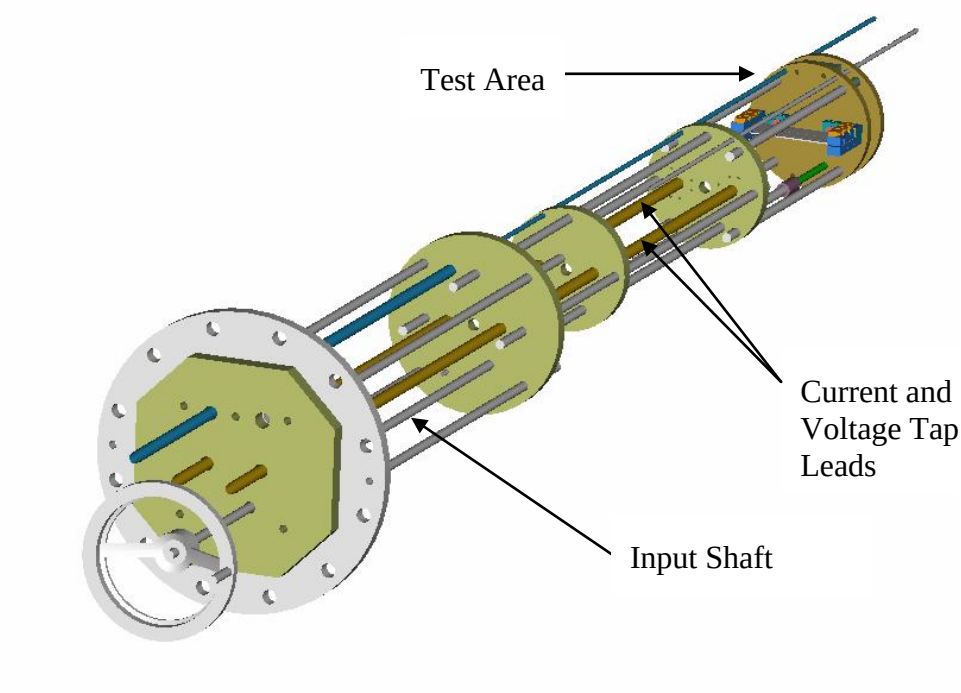

Figure 11 – Harris's Probe Design [9]

The testing area consisted of a gearing system and sample holder that deformed the superconducting samples in a pure bending fashion. The concept of the system was to rigidly connect the sample holder to two arms that would rotate symmetrically. The offset between the ends of the sample holders and the axes of

rotation allowed the sample to purely bend without also being subjected to tension. The gearing transmits rotation from the input drive shaft to the two torque shafts used to deform the sample holder. In Harris's design, the sample holder was a plate with three notches to hold test samples. The notches allowed for the test samples to be positioned along the neutral axis of the plate, minimizing tension or compression of the samples. The plate would support the samples against the Lorentz force during testing [9]. Figure 12 is a representation of Harris's test area design.

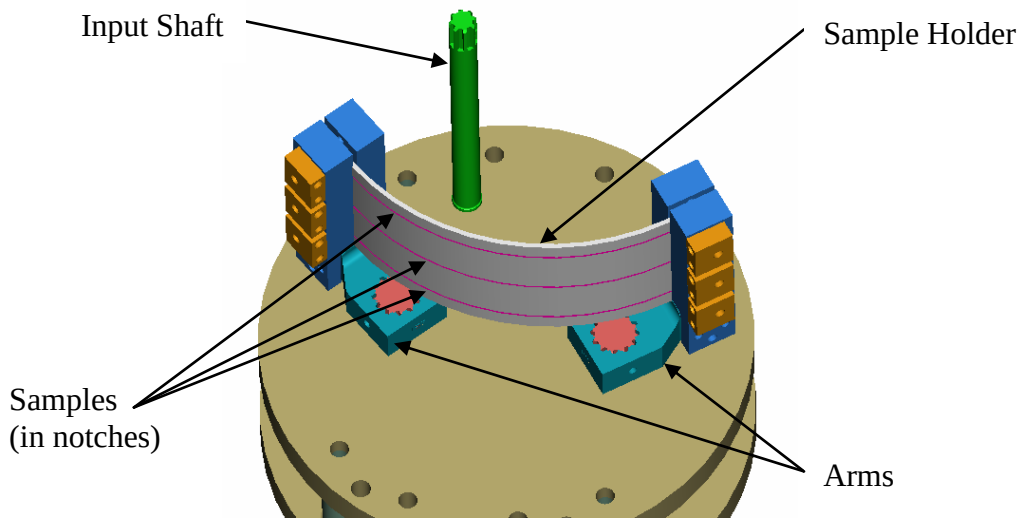

Figure 12 - Harris's Test Area [9]

One drawback to Harris's sample holder design was that the maximum allowable bending strain was 0.7% due to the sample holder's required thickness. Applying bending strain beyond this amount would have resulted in the sample holder yielding [9].

A significant design alteration was made in 2006 by Allegriti after the first tests performed with Harris's design showed degradation caused by axial strain and not

only pure bending [10]. The new design featured sample holder beams that held two superconducting samples each in channels along the top and bottom of the beam, assuring that the samples would be placed along the sample holder's neutral axis. In creating a channel along the top and bottom of the beam, the thickness required to counteract the Lorentz force during operation increased. To avoid thickening the entire sample holder and severely limiting its bending range, the sample holder was kept thin, but with the addition of regularly spaced ribs. The ribs provided the support against the Lorentz force, while the rest of the thin sample holder beam allowed for the maximum bending strain to be maintained at 0.7%. The symmetric nature of Allegriti's sample holder meant that they could support the samples against a Lorentz load regardless of the current direction. The new design also allowed for four samples to be mounted on the gear box instead of three. Minor alterations to the probe were needed to accommodate the additional sample [10]. See Allegriti's sample holder design in Figure 13.

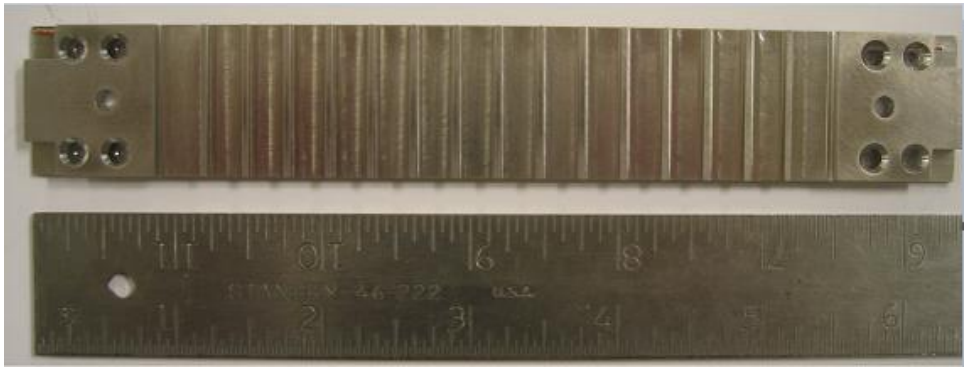

Figure 13 - Allegriti's Sample Holder [10]

Despite the design revision, the problem of a limited bending range still existed. In 2011, Mallon implemented design changes to alter the range of bending strain, including allowing a maximum bending strain of 1.4% [11]. In order to

accomplish this, Mallon introduced two new sample holders to complement Allegriti's design. The three sample holders were designed to cover three separate bending ranges of 0.0-0.7%, 0.4-1.1% and 0.7-1.4%. The exact range of operation was dependent on current and magnetic field, since these two factors determined the Lorentz load that the sample holders needed to react.

The low bending sample holder, 0.0-0.7% bending strain, was Allegriti's design, while the medium and high bending sample holders were modifications of that design. The medium bending sample holder, 0.4-1.1%, was simply a thinner version of the low bending range, with the same ribs, but thinner channel walls to allow for more bending strain but to avoid plasticity of the sample holder. The high bending sample holder, 0.7-1.4%, completely removed the channel wall, using only the ribs to support the samples against the Lorentz force. For the medium and high bending range sample holders, the minimum bending strain was estimated based on expected current and magnetic field. At lower strain values, the critical current of the samples is higher, resulting in a larger Lorentz force than at higher bending strain values [11]. Due to variability among different Nb_3Sn strands, the low ends of the allowable ranges are not universal, but the design guidelines were for a strand with a critical current of 350 A at 12 T (4.2 kN/m). See Figure 14 for a SolidWorks model of Mallon's high bending sample holder.

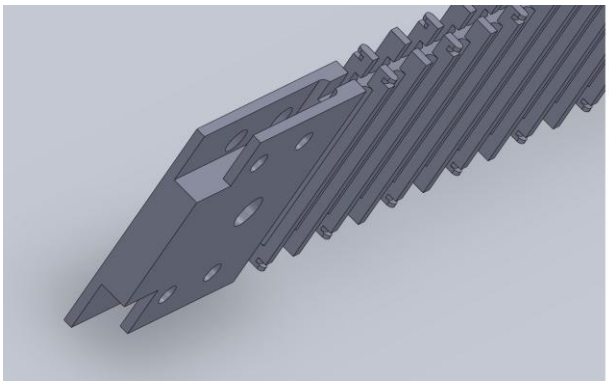

Figure 14 - Mallon's High Bending Sample Holder [11]

2.2 Current Experiments

The current round of pure bending experiments used the sample holder and probe modifications from Mallon's experiments, but tested samples of the bronze route manufacturing process as opposed to internal tin samples that Mallon tested. Beyond the addition of electrical leads for current input and voltage measurements, the most significant change to the probe since Harris's experiments was the addition of a motor and encoder system to replace the original hand crank.

The originally scheduled experiments spread across eight days at the NHMFL during August 2011 with tests being run on three of those days and the rest being used for preparation. Each testing day was dedicated to a different bending range. Critical current measurements were performed as a function of bending strain at fixed magnetic field (12-15 T) and fixed temperature (4.2 K). The first day of testing used the low bending sample holder to test the 0.0-0.7% bending strain range; the second test day used the medium bending sample holder to test the 0.4-1.1% range; the final day used the high bending sample holder to test the 0.7-

1.4% range. Preparation, which will be explained in detail in the next chapter, consisted of readying and mounting the Nb_3Sn samples, the sample holders and the probe. A testing day comprised of applying bending strain to the samples via the motor and gear box, ramping up the current to each sample, one at a time, and recording the voltage readings from two voltage taps per sample to determine the critical current from the voltage transition from the superconducting to resistive state. The applied bending strain was typically increased at 0.1% strain increments by using the motor to apply a known rotation to achieve the desired bending strain. After increasing the applied strain a few increments, the strain was lessened and additional measurements were performed to try to detect any permanent critical current degradation. Critical currents were estimated in real time during testing by detecting when voltages crossed values representative of industry standards for electric field criteria. More on this will be explained in chapter 4.

In addition to the original three testing days, a second trip was made to the NHMFL in January 2012 for an additional day of testing with the high bending sample holder. As will be explained in chapter 5, this series of tests were used to learn more about the performance of the high bending sample holder. Tests for this day included the full 0.0-1.4% bending range, rather than the original design range of 0.7-1.4%, as well as a series of runs with a reversed current direction. These two modifications helped improve the understanding of how significantly the Lorentz force affected the samples and sample holders.

3. EXPERIMENT PREPARATION

The experimental setup consisted of two sample holders mounted to a gear box on the end of a probe. This chapter will break down the preparation for the experiments into separate sections for each of those three subsystems of the test setup and final miscellaneous preparations. A description of the individual parts, their roles and required preparation are included.

3.1 Sample Holders

Included in the scope of the preparation of the sample holders are the sample wires from EAS and Hitachi, the sample holder beams and all the necessary pieces to complete the process.

3.1.1 Sample Holder Components

In addition to the sample holder itself, two other key components, copper current terminators and copper current leads, were needed for the tests. A prepared sample holder that includes the current terminators and leads can be seen in Figure 15. The copper current terminators were the same as the design for previous bending experiments run by Mallon. The U-shaped terminator was designed to increase the length of the interface between the terminator and superconducting wire. A SolidWorks representation of the current terminator is shown in Figure 16. Cabled copper current leads transferred the current to the terminators from an external power supply via leads mounted on the probe.

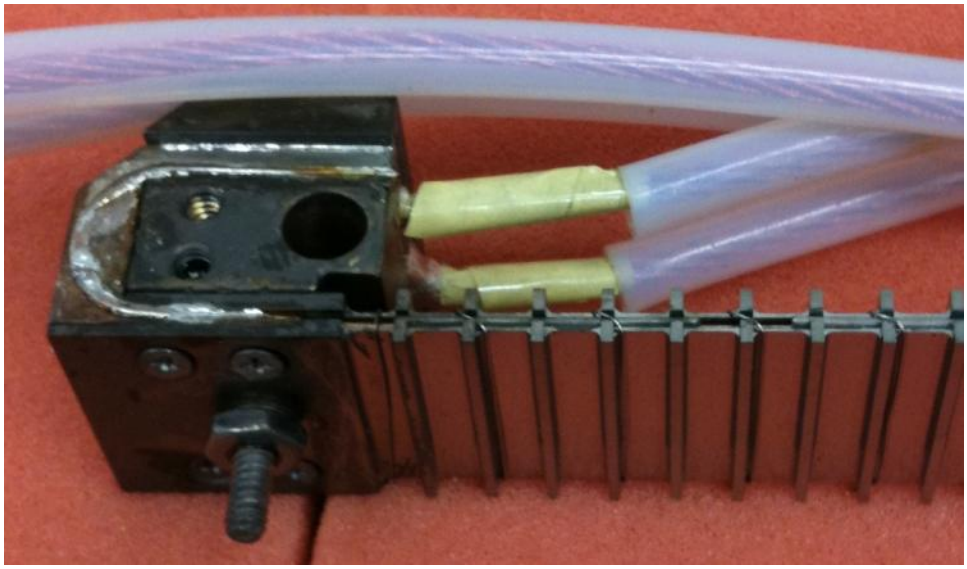

Figure 15 - Sample Holder with Current Terminators and Leads

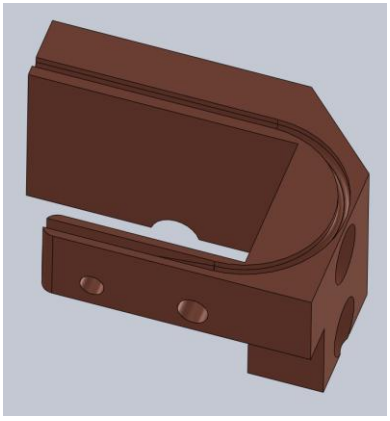

Figure 16 - Copper Current Terminal

Beyond the sample holders, current leads and current terminators, several auxiliary components were required to hold the samples in place for heat treatment and other preparations. These parts were specifically a copper spacer, a stainless steel cover plate and a stainless steel backing plate. The copper spacers fit inside the copper current terminators, where the gear box arms would be during testing. More information on the gear box arms can be found in the gear box preparation section. The copper spacers provided additional structural strength

during heat treatment and a location for a cartridge heater for soldering procedures that will be explained later. After heat treatment and soldering, the copper spacers were removed. See Figure 17 for a SolidWorks model of the copper spacer.

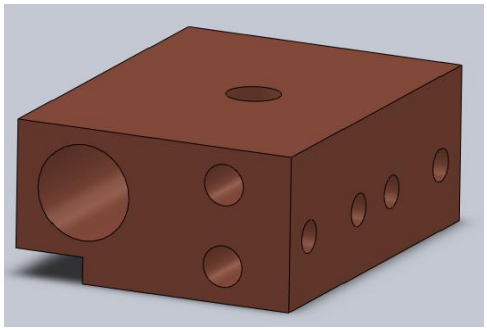

Figure 17 - Copper Spacer

The stainless steel cover plates fit on top of each of the copper current terminal blocks to hold the Nb_3Sn sample in the channel during heat treatment. The cover plates were removed after heat treatment. The stainless steel backing plates helped hold the current terminals in place during both heat treatment and testing. They were removed during soldering, but put back in place after mounting the sample holders onto the arms. The stainless steel cover plate and backing plate are shown as SolidWorks models in Figure 18.

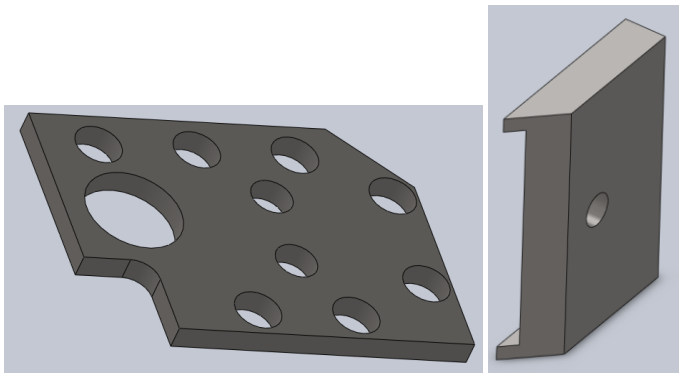

Figure 18 - Stainless Steel Cover Plate (left) and Backing Plate (right)

3.1.2 Sample Holder Preparation

With all necessary components identified, the first step in preparation was to thoroughly clean all the parts, especially those that would be involved in the heat treatment phase. Several of the parts were then given a thin graphite coating to prevent various parts from potentially fusing together. All faces of the current terminators and the stainless steel cover plates and backing plates were covered; the inside of the sample holders' channels and all their faces that mated with the current terminators were coated; all the surfaces of the current terminators that mated with the sample holders, backing plates and copper plates were also coated. The channels and holes of the current terminators where they mate with the superconducting samples and current leads, respectively, were kept free of the graphite coating, otherwise it would have been difficult to solder the samples to the current leads following heat treatment. With tight size tolerances on the parts, it was imperative that the graphite coatings be kept thin to ensure that the parts could easily fit together and be removed when necessary without damaging the superconducting wires.

Preparation of the samples spanned a couple of weeks plus the time necessary for heat treatment. The bronze process Nb_3Sn wires arrived as unreacted wire from EAS and Hitachi. Since the wires are far less brittle and sensitive to strain before heat treatment, they needed to be mounted into the sample holders and then heat treated. Despite the better ductility prior to heat treatment, great care was taken to minimize unnecessary deformation of the samples that could cause damage.

The next step was to assemble the sample holders. The first stage of this process was to simply connect the current terminals to the sample holders. A SolidWorks representation of one current terminal placed in its location in a sample holder is shown in Figure 19.

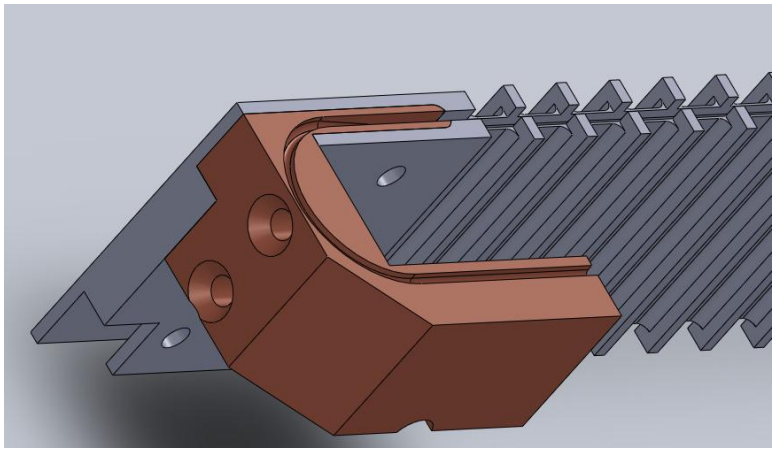

Figure 19 - Copper Current Terminal and Sample Holder

With all four current terminals in place for each of the six sample holders, the copper spacers were slid into place. The stainless steel backing plate was then positioned onto the copper terminal blocks and bolted into place. Figure 20 shows a photograph of the sample holder preparation up to this point.

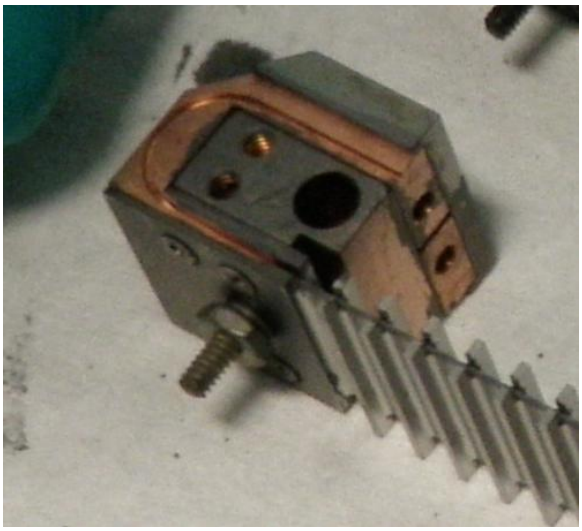

Figure 20 - Sample Holder Preparation without Wire

The sample wires were then carefully inserted into the channels of the sample holders and the U-shaped current terminals. After inserting the wire into the channel of a current terminator, the cover plate was screwed on top of the sample to keep it in the channel during handling and heat treatment. Stainless steel wires were inserted into the channel on top of the superconducting strands to help keep the samples in place during transport, heat treatment and testing. For the same reasons, thinner stainless steel wire was looped around the sample holder beams at regular intervals. A single length of wire per manufacturer was used for all three sample holders. One complete set of sample holders, before heat treatment, is shown in Figure 21. The extra length of wire, approximately 2 feet on each side, was left uncut beyond the end of the samples to help ensure consistent heat treatment that would exclude end conditions.

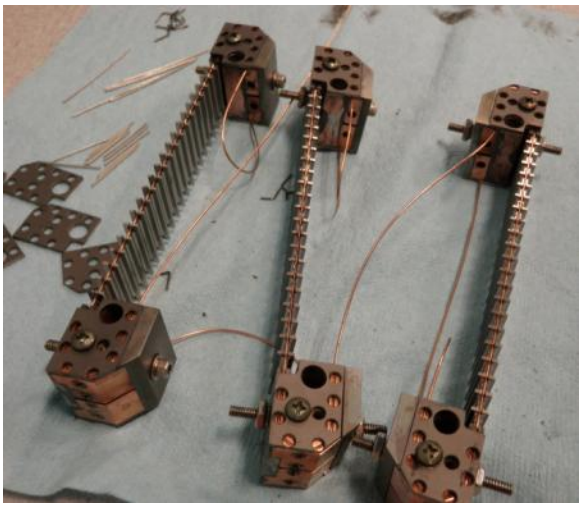

Figure 21 - Sample Holder Preparation with Wire

All six sample holders, one for each of the three bending ranges for each of the two manufacturers, were then bundled onto a rack and heat treated in a furnace for nearly 500 hours. The sample holders on the rack were carefully positioned to be in the center of the furnace to help ensure uniform heating. Included with the sample holders were standard J_c barrels; these were small sample windings with additional Nb_3Sn samples wound around them that could be used for baseline critical current measurements in the future if needed. The full heat treatment schedule is plotted in Figure 22.

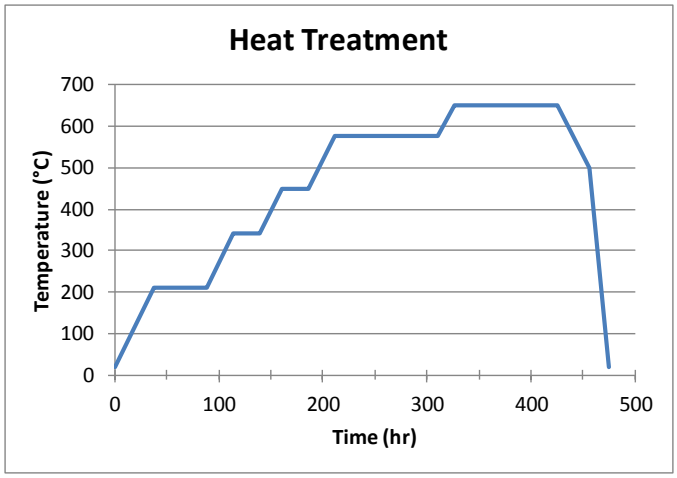

Figure 22 - Heat Treatment Schedule

Following heat treatment, the wire was cut close to the copper current terminal. The next step was to solder the samples to the channel of the current terminator both to ensure that the samples remain in the channel and to create a quality electrical connection between the copper current terminators and the superconducting strands. For soldering, the cover plates were removed and would not be needed again. The copper spacing remained in place and acted as a holder for a cartridge heater. A second cartridge holder was held against the outside edges of the current terminator. The cartridge heaters were connected to a variac to control the input power; a temperature sensor was also used to avoid overheating and potentially damaging the Nb_3Sn wires. The temperature sensor was connected to a temperature controller that switched the power to the variacs on and off to maintain a nearly constant temperature. Heating the copper current terminators and the sample itself helped produce a high quality electrical connection.

Once all the sample wires were soldered to the current terminators, the current leads needed to be soldered. The first step was to solder copper blocks to one end of the leads. These blocks would be connected to the current leads already mounted on the probe for testing. See Figure 23 for the connection site. A plastic insulating sleeve was then slipped over the majority of the length of the current leads to avoid undesired electrical connections between samples from being made on the probe.

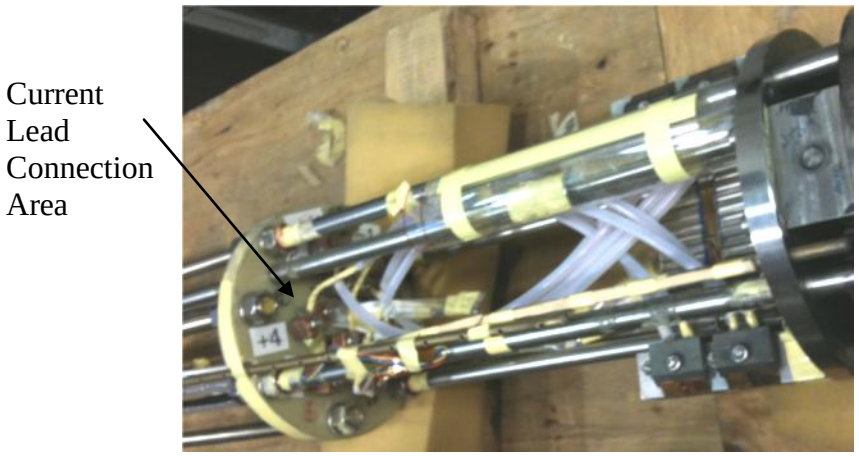

Figure 23 - Copper Leads Connection

The current leads were then inserted into the corresponding holes on the current terminals that were already filled with melted solder. It was found that giving the current leads a slight tapered cut at the end made it significantly easier to slide them in without losing several strands of the cabled copper wire. Although preparation was not complete at this stage, this soldering was the final step of preparation before shipping the equipment to the NHMFL. The samples prepared for shipping are shown in Figure 24.

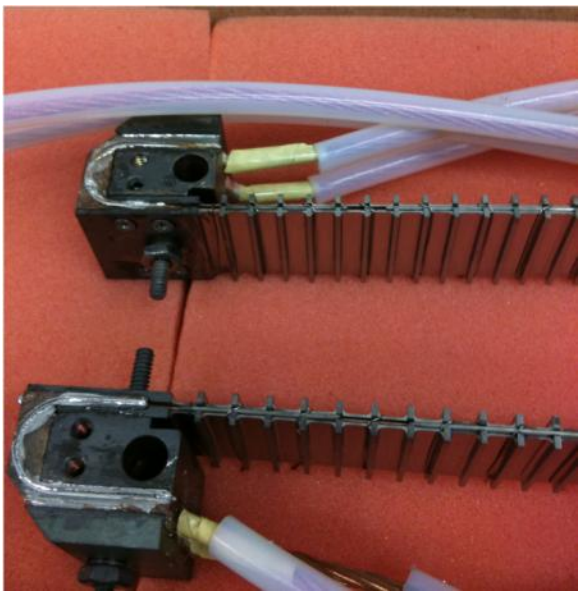

Figure 24 - Sample Holders Prepared for Shipping

Once arriving at the NHMFL, the copper spacers were removed and the voltage taps used for the measurements needed to be soldered directly to the Nb_3Sn samples. This step was taken after shipment because it was believed that the connection would be sensitive and could potentially be damaged during shipment. Each voltage tap consisted of two thin wires of different length that were twisted together. It was found during testing that the tightness of the twist had a profound effect on the signal to noise ratio; the voltage taps for the first day of testing were loosely twisted and produced noisy signals, but the remainder of the voltage taps were twisted more tightly and produced considerably cleaner signals, allowing for clear reading of microvolt level signals. Two voltage taps were used for each sample. A short voltage tap spanned the middle section of the sample with a nominal length of 50 mm. A long voltage tap spanned the length of the sample, nominally 115 mm. Measurements from both voltage taps were recorded for every test, but the signal from the short voltage tap was used for analysis

whenever possible because it excluded non-uniform end conditions that may have existed due to a not fully developed current flow or uneven bending strain.

At one end of the voltage taps, pins were soldered onto the wires for a quick connection to the voltage tap leads on the probe. The other ends of the two wires were soldered directly to the sample wire. A soldering gun was used to heat the sample holder and wire while a soldering iron was used to apply a thin coating of solder to the sample. The voltage tap was then soldered to the sample with a small amount of additional solder to produce a strong electrical connection that would have little noise.

3.2 Gear Box

With soldering complete, the next step was to mount the sample holders onto the gear box. The gear box assembly includes a series of worm gears, a main drive shaft and arm connectors to produce pure bending deformation.

3.2.1 Gear Box Components

The gear box consists of five gears positioned between two plates. The gearing converts the rotation from the single drive shaft into rotation for two torque arms that deformed the sample holders to the desired bending strain. The torque arms are broken down into several parts for ease of assembly. For each side of the gear box, the first part is the radial arm that extends parallel to the sample holder at 0.0% bending. Next are two vertical arms that connect to the radial arm and extend out from the top plate of the gear box. These two vertical arms connect to the sample holders. Figure 25 shows the gear box with major components

labeled. Note that the sample holders in the schematic are not the ones used in this research, but the remainder of the gear box assembly is the same as the one used for this study.

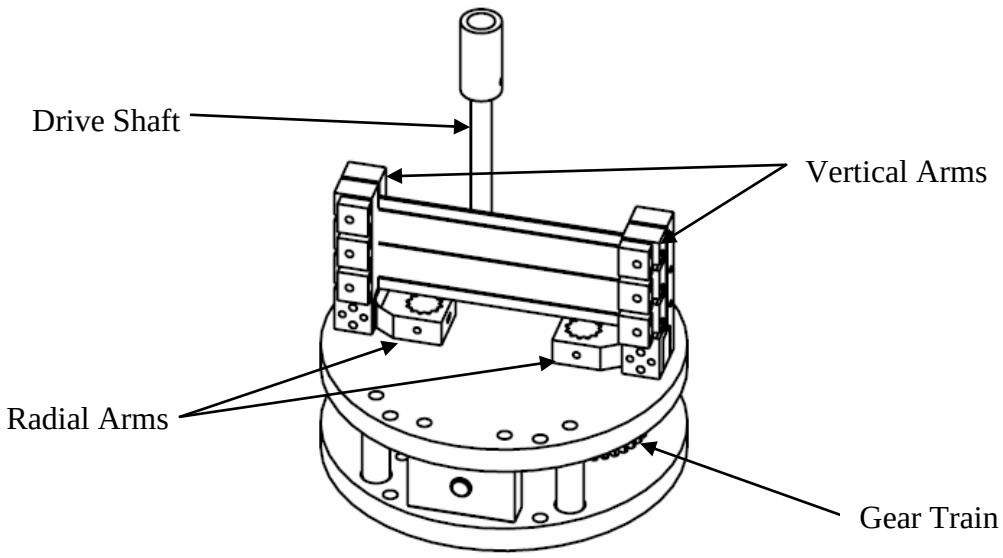

Figure 25 - Gear Box Schematic

3.2.2 Gear Box Preparation

Preparing the gear box assembly was a less involved process than the sample holders. All components of the gear train, including the top and bottom circular plates and the spacers, were thoroughly cleaned. All surfaces that mated against others were given a thin coat of graphite to reduce friction and the risk of galling that caused trouble in previous bending testing. All rotating components were given test rotations to detect smooth movement with little friction. After achieving satisfactory rotation, the radial arms were attached to their respective gear shafts and aligned to 0.0% bending.

The next step was to prepare to mount the sample holders to the gear box. To do this, the sample holders first needed to be connected to the vertical arms. See

Figure 26 for a view of the sample holders mounted onto the vertical arms. One vertical arm was slid into place where the copper spacers had been for two of the sample holders. Great care was taken not to damage the nearby voltage taps and superconducting samples. The other vertical arm was then placed on the outside edge of the sample holder. Both vertical arms were then bolted together to maintain a strong connection.

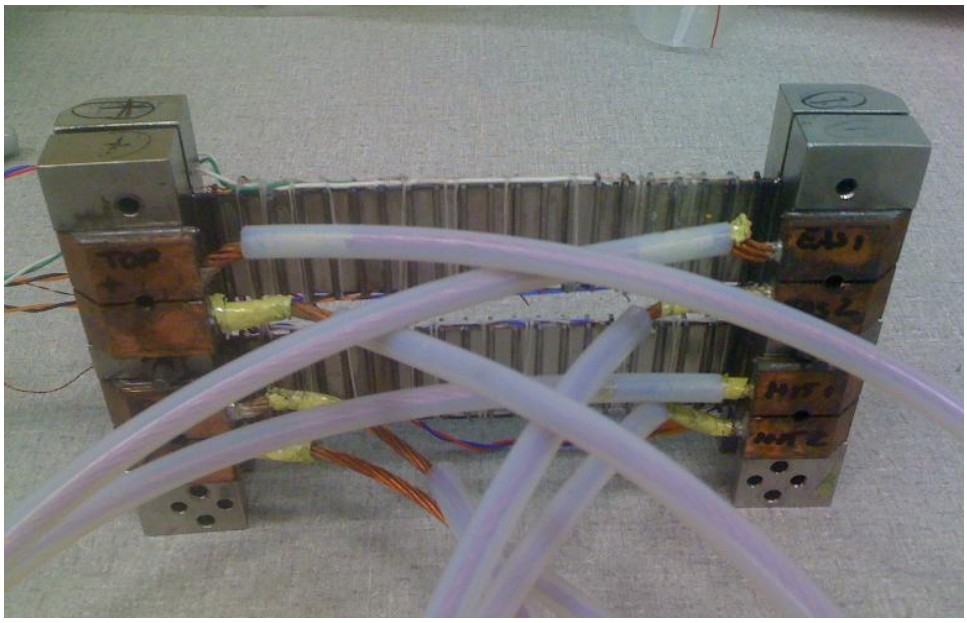

Figure 26 - Sample Holders Mounted on Vertical Arms

The sample holders and vertical arms subassembly was then place onto the gear box, using pins to connect the radial and vertical arms. The full gear box assembly, including the arms and sample holders can be seen in Figure 27.

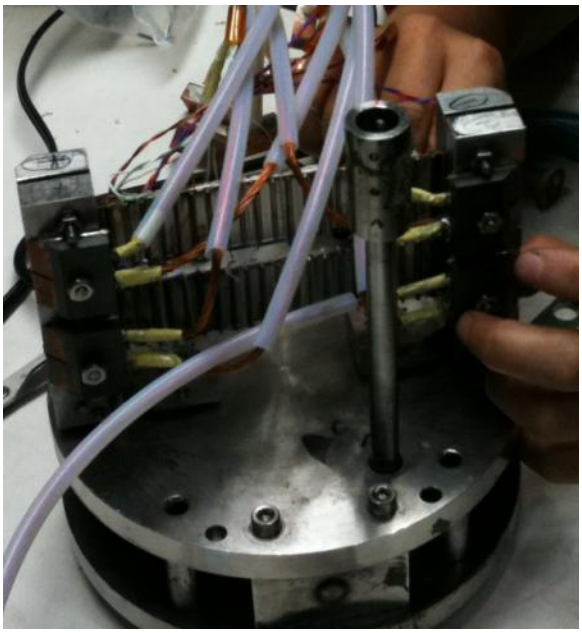

Figure 27 - Complete Gear Box Assembly

3.3 Probe

The probe had minimal setup requirements since most of the assembly remained intact from previous testing. The two most significant preparations regarding the probe were mounting the prepared samples and gear box to the bottom and mounting the motor and encoder system to the top of the probe.

3.3.1 Probe Components

The probe is a necessary component for the experiment as it positions the samples in the middle of the magnetic field in a bath of liquid helium. The probe has current and voltage tap leads that run from the sample area to the top of the probe, where they can be connected to the power source and multimeters, respectively. Also at the top of the probe, outside the dewar, was the end of the drive shaft. The original probe design featured a hand crank to power the drive shaft, but for

this research, a motor and encoder system was used. See Figure 28 for a generalized schematic of the probe.

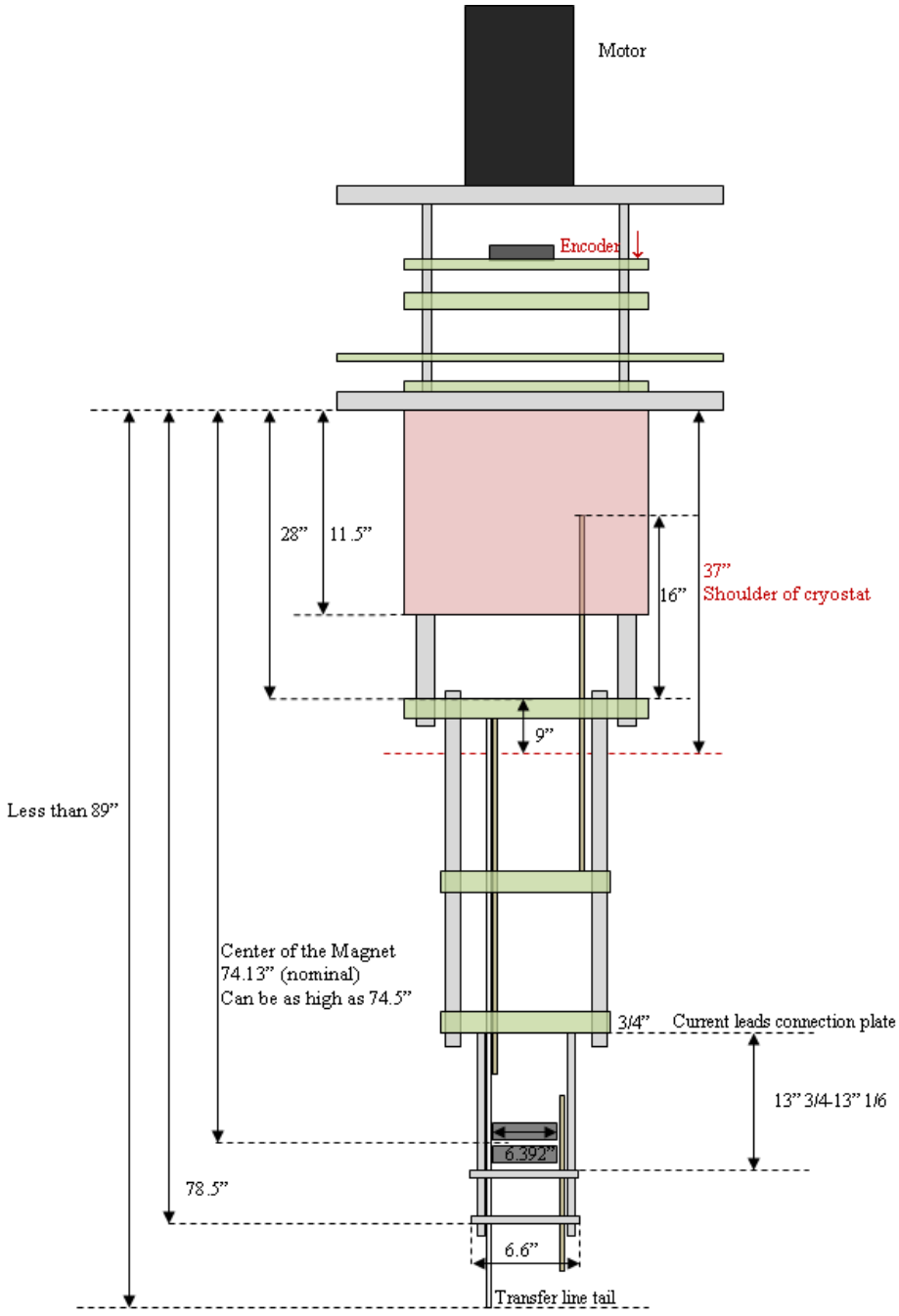

Figure 28 - Probe Schematic

3.3.2 Probe Preparation

The motor and encoder needed to be mounted onto the probe and connected to the drive shaft. To mount the motor, another steel plate was attached to the top of the threaded rods protruding from the top of the probe. The motor was then connected to the plate using three bolts. The encoder slid onto the shaft and was tightened into place. A shaft coupling, featuring a keyway and pin on the motor side and a pin on the probe's drive shaft side, connected the motor shaft to the probe's drive shaft. See Figure 29 for the motor mounted on the probe.

Figure 29 - Motor Mounting

The gear box slid onto the bottom of the probe and was locked into place with a series of nuts. Another shaft coupler was used to connect the probe's drive shaft

to the gear box's drive shaft. On the probe side, two pins were used as connectors; on the gear box side, one pin and eight gear teeth aligned and connected the two shafts. Additionally, the voltage taps and current leads from the sample holders needed to be attached to the leads on the probe. The voltage taps were simple electrical pin connections, while the copper blocks on the current leads were bolted up against similar copper blocks connected to the probe. See Figure 30 for the gear box mounted on the probe.

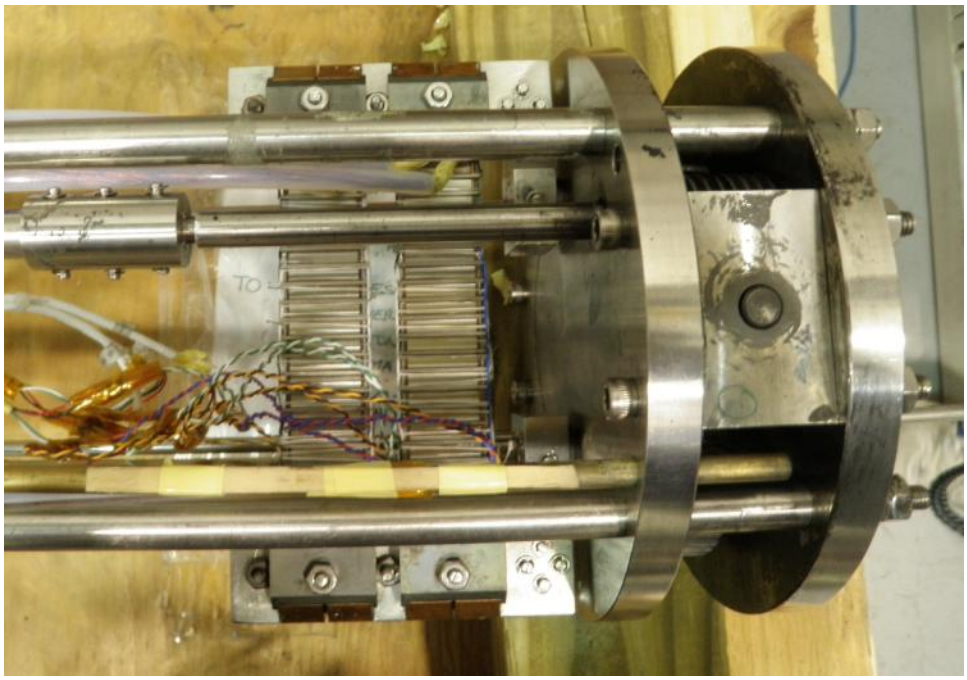

Figure 30 - Gear Box Mounted on Probe

3.4 Final Preparation

After mounting all the subsystems to the probe, only a few final test preparations remained. Current leads were set up between the probe's connectors and a switch block; the leads from the power supply were connected to this board in varying configurations to send current through the desired sample, one at a time for the

given bending load condition. The leads from the voltage taps were connected to a 32-pin connector board. Using the board allowed for quick changes between samples to minimize downtime between test runs. Three multimeters were setup and connected to the data acquisition board (DAQ). Two multimeters measured the voltages of the two taps while the third measured the input current. A LabView program, developed by the NHMFL, was loaded and used to record the data from the multimeters.

The outer dewar was kept full of liquid nitrogen throughout the week of testing. During the morning of each test, the inner dewar was filled with liquid helium. Sensors were used to monitor liquid helium levels throughout testing days to be certain that testing conditions were at a constant temperature of 4.2 K. The liquid nitrogen helped minimize thermal gradients and losses of liquid helium during testing.

4. EXPERIMENTAL RESULTS

Wide range bending tests were performed on single strands of bronze Nb_3Sn wire from two manufacturers, European Advanced Superconductors (EAS) and Hitachi Cable, Ltd. (HIT). Two samples from each manufacturer were tested for each of the three bending ranges, totaling 12 tested wire samples. A simple sequential numbering system was used to identify each sample with its manufacturer and bending range. For example, EAS 1 and EAS 2 refer to samples prepared from the EAS wire in the low bending range.

4.1 Data Collection and Preliminary Analysis

During testing, two voltage signals as a function of applied current were recorded in real time. The two signals corresponded to the short and long voltage taps for each sample. See Figure 31 for an example of the data collection screen; voltages measured in the range of 20-30 μV with low noise levels on the order of 1 μV. The red line represents the short voltage tap data and the blue line represents the long voltage tap data. When possible, the shorter voltage tap was used exclusively to ensure less error from the pure bending condition that may have resulted from end conditions where the sample holder beam mated with the arms. In a few instances, the shorter voltage tap broke or became disconnected from the sample, requiring use of the longer voltage tap. The nominal lengths of the short and long voltage taps were 50 and 115 mm, respectively, but there was slight variation from sample to sample. The short voltage taps measured 47-50 mm and the long voltage taps measured 114-116 mm.

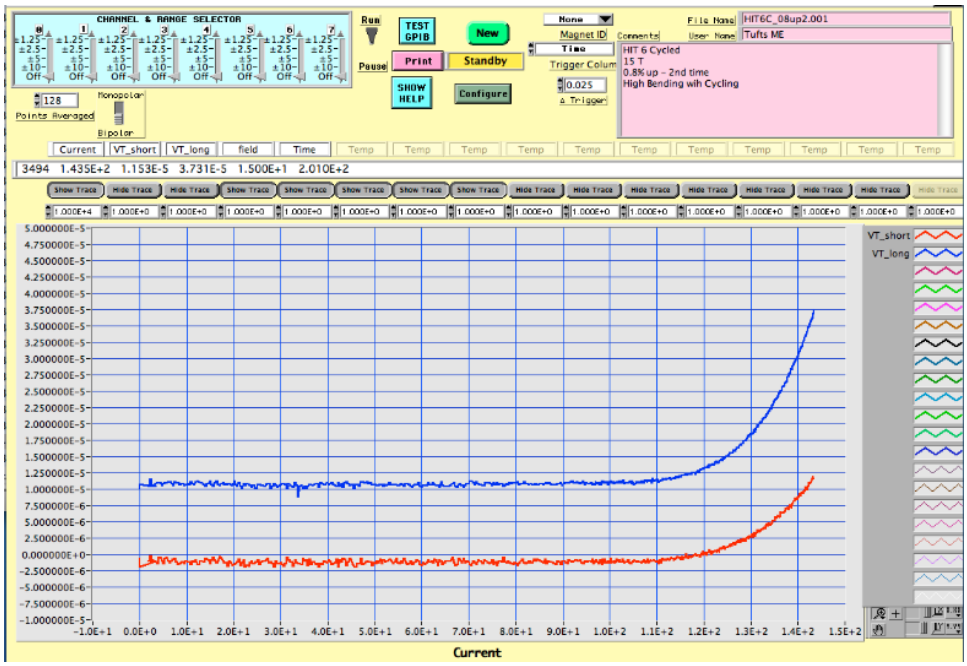

Figure 31 - Example of Real Time Data Acquisition

As seen in Figure 31, there is a voltage offset when tests are run. For data analysis, this voltage offset was eliminated. A simple noise reduction algorithm was then applied to the voltages, using a five point average as seen in Equation 1.

$$V_{avg} = \frac{V_{n-2}+V_{n-1}+V_n+V_{n+1}+V_{n+2}}{5} \quad (1)$$

Figure 32 shows a typical example of the data from the short voltage tap. The horizontal dashed lines mark three standard electric field criteria, to determine critical current for superconducting wires. The 10 μV/m, 100 μV/m and 200 μV/m criteria are commonly used in the industry. The criteria represent the electric field in the sample being tested. Since voltages were being measured, the electric field criteria needed to be converted into voltages by multiplying by the lengths of the voltage taps. For instance, the 100 μV/m electric field criterion was nominally equivalent to a 5 μV voltage criterion for the short voltage tap of 50 mm. During testing, the nominal lengths of the voltage taps were used to quickly approximate voltage criteria and critical currents; exact values of voltage tap lengths were used in later calculations.

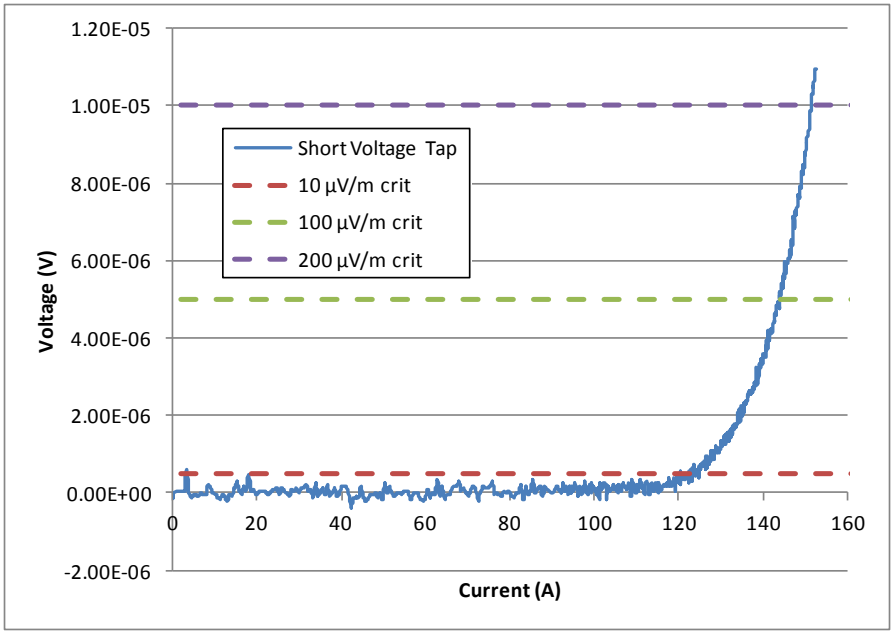

Figure 32 - Data Plot Sample

Most samples exhibited the exponential behavior that is typical of a real superconductor's transition to a resistive state, but a few samples quenched, or lost superconductivity, without displaying the exponential transition phase. Although it is easy to see the critical current for all three criteria in Figure 32, noisy data made the 10 µV/m criterion difficult or impossible to accurately detect for many other samples.

To this point, the critical current has been determined across a range of bending strains. An additional characteristic of the transition from the superconductive state to the resistive state is referred to as the n-value. The n-value is from Equation 2 and describes the sharpness of the transition from the superconducting state to the resistive state.

$$\left(\frac{E}{E_c}\right) = \left(\frac{E \cdot l_{voltagetap}}{E_c \cdot l_{voltagetap}}\right) = \left(\frac{V}{V_c}\right) = \left(\frac{I}{I_c}\right)^n \qquad (2)$$

where E is the electric field, V is the voltage, I is the current, *l* is the length of the voltage tap and the subscript c denotes the critical values. By converting the collected voltage-current data into a log-log plot, the slope of the resulting line is the n-value of the sample under those conditions. Figure 33 shows an example of the logarithmic plot.

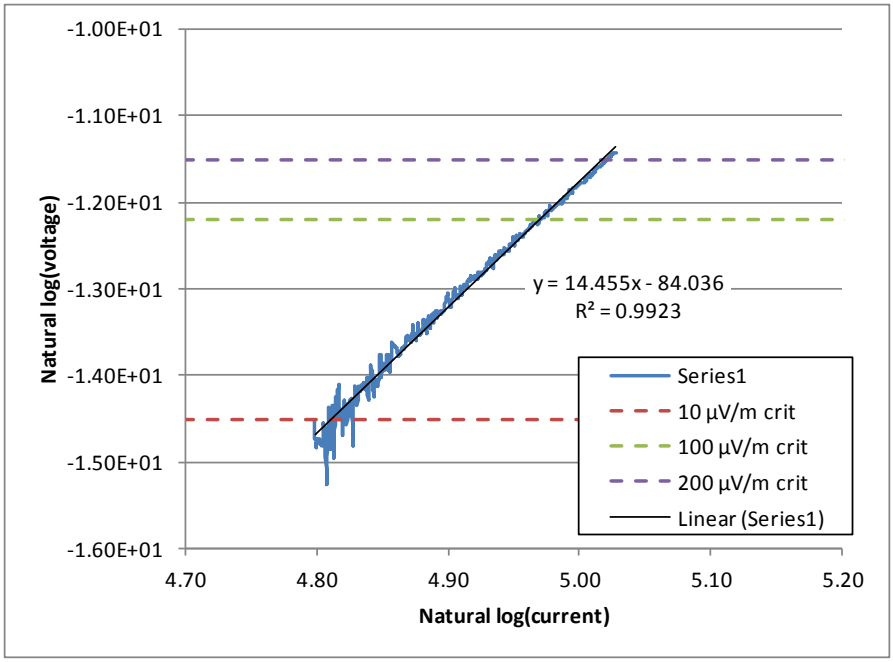

Figure 33 - Logarithmic Plot Sample

From the logarithmic plot, a linear trendline produces an equation that yields the n-value. The equation was also utilized to find better approximations for the critical current than the simple observation of the raw data plots provided. Like previously discussed, not all the data collected provided accurate results for the 10 µV/m criterion; in some cases the linear fit equation was used to extrapolate values for the 10 µV/m criterion. After computing the critical currents for each strand relative to the applied bending strain, those currents were normalized by the initial critical current without strain obtained before applying bending.

4.2 Critical Current Results

Figure 34 plots the critical current results using the 10 µV/m criterion for both the EAS and Hitachi samples across the entire bending range of 0.0-1.4%. Figure 35 shows the critical currents for the 100 µV/m criterion. All the plots and results presented in this chapter are from tests run at 15 T and 4.2 K. Separate plots for each bending range will be shown later to more clearly observe the behavior of each sample and highlight their response to cyclic loading, sequence of loading and unloading conditions.

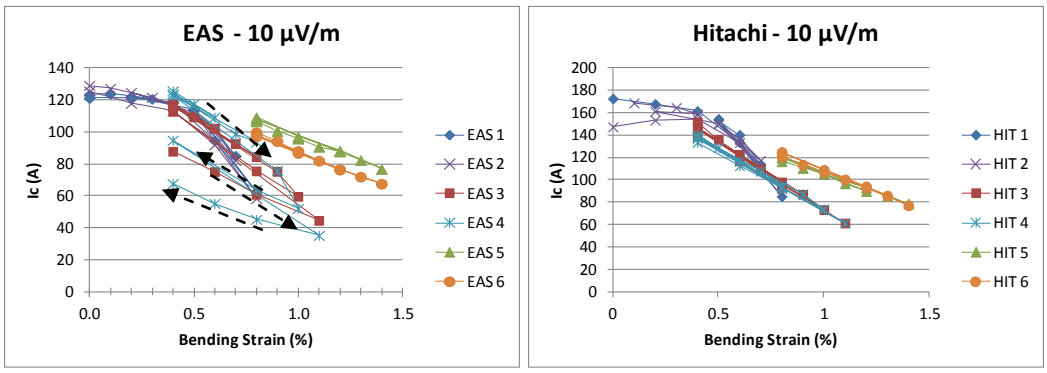

Figure 34 - Critical Current over Full Bending Range: 10 µV/m criteria

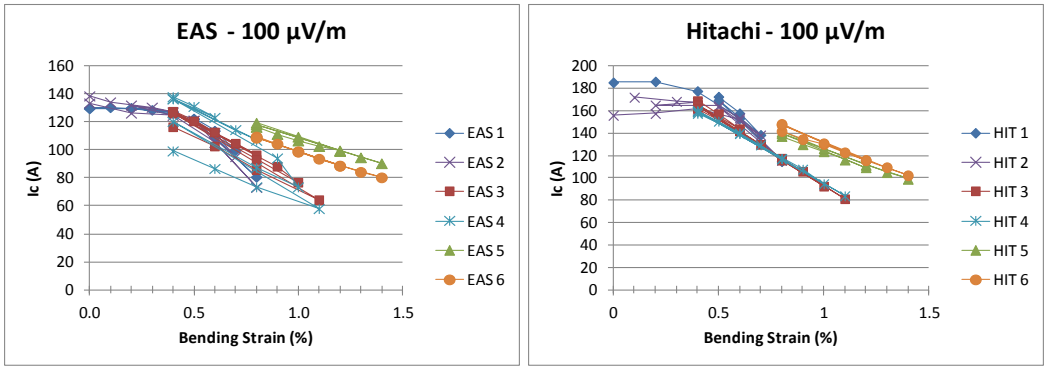

Figure 35 - Critical Current over Full Bending Range: 100 µV/m criterion

The critical current of the samples decreased as bending strain was applied and increased to previous levels when the strain was removed, showing no permanent

degradation of the critical current with the exception of the medium bending range EAS samples. As can be seen in Figure 34 and Figure 35, all four samples tested with the high bending sample holders, numbered 5 and 6, had higher critical currents and a more gradual critical current drop-off than the samples tested for the medium bending range, numbered 3 and 4, at the same strain values, and no permanent degradation as strain was removed. Expectations were that the critical current would match well with the higher end of the medium bending range with the possibility, though no certainty, of permanent degradation. Potential reasons for this disagreement between the medium and high bending range results will be discussed in later sections.

Figure 36 displays the normalized critical current over the full range of bending strain. The critical current is normalized against the critical current of the samples without any applied strain. Such a plot provides a relative sense of the degradation of critical current as bending strain increases and makes the comparison between strands from different manufacturers easier. Without the absolute values of critical current plotted, it is easy to detect a percentage of the maximum critical current lost at any value of bending strain. For both the EAS and Hitachi samples, the data from the medium bending sample holder indicates critical currents decrease to around 40-50% at 1.1% bending strain, but the data from the high bending sample holder shows the critical current decreasing to 60% at 1.4% bending strain. None of the results showed noticeable permanent degradation.

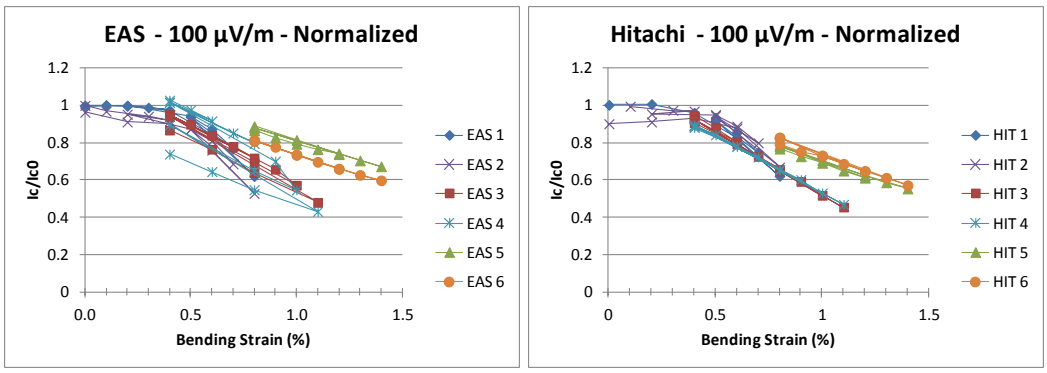

Figure 36 - Normalized Critical Current over Full Bending Range: 100 µV/m criteria

4.2.1 Low Bending Range Results

Plotted in Figure 37 is the critical current against the applied bending strain for the low bending EAS and Hitachi samples, covering a range of 0.0-0.8% bending strain. Shown in Figure 38 is the normalized critical current against the applied bending strain for these samples. All plots from this point forward will represent the 100 µV/m criterion unless specified otherwise; this is done because it is the lowest criterion that did not require any data extrapolation to meet. The data for the HIT 2 sample is from the long voltage tap because the short voltage tap broke during test setup.

The critical current for all four low bending samples is normalized against its own 0.0% strain critical current. All four samples performed consistently with little variation in critical current at each instance of a particular bending strain with some exceptions for the Hitachi samples. The HIT 1 sample has fewer data points since it quenched without showing an exponential superconducting-to-resistive transition phase for the first few applied strains up to 0.4% bending. For both manufacturers, there was little reduction in the critical current up to strains of

0.4%. From there, the loss of critical current began to steepen slightly with additional applied strain.

The undeformed critical current of the EAS samples ranged from approximately 130-138.5 A. The Hitachi samples had a more significant range of undeformed critical current values, ranging from 155-185 A. The HIT 2 sample, especially, showed a less consistent range of critical current measurements at very low bending strains. At these very low strain values, the samples were susceptible to quenching near their critical current values. Unlike the higher applied bending strains, the low bending results needed to be extrapolated to obtain critical current values often for the 10 µV/m and sometimes for the 200 µV/m. The quenching may have added some uncertainty into the critical current and n-value calculations for those cases that needed to be extrapolated. Even with some variability at the low bending, all the samples maintained at least 90% of their maximum critical current after ramping up the bending strain to 0.8%.

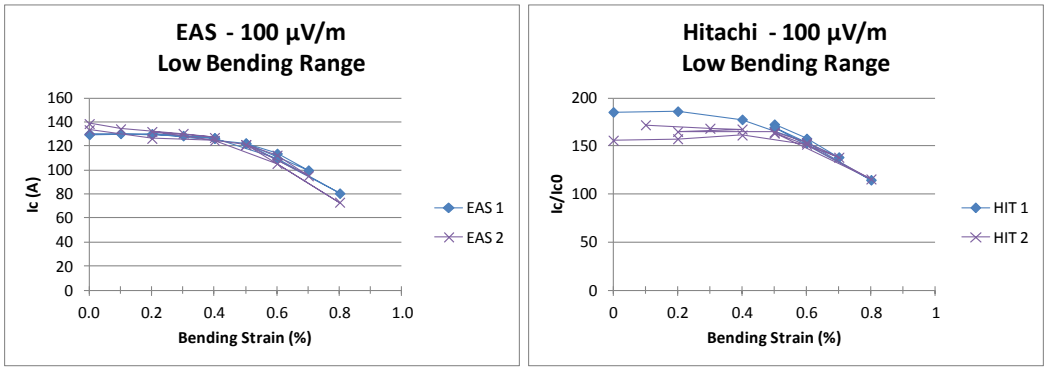

Figure 37 - Critical Current: Low Bending Range

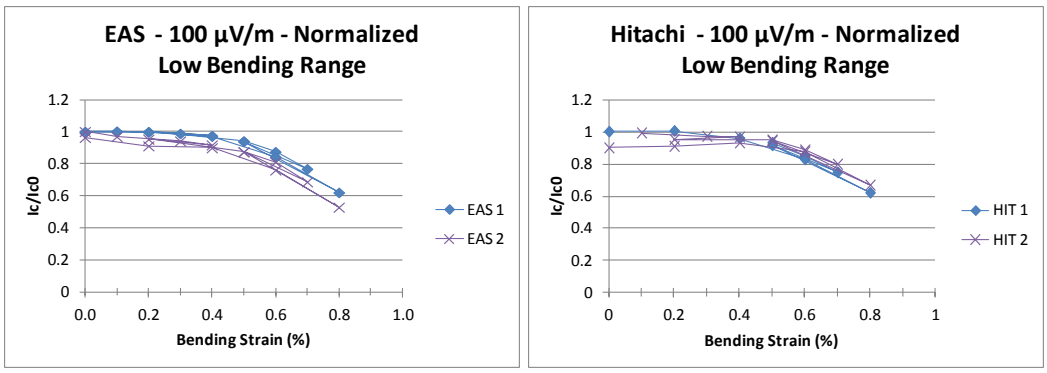

Figure 38 - Normalized Critical Current: Low Bending Range

4.2.2 Medium Bending Range Results

The critical current results for the medium bending range, 0.4-1.1%, can be seen in Figure 39 and the normalized critical currents results can be found in Figure 40. Since these samples and the ones for the high bending sample holder were not tested at 0.0% strain, their critical current could not be normalized against a value specific to those samples. Recall that the medium and high bending range sample holders were expected to be unable to react the high Lorentz forces at low bending strains. Thus, all eight of the medium and high bending range samples were normalized against the average critical current of the samples by their respective manufacturers that were tested at 0.0%. For example, the EAS 3 sample was never tested at 0.0%; therefore, to calculate a normalized critical current, the average of the critical currents for EAS 1 and EAS 2 at 0.0% bending was used.

The medium bending range samples showed a nearly linear decrease in critical current as applied bending strain increased from 0.4% to 1.1%. The Hitachi samples displayed very consistent behavior; a spread of approximately 4 A at

0.4% bending strain for the HIT 3 sample was the most significant range for the Hitachi samples. Each of the four medium bending range samples experienced approximately a 55% loss of critical current at 1.1% bending strain.

The results for the EAS samples, particularly the EAS 4 sample, displayed a considerable spread in critical current values, with a 40 A range between minimum and maximum values at some bending strains. The lower measured values began after cycling the bending strain up to 1.0% and then removing it. Such a behavior would indicate that the EAS 4 sample experienced permanent critical current degradation so that it did not return to its original critical current value once the bending load is removed. The EAS 3 sample also showed some permanent degradation after the 1.1% bending strain was applied. Since these two samples are the only ones that showed this behavior, however, there is not enough evidence to determine if the permanent degradation is due to pure bending strain or another unidentified source, such as undesired, or non-circular, deformation of the sample holder.

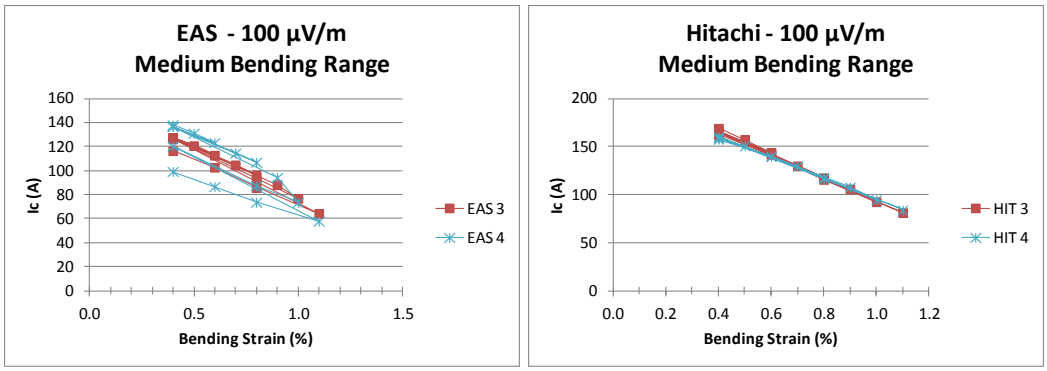

Figure 39 - Critical Current: Medium Bending Range

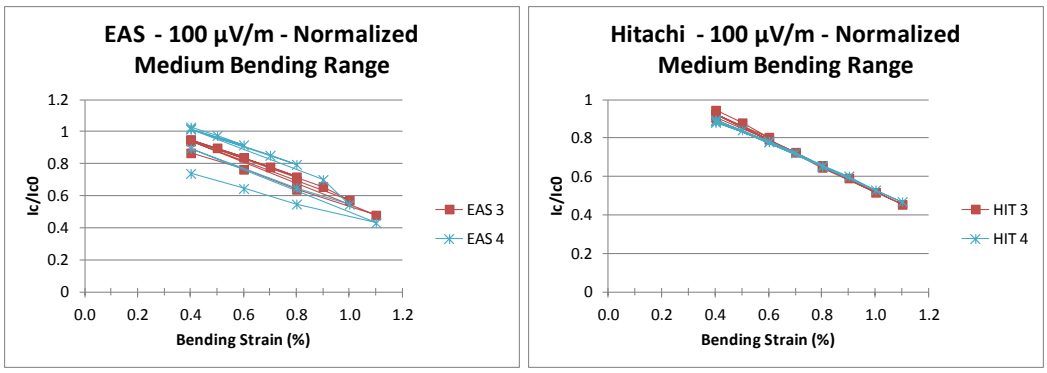

Figure 40 - Normalized Critical Current: Medium Bending Range

4.2.3 High Bending Range Results

Finally, the critical current results for the high bending range, 0.8-1.4%, are plotted in Figure 41. Figure 42 displays the normalized critical current for the high bending range. The two most notable trends regarding the final bending range are the upward shift in critical current and a more gradual negative slope compared to the medium bending range. The increase in critical current over the measurements from the medium bending range prompted a detailed study into possible explanations of these results that will be further discussed in a later section.

First, though an examination of the high bending data shows very consistent results from sample to sample and from multiple measurements of a single sample at each applied load. The EAS 6 sample maintained a critical current capacity of 109 A at 0.8% strain and 80 A at 1.4%; the EAS 5 sample showed similar trends, but with critical currents 7-10 A greater. The HIT 5 sample consistently performed at slightly lower critical current values compared to HIT 6, ranging from 137 A at 0.8% bending strain to 99 A at 1.4%.

The normalized critical current results indicate that both the EAS and Hitachi samples maintain approximately 80% of their maximum critical current with 0.8% applied bending strain and approximately 60% at 1.4% applied bending strain. As with the other bending ranges, no permanent degradation occurred, as the samples were able to return to their original critical current levels after the high strain loading was removed.

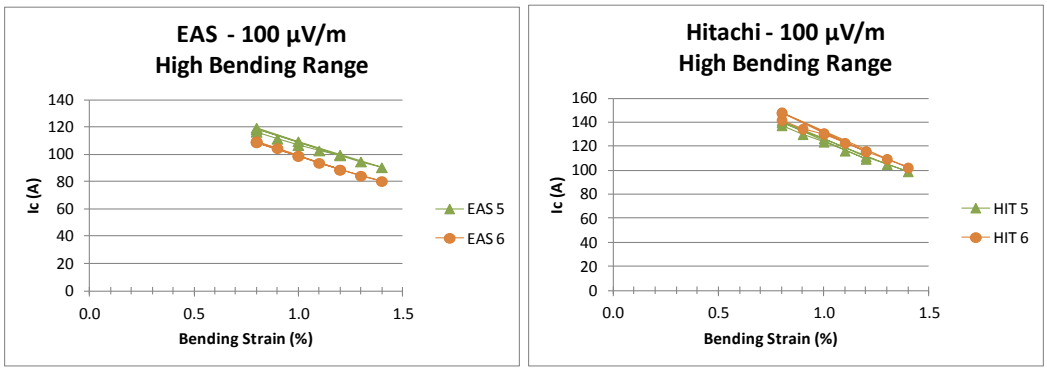

Figure 41 - Critical Current: High Bending Range

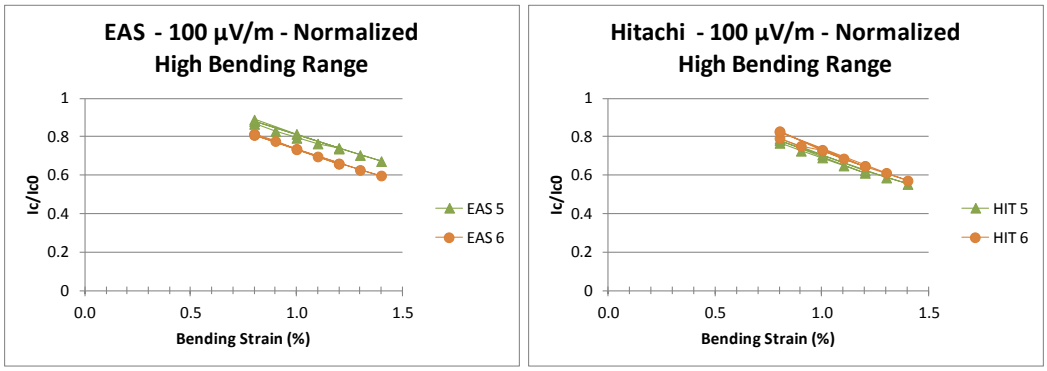

Figure 42 - Normalized Critical Current: High Bending Range

4.3 N-value Results

As previously mentioned, another characteristic of superconductors is the n-value that describes the sharpness of the transition from a superconductive state to a resistive state. The n-values for all the samples from the three bending rangers

are plotted in Figure 43. For both the EAS and Hitachi samples, the n-values were largest at lower strain values. This trend correlates well with the testing experience as it was these test runs that showed a quick increase in resistivity and with a relatively high chance of quenching. The n-values for the low bending strain Hitachi samples that range from 80 to nearly 120 are much higher than the rest of the samples. This is believed to be the case due to significant noise on the voltage tap signals, high risk of quenching and limited data. The samples that had consistent critical currents also had consistent n-values with a typical range of 5-25. As the applied bending strain increased, the n-value tended to decrease.

The medium bending range EAS samples, EAS 3 and EAS 4 also displayed a decrease in n-value as the applied bending strain increased, but the n-values did not recover as the load was removed. Similarly to the critical current results, this trend indicates permanent degradation, though the source is not completely clear given the limited data. Additional testing of EAS samples with the medium bending sample holder might be able to explain the cause of the degradation.

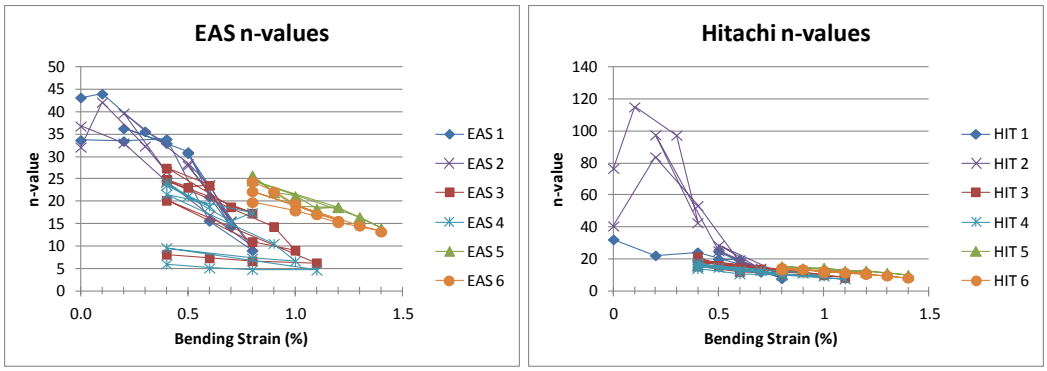

Figure 43 - EAS and Hitachi n-values

5. INVESTIGATION OF EXPERIMENTAL RESULTS

The consistent shift toward higher critical currents for the high bending range samples compared to the low and medium bending range samples prompted a detailed study of possible causes. One potential explanation for the different behavior was that the high bending sample holder did not deform in a pure bending fashion. Rather, it was believed that it could have deformed significantly more around the ends, leaving the middle of the test sample less deformed than expected. A second possible reason for the results was that the bronze process Nb_3Sn samples are sensitive to cyclic loading. While the samples for the low and medium bending range had their deformation cycled up to 0.8% and 1.1%, respectively, the samples for the high bending sample holder began in this bending range; perhaps the cycling that the low and medium range samples experienced in reaching the 0.8-1.1% bending strain led to additional degradation.

5.1 High Bending Voltage Tap Analysis

Since the possibility of non-uniform deformation could be analyzed with data that was already collected, it was the first option explored. In order to determine if this situation was what actually occurred, the voltage signals and the corresponding critical current results from a sample's short voltage tap were compared to those of its long voltage tap.

In the ideal case, the electric field would be constant throughout the length of the sample. Thus, the voltage measured from each tap divided by its length should be identical for the short and long voltage taps and lead to the same critical current values. If this were the case, it would indicate that the sample was deformed to a

constant strain over the entire length of the testing region, indicating circular deformation.

The voltages across three regions of the sample were examined to better determine the deformation of the samples. The long voltage tap data was compared with the short voltage tap data and the difference between the two. Including the difference between the measurements of the two voltage taps provided combined voltage measurements for the two outer regions on each side of the short voltage tap. A depiction of these regions can be seen in Figure 44: the short voltage tap measures across the black portion, the long voltage tap measures across the entire length and the difference is shown in gray.

If the outer regions exhibit a greater voltage per unit length than the short voltage tap, indicating that they were deformed to a greater extent, and thus showing a lower critical current value, then it would be likely that the actual deformation of the sample holder varied significantly from the expected pure bending deformation. Figure 44 also displays a simple schematic of the desirable and undesirable bending. If the undesired deformation shown on the right occurs, then it would be likely that the amount of bending strain applied to the middle of the sample would be less than anticipated.

Figure 44 - Bending Schematic. Left: Desirable deformation; Right: Undesirable deformation (not to scale)

As a reminder of nomenclature and the experimental setup, here is a rundown of the sample names and their positions relative to the gear box. The sample holder closer to the gear box held the Hitachi samples; the even numbered Hitachi samples were the closest to the gear box, while the odd numbered samples were on the side of the sample holder further from the gear box. The EAS samples followed the same convention as the Hitachi samples, but on the sample holder that was further from the gear box. Figure 45 shows a graphical representation of this nomenclature for clarity.

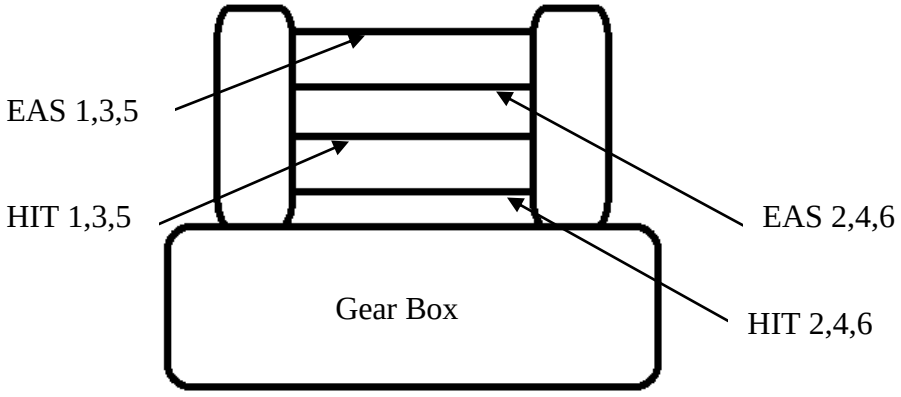

Figure 45 - Sample Nomenclature Schematic

The following plots in Figure 46 show select results of progressive increases in bending strain for two samples, specifically the bottom EAS sample for the

medium and high bending ranges. In each plot, the blue line is the short voltage tap data, the red line is the long voltage tap data and the green line is the difference between the long and short voltage taps. The selected plots include the bending strains that were applied in both the medium and high bending ranges for the EAS samples, though the entirety of those two ranges were examined for trends for both samples.

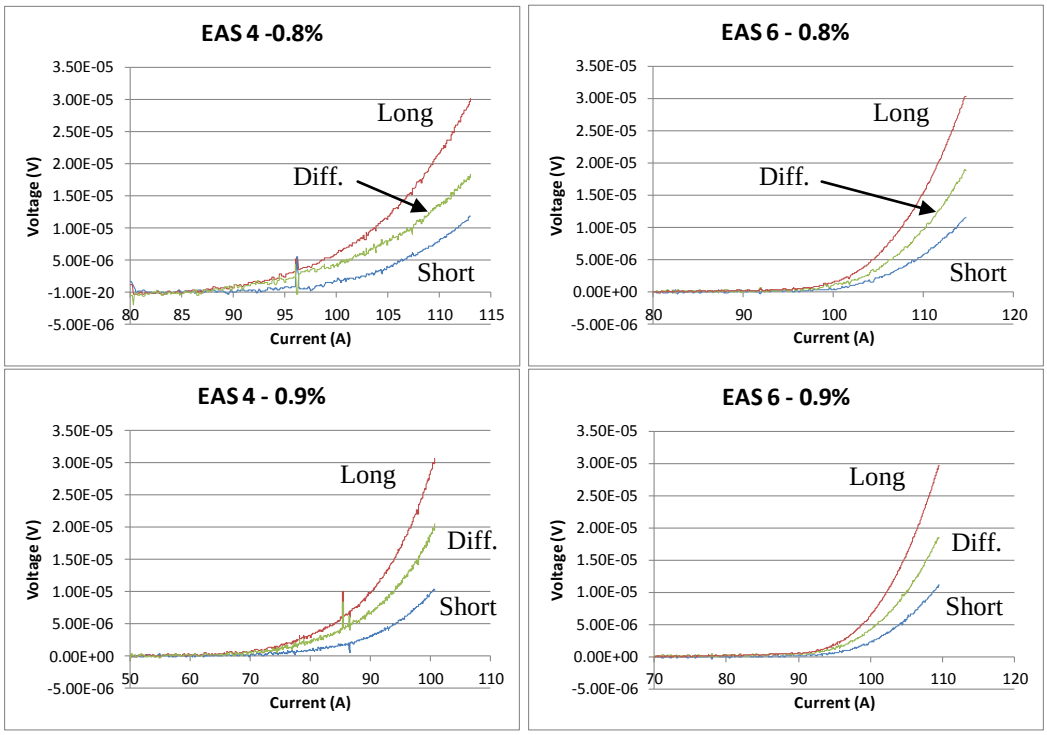

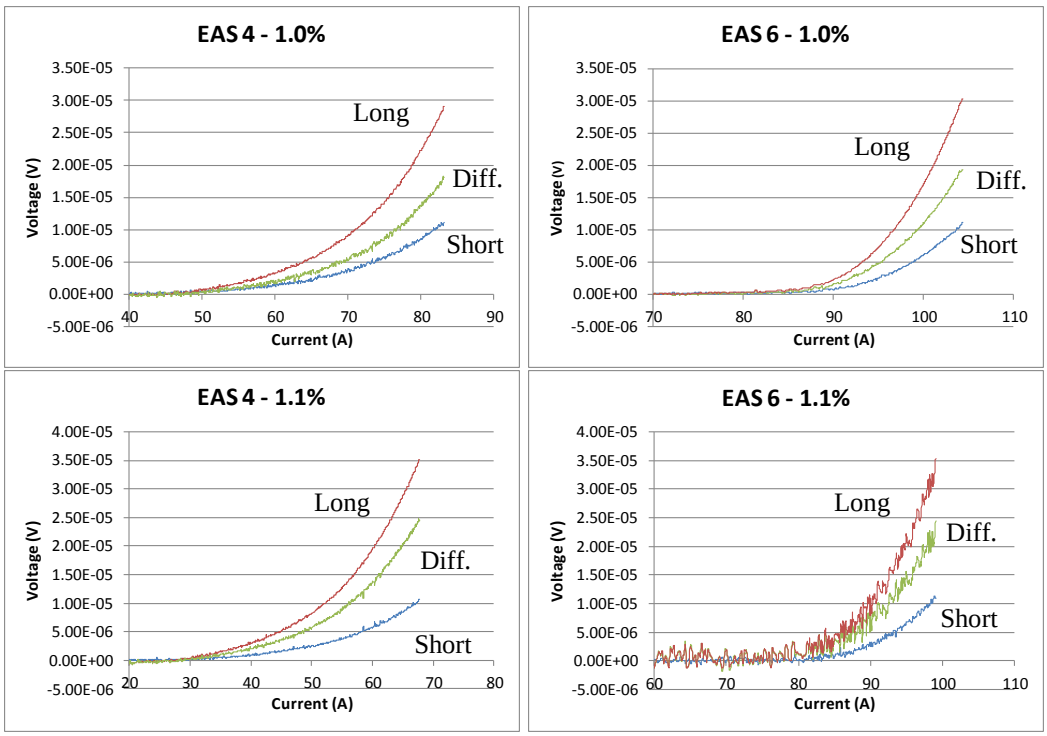

Figure 46 - EAS Medium and High Bending Range Voltage Comparisons

As can be seen from the selected plots, the voltage across the middle of the samples is consistently less than over the outer regions; however, the difference is not large enough to conclude that the sample holders deform unevenly. It is expected that the short voltage tap region will have a lesser voltage as its length is slightly less than half the total length of the sample. Another important trend to note is how well the voltages correlate for the two different sample holders. The relative position of the voltage tap difference (the green line) compared to the long and short voltage tap data remains consistent for any given bending strain for both the medium and high bending sample holder. As such, the difference in critical current results between the medium and high bending range cannot be explained by a non-circular deformation of the high bending sample holder. This will be explained in more detail in the following section.

The trends were relatively similar across the range of samples; specifically, the voltage of the outer areas begins in one position relative to the voltage from the short voltage tap then shifts toward the long voltage tap data line as bending increases. Although the results seemed to worsen for higher bending strains, the results for strains found in both the medium and high ranges correlated closely enough that it seemed unlikely that the experimental results observed were caused by inconsistent bending strain along the length of the sample.

Additionally, the critical current was calculated for the data from both voltage taps and their difference. The following figures plot some of the results for the samples for the high bending range. Again, in the ideal case, the critical current calculation would be consistent regardless of which voltage tap was used to calculate it. Figure 47 represents the best case, or nearly identical results independent of the voltage signal used. Figure 48 plots the worst results of the batch. The other two samples exhibited behavior that was slightly worse than the plotted results for the EAS 6 sample.

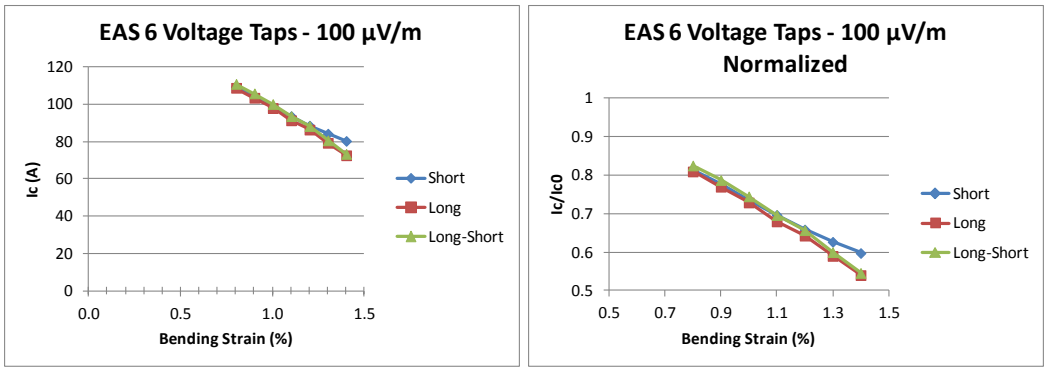

Figure 47 - EAS 6 Voltage Tap Analysis: Critical Current Results

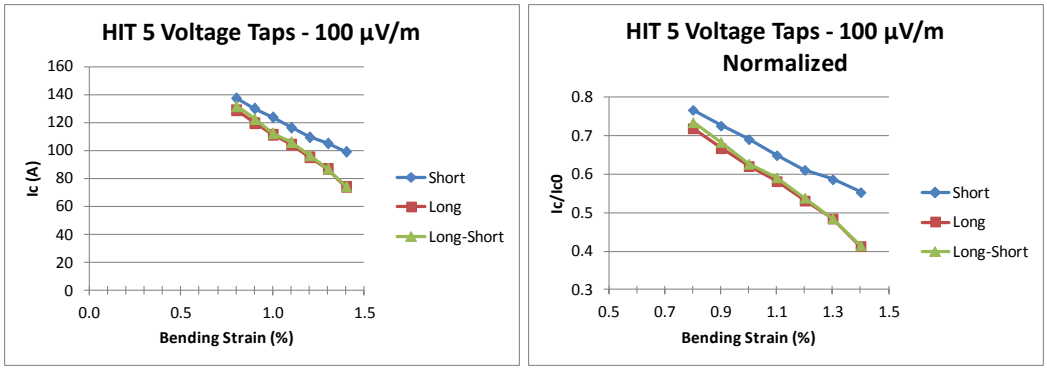

Figure 48 - HIT 5 Voltage Tap Analysis: Critical Current Results

For the EAS 6 sample in Figure 47, the critical current measurements were very consistent for each measurement through 1.2% bending strain. For the HIT 5 sample in Figure 48, the short voltage tap consistently indicated a greater critical current than the long voltage tap and their difference. The difference at 0.8% applied bending strain was approximately 8.5 A, or 4.5% of the sample's maximum critical current. At 1.4% bending strain, the difference was approximately 15 A, or 14% of the sample's maximum critical current. The differences seem to be significant for this worst case scenario, but the lower critical current values from the long voltage tap and the difference still do not fully account for the difference between the medium and high bending range results. As can be seen in Figure 49, the lower critical current values lie in between the results for the two medium bending Hitachi samples and the critical current calculated from the short voltage tap.

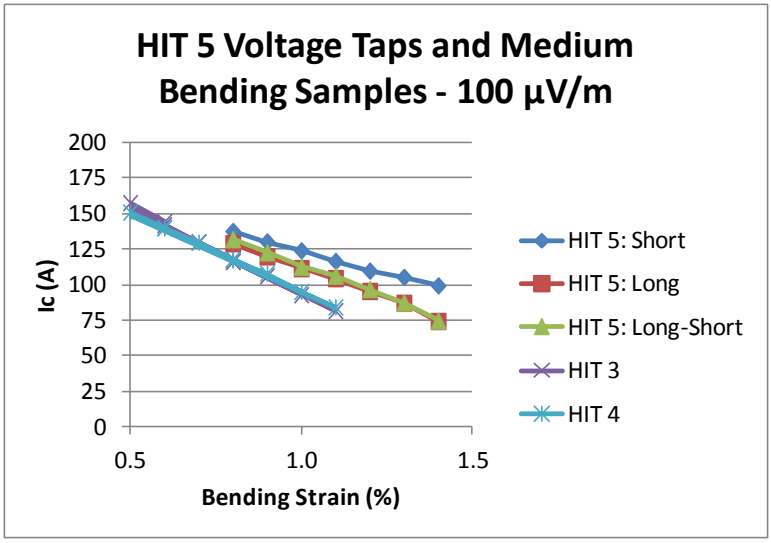

Figure 49 - HIT 5 Voltage Taps and Medium Bending Samples

The more significant differences at the high end of the bending range for all the samples raises some concerns about the sample holders' ability to deform uniformly at such high bending strains. Also, the consistently higher critical current results from the short voltage tap for the HIT 5 sample call into question the sample holder's ability to deform uniformly. While much of results seem to indicate that the high bending sample holder deformed uniformly, the significant gap for the HIT 5 results prevents a concrete conclusion from being made without more testing and analysis. Additional testing to determine the potential impact of load cycling was one of the next steps; those tests would also provide additional data to help determine the extent of deviation from pure bending.

5.2 Room Temperature Test

Before running additional tests at the NHMFL, a short series of simple room temperature tests were performed with the high bending sample holder to obtain a qualitative sense of error from pure bending. The sample holder was deformed to

0.6% and 0.8%, then compared to a block that featured a curved edge, representative of the sample holder's desired deformation.

Observation of the setup indicated slight error from pure bending, but not of magnitude that would have been required to explain the better than expected results. The greatest and most conservative estimation of deviation from the nominal bending strain was about 0.05%. As can be seen in Figure 50, the high bending sample holder would have had to consistently deform to a bending strain of at least 0.1% less than the expected strain value to yield comparable critical current values to the medium bending samples. This can be seen by examining the horizontal distance between the medium and high bending curves at any critical current value.

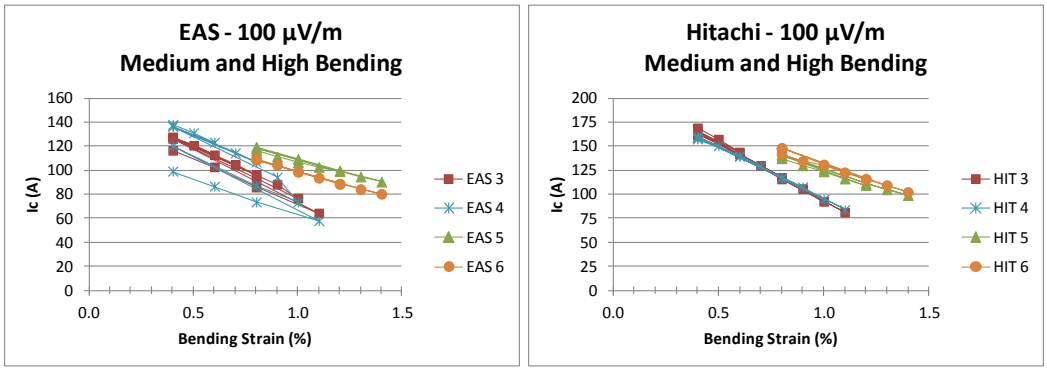

Figure 50 - Comparison of Medium and High Bending Results

5.3 Cycled Load Testing

In order to determine if cyclic loading had significant effects on the samples, an additional day of testing was needed. The fourth testing day reused the high bending samples, sample holders and voltage taps. As such, the only major intended change from the third day of testing was the applied loading. In addition

to the loading that the samples had already experienced from the earlier testing, the samples were held at 0.4% bending strain three times to include more cycling, more closely representing the cycles experience by the medium bending samples. The first half of the testing day indicated that the original results were not caused by a lack of load cycling as even if the high bending samples were cycled the same amount as the medium bending samples, they still had higher critical current values than the medium bending samples. A discussion of these early results and conclusions is to follow. With extra available time to test at the NHMFL, the samples were also tested below the sample holder's proposed range of 0.8-1.4% bending and with a reversed current direction.

Figure 51 lists the applied bending strains in the order tested. Only the rows that include 'Ic' under the 'Measurement' column were tested for critical current; the first three instances of 0.4% bending strain were applied only to include load cycling, not to test for critical current. The bending strain values that include '*' indicate a reversed current direction to test for the significance of Lorentz effects.

#	Bending Strain (%)	Measurement		#	Bending Strain (%)	Measurement
1	0.8	Ic		14	1.0	Ic
2	0.4			15	1.0*	Ic
3	0.8	Ic		16	0.8	Ic
4	0.9	Ic		17	0.8*	Ic
5	1.0	Ic		18	0.6	Ic
6	0.4			19	0.6*	Ic
7	1.1	Ic		20	0.4	Ic
8	0.4			21	0.4*	Ic
9	0.8	Ic		22	0.2	Ic
10	1.0	Ic		23	0.2*	Ic
11	1.2	Ic		24	0.0	Ic
12	1.4	Ic		25	0.0*	Ic
13	1.2	Ic				

Figure 51 - Day 4 Testing Schedule: * indicates reverse current direction

5.3.1 Cycled Load Results

Early results from the new test runs that applied additional cycling did not differ in a substantial way from the original results for the high bending samples, as can be seen in Figure 52 and Figure 53. The plots on the left display the critical current values and the plots on the right show the normalized critical current with comparisons to the original results. The critical current measurements for the cycled EAS samples are nearly identical for the entire high bending range. The Hitachi results revealed slightly lower critical currents across the range, particularly for the HIT 6 sample, but the trends are remarkably similar and the values are not too different; the greatest single difference was 16 A or 9% of the maximum critical current for the HIT 6 sample at 0.8% bending strain.

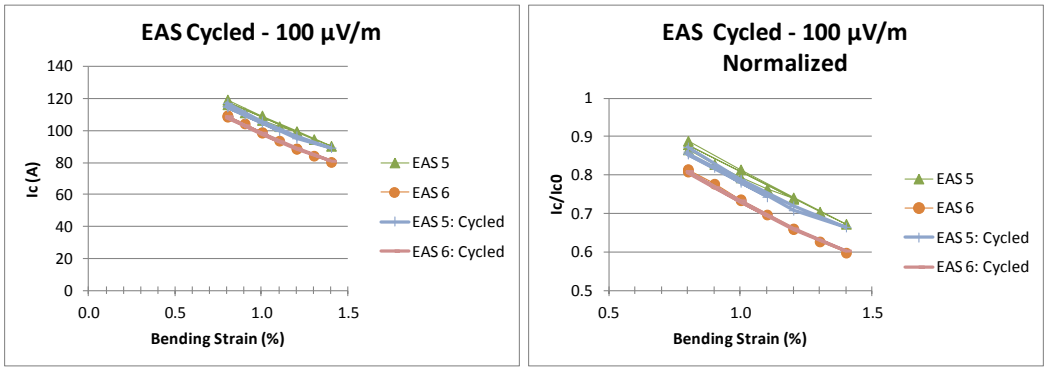

Figure 52 - Cycled EAS Results: High Bending Range

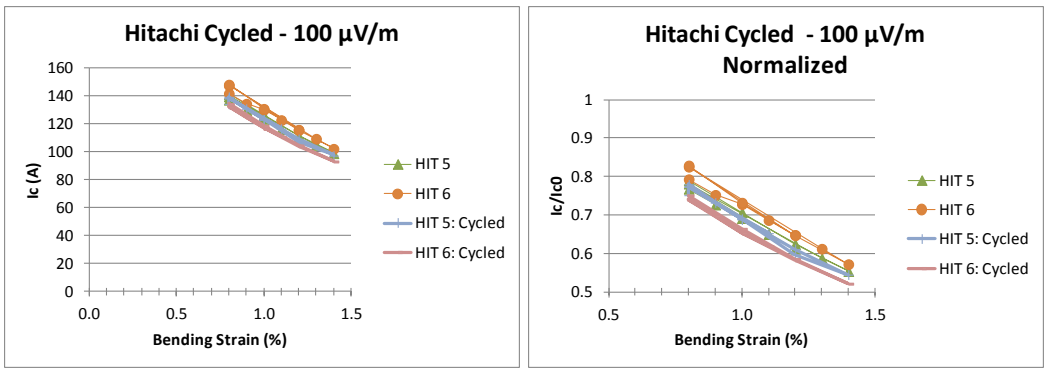

Figure 53 - Cycled Hitachi Results: High Bending Range

In order to better visualize the position of the critical current measurements for the cycled samples, it is important to plot them alongside the rest of the critical current measurements. The results for the Hitachi samples, which appear to exhibit slightly lower critical currents after additional cycling, are presented in Figure 54. The small difference in critical current is not nearly significant enough to account for the difference initially seen between the medium and high bending samples. It is clear at this point that the high bending sample holder produced repeatable results and that the samples are not particularly sensitive to load cycling at the strain values tested.

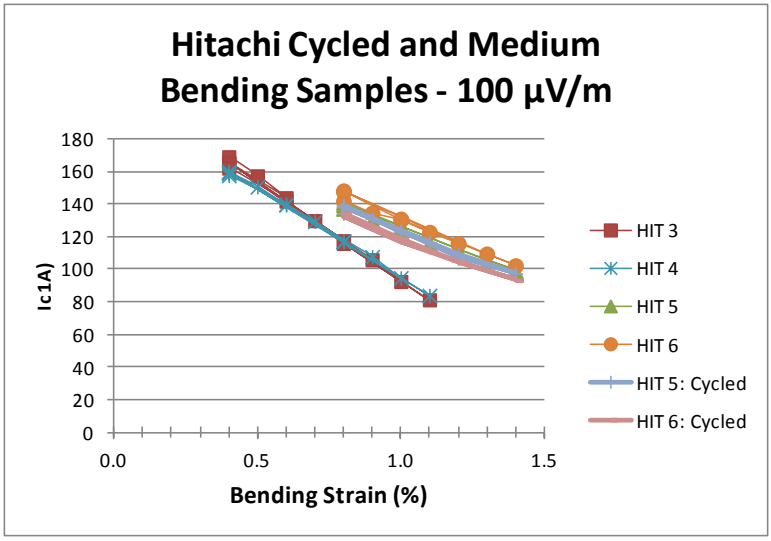

Figure 54 – Comparison of Hitachi Cycled and Medium Bending Samples

Another characteristic of the cycled samples to compare to the original test runs is the n-values calculated from the log-log plots. Although the exact trends of each sample are difficult to decipher from the n-value plots in Figure 55, it is clear that the cycled samples exhibited very similar transitions to their respective uncycled samples. For all the EAS and most of the Hitachi samples, the n-values at any bending strain were within a range of 6.

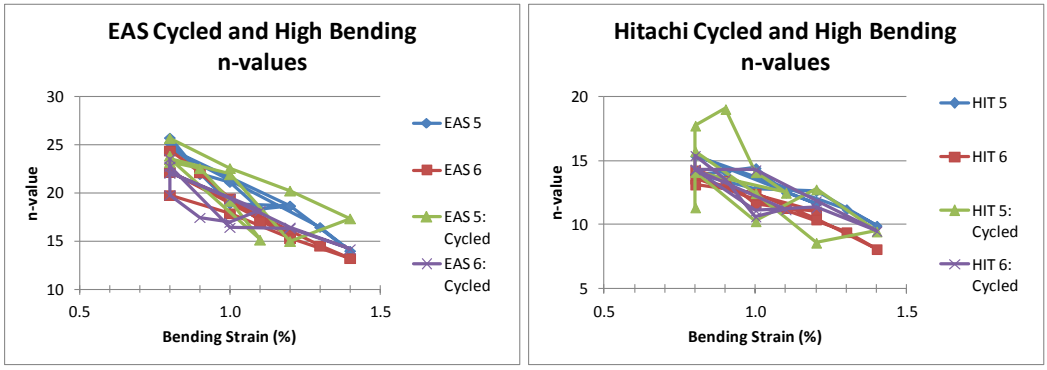

Figure 55 - Cycled and High Bending n-value Comparison

5.3.2 Full Range Cycled Samples

With additional time available at the NHMFL, more tests were run in an attempt to gain an increased understanding of the performance of the high bending sample holder and the Nb_3Sn strands. After concluding tests on the high bending range of 0.8-1.4%, strain was reduced in increments of 0.2% with tests being conducted for both current directions. The typical current direction is so that the Lorentz force acts toward the center of curvature when the samples are deformed, as shown in the left hand side of Figure 56. Testing outside the expected bending range of the sample holder and in both current directions was intended to help clarify the capabilities of the sample holder for the current values achievable by these samples. If the Lorentz load had a significant effect in deforming the sample out of the neutral axis or applying undesired strain, the critical current measurements would be significantly different from the standard current direction results.

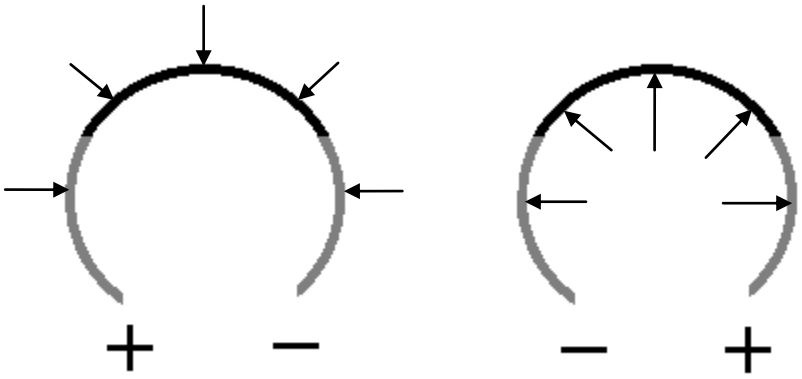

Figure 56 - Lorentz Force Direction Schematic. Left: Normal Current Direction; Right: Reverse Current Direction

Figure 57 plots the results for all the cycled samples with the normal current direction. Included on the plot are the low and medium bending range data for

reference. The original high bending range data is omitted for clarity and to avoid redundancy. For both the EAS and Hitachi samples, the data from the high bending sample holder closely match those of the low and medium bending sample holders up to around 0.5% bending strain. At this point, much of the critical current results for the low and medium bending sample holders drop off and show more significantly degraded performance.

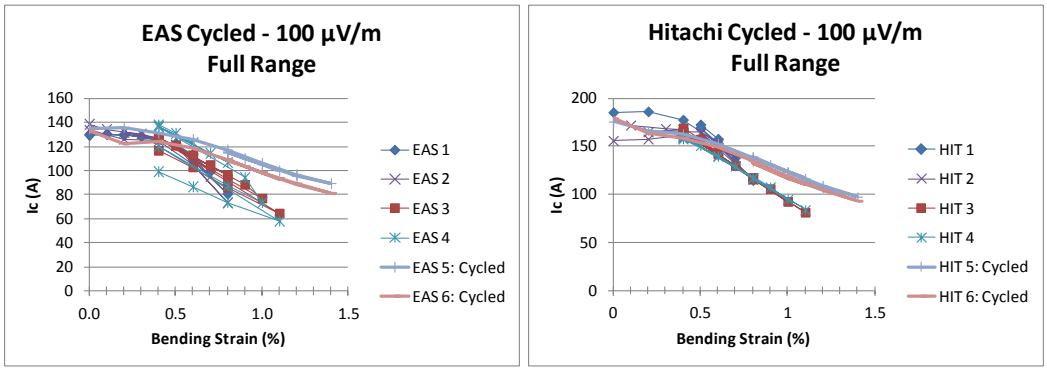

Figure 57 - Full Range Results for Cycled Samples

As noted earlier, the high bending sample holder was designed to support the Lorentz load expected at bending strains of 0.7-1.4%. However, the results that are consistent with the low bending range are an early indication that the high bending sample holder can support the strands through a full bending range of 0.0-1.4% for the bronze route Nb_3Sn strands tested in this study. The critical currents of the bronze route samples tested had lower critical currents relative to the design guidelines of the sample holders, resulting in a Lorentz load of less than 3 kN/m. The discrepancy in the medium bending range of approximately 0.6-1.1% bending strain may be explained by the low bending sample holder exceeding its accurate range of bending and the medium bending sample holder

being less accurate than expected. Finite element analysis for all three sample holders will be presented in a later section to further develop this concept.

Regarding the possibility of the high bending sample holder being suitable for the entire range of bending strain from 0.0% to 1.4%, two additional requirements needed to be met. First, the high bending sample holder needed to demonstrate that it would deform in a pure bending fashion across the entire range. Secondly, reversed current tests needed to be run to confirm that the Lorentz load on the samples did not have a significant effect.

5.3.3 Cycled Samples Voltage Tap Analysis

To further examine the first requirement, that of uniform pure bending, a similar approach to the initial investigation of the high bending sample holder was taken; the results from the short and long voltage taps were analyzed over the entire bending range. The following section contains this analysis for both EAS samples and one Hitachi sample, labeled 'EAS 5 Cycled,' 'EAS 6 Cycled' and 'HIT 6 Cycled.' The HIT 5 sample had a broken long voltage tap for most of the tests and thus was not analyzed for uniform pure bending.

As was the case before, the first step was to examine the raw voltage vs. current plots with the data from the short voltage tap, the long voltage tap and the difference between the two. Figure 58 consists of selected results for EAS 5 Cycled. The plots are displayed in order, left-to-right then top-to-bottom, representative of the tested order; testing began at 0.8% bending strain, increased to 1.4%, then decreased down to 0.0%. Again, in each plot, the blue line

represents the short voltage tap, the red line represents the long voltage tap and the green line represents their difference.

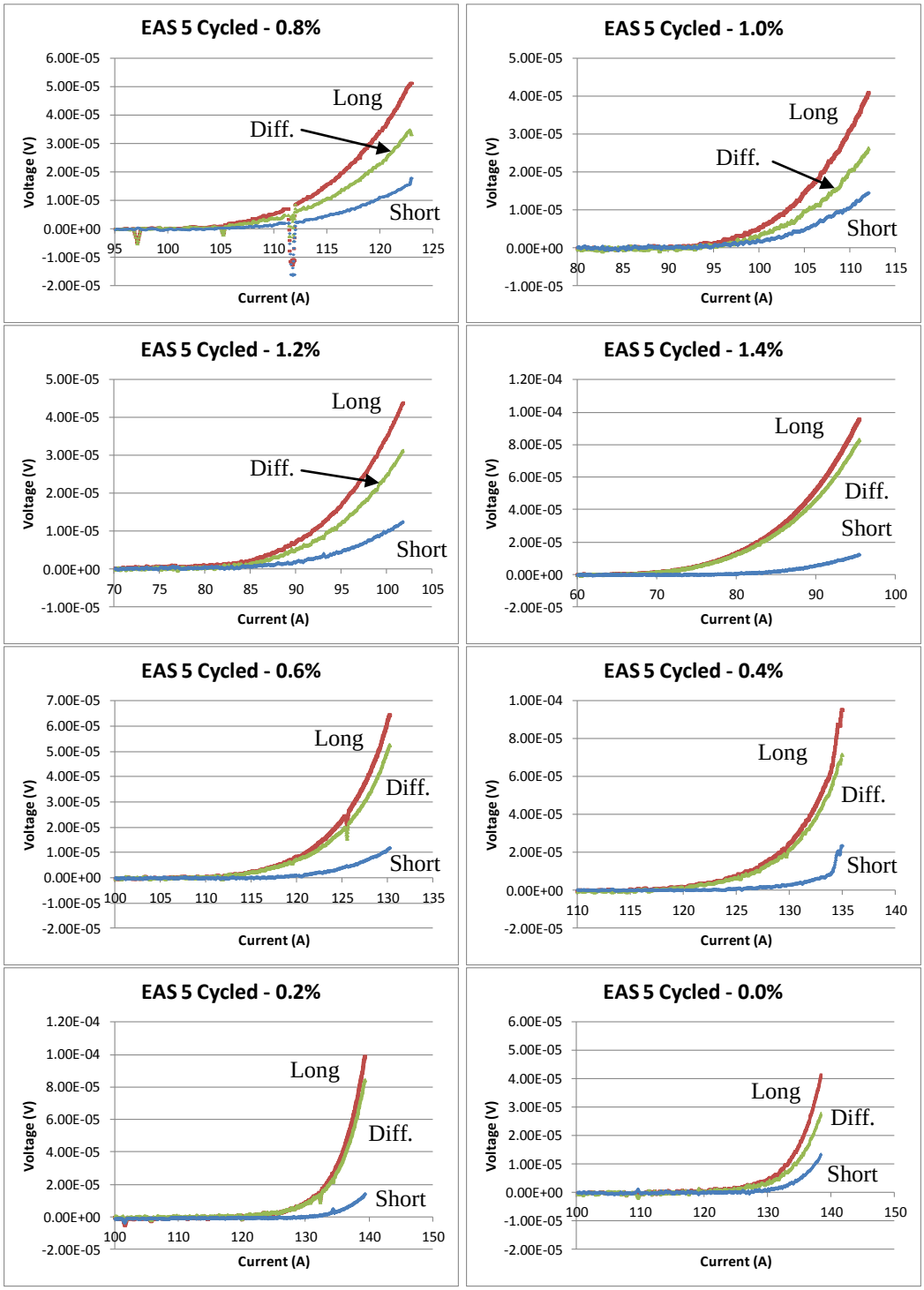

Figure 58 - Voltage vs. Current Voltage Tap Analysis for EAS 5 Cycled Sample

The results at the higher end of bending strains match well with the initial results of the samples that did not experience the extra cycling. The voltage across the outer sections of the sample, represented by the green line, trends toward the long voltage as strain increases from 0.8% to 1.4% bending. As the applied strain is reduced below the original 0.8% toward 0.0% bending strain, the difference results also tend very strongly toward the long voltage tap results. Results were similar for the other two samples tested, though the HIT 6 sample did not display as drastic a trend at the lower end of the bending range.

The next step was to further process the data to calculate the critical current values from each voltage tap. The critical current and normalized critical currents results are plotted in Figure 59 for the cycled EAS 5 sample, Figure 60 for the cycled EAS 6 sample and Figure 61 for the cycled HIT 6 sample. The results for all three samples are consistent throughout the entire 0.0-1.4% range of bending strain. In all three cases, there is slight deviation at 1.4% bending strain, but it is not particularly significant at 13 A or 9% of the maximum critical current. Although the EAS 6 sample had originally shown the least variability in voltage tap results, here the EAS 6 Cycled sample showed the largest spread, though still within 10% of the maximum critical current.

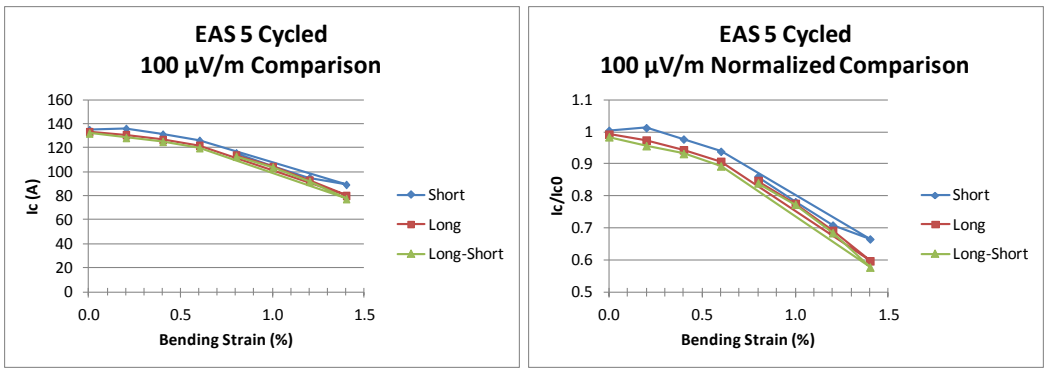

Figure 59 - EAS 5 Cycled Voltage Tap Analysis: Critical Current Results

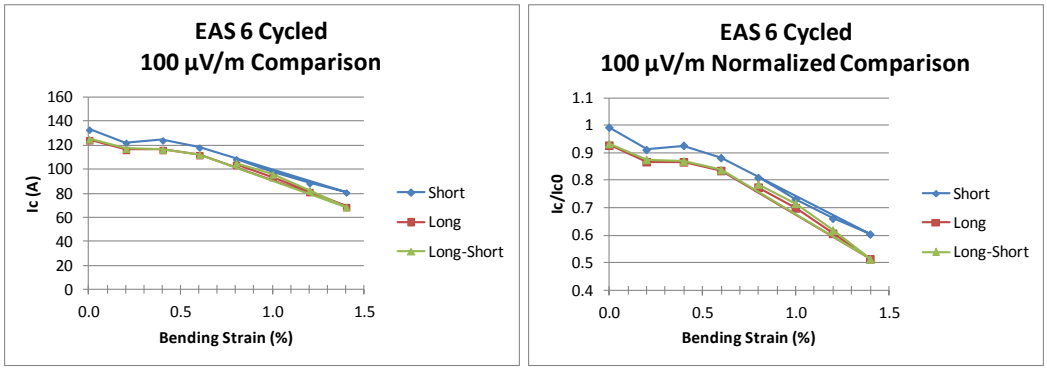

Figure 60 - EAS 6 Cycled Voltage Tap Analysis: Critical Current Results

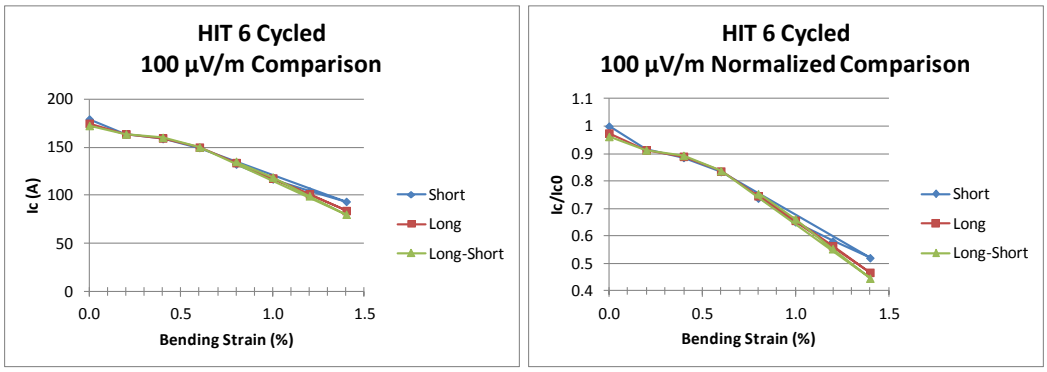

Figure 61 - HIT 6 Cycled Voltage Tap Analysis: Critical Current Results

The critical current results for the cycled test samples greatly increased confidence in the high bending sample holder's ability to deform uniformly. Another important property of the superconducting samples that needed to be

investigated for each voltage tap was the n-value. Representing the rate at which the samples transition from the superconducting to resistive state, the n-value would be expected to remain relatively constant for any single bending strain and decrease slightly as bending strain is increased. Figure 62 displays the n-values for the EAS 5 cycled sample; Figure 63 displays the n-values for the EAS 6 cycled sample and Figure 64 displays the n-values for the HIT 6 cycled sample. With just a few exceptions, the n-values, which are more subject to variation than critical current, are very similar in magnitude for each of the three voltage tap measurements analyzed.

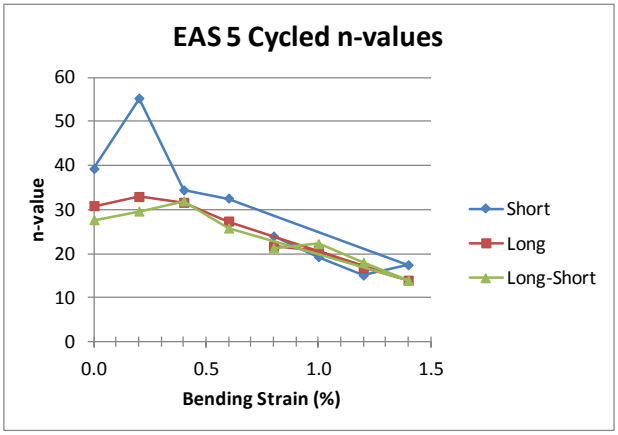

Figure 62 - EAS 5 Cycled Voltage Tap Analysis: n-values

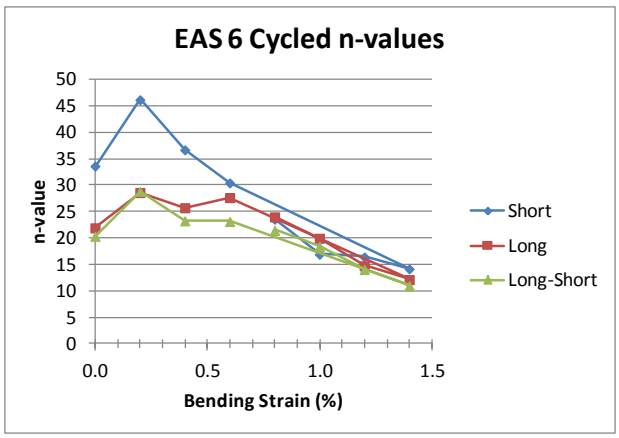

Figure 63 - EAS 6 Cycled Voltage Tap Analysis: n-values

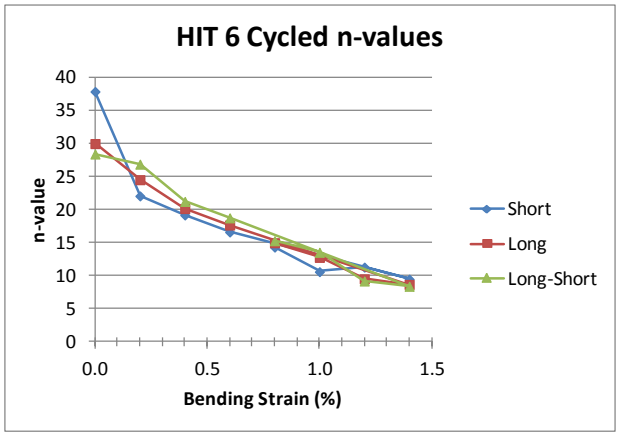

Figure 64 - HIT 6 Cycled Voltage Tap Analysis: n-values

Combining this voltage tap analysis with the results that corresponded well with those from the low bending sample holder, it appeared the high bending sample holder was able to cover the entire bending range from 0.0-1.4%. While the high bending sample holder was originally designed for a range of 0.7-1.4% bending, the expected critical current of an undeformed sample for that design was 350 A at 12 T. The greatest undeformed critical current of the samples tested in this study was under 200 A at 15 T, with a maximum value of 186 A for the 100 μV/m criterion. Thus, the high bending sample holder could support the Lorentz

load of a sample deformed less than the originally proposed minimum range value of 0.7%. Another subset of tests that used a reversed current direction was performed to help reinforce this conclusion.

5.3.4 Reverse Current Testing

The normal current direction used for all the tests to this point resulted in a Lorentz force that acted inward on the bent samples. In order to better understand the magnitude of the Lorentz load effect on the samples, the current direction was reversed, making the force act in an outward direction.

The critical current results for the reverse current direction EAS and Hitachi samples are plotted in Figure 65. Included in the plots are the critical current values for the cycled samples. Since the results come from the same samples and loading, the results should be identical if the Lorentz load has no effect on the deformation of the sample or the sample holders. Such a scenario would indicate that the sample holder was able to adequately support the sample, preventing substantial deviation from the nominal bending strain applied and localized strand deformation. As can be seen in the two plots of Figure 65, the reverse current results were very similar to the regular current direction results. The most significant differences for both the EAS and Hitachi wires was at 0.2% bending strain, with a critical current difference of approximately 9 A. For the EAS samples, this represented a difference of 7% of the maximum critical current; for the Hitachi samples, the difference was just 5.5%. The critical current differences at all other strain values were within 5% of the maximum critical current for each sample.

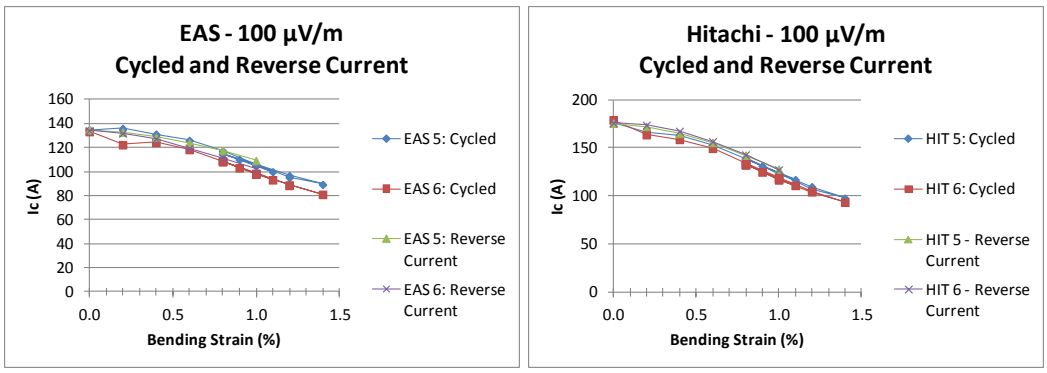

Figure 65 - Reverse Current Results: Critical Current

The raw voltage vs. current results for the HIT 6 reverse current sample voltage tap analysis are plotted in Figure 66. As in Figure 46 and Figure 58, the blue line represents the short voltage tap, the red line represents the long voltage tap and the green line represents their difference. The selected results that are presented here are representative of the results for all three analyzed samples. For all three samples, the green line representing the difference between voltage taps, consistently lies around the middle of the area between the two other curves for 1.0-0.2%, but closer to the long voltage tap at 0.0%. Such a behavior is not particularly concerning given the slight differences that may occur when the sample holder would ideally be perfectly straight.

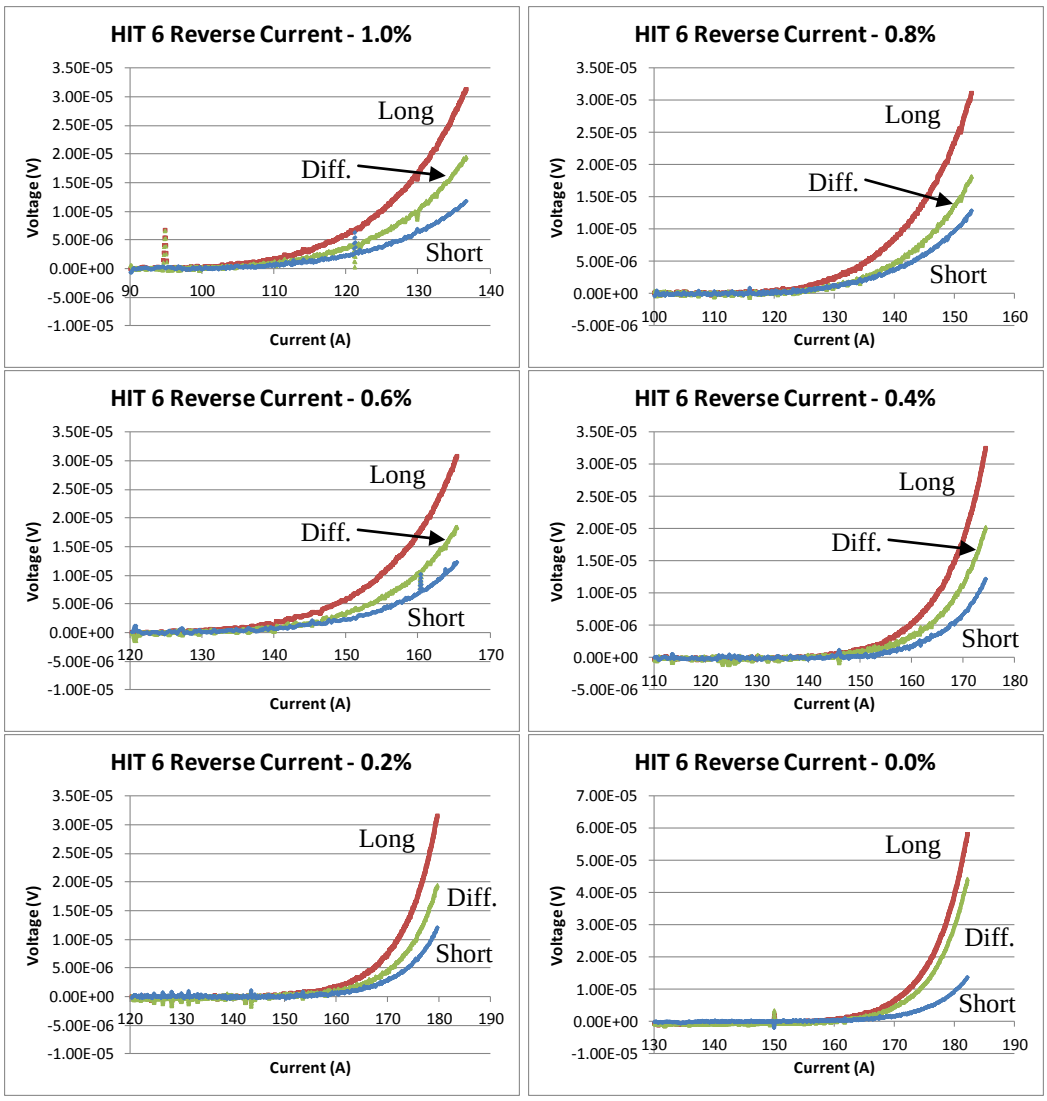

Figure 66 - Voltage vs. Current Voltage Tap Analysis for HIT 6 Reverse Current Sample

After performing some calculations to find the critical current from the voltage measurements for each voltage tap, the results for each sample were then plotted in Figure 67 for the EAS 5 reverse current sample, Figure 68 for the EAS 6 reverse current sample and Figure 69 for the HIT 6 reverse current sample. Like the critical current voltage tap analysis for the cycled samples, the results for the reverse current samples are remarkably consistent. The EAS 5 and HIT 6 samples had virtually identical critical current measurements for each of the long and short

voltage taps and the difference between them. The largest difference at any bending strain was 2.1 A for the EAS 5 sample and 3.8 A for the HIT 6 sample, though most differences were within 1 A. The EAS 6 sample again showed a slightly higher critical current across the short voltage tap, but at differences of around 5 A, they are not particularly concerning, especially since all the results fall within the range of results originally found for the low bending EAS samples.

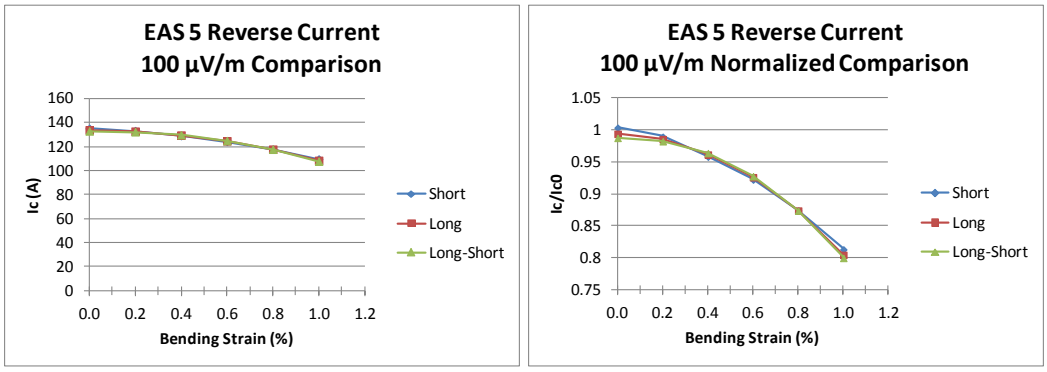

Figure 67 - EAS 5 Reverse Current Voltage Tap Analysis: Critical Current Results

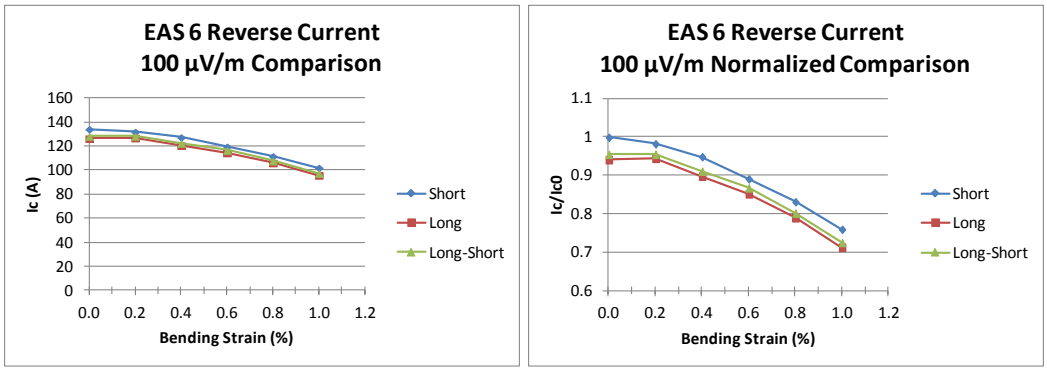

Figure 68 - EAS 6 Reverse Current Voltage Tap Analysis: Critical Current Results

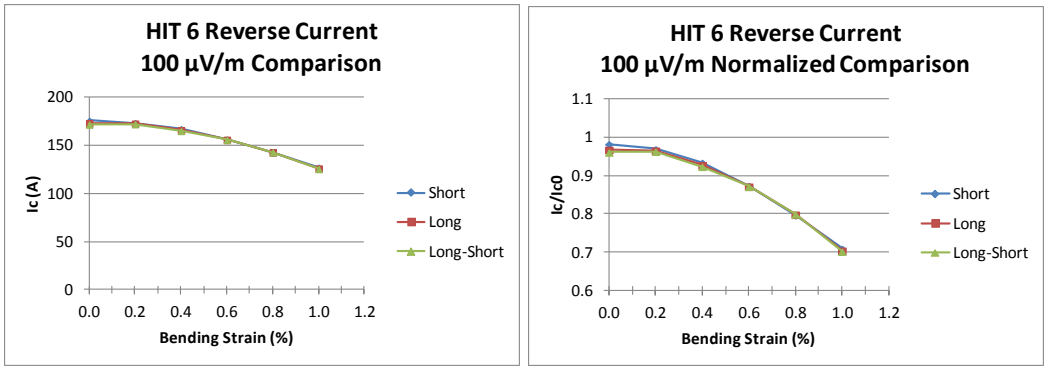

Figure 69 - HIT 6 Reverse Current Voltage Tap Analysis: Critical Current Results

A final step in investigating how uniformly the high bending sample holder bent was to plot the n-values for each voltage tap for the reverse current tests. The EAS 5 reverse current results are plotted in Figure 70; The EAS 6 reverse current results are plotted in Figure 71 and The HIT 6 reverse current results are plotted in Figure 72. The n-values again remain consistent for each of the voltage taps, though the short voltage tap does show some variation, particularly for the EAS 6 sample.

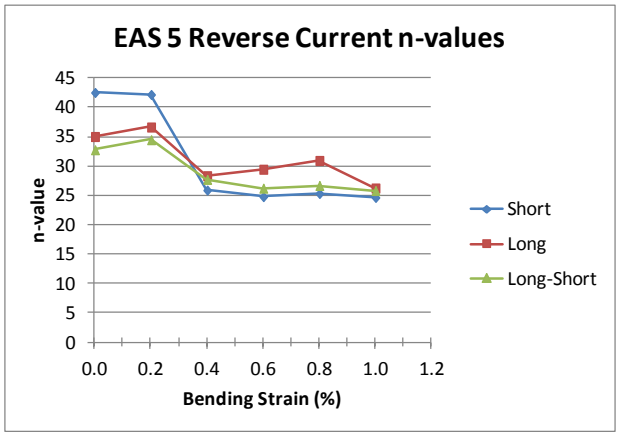

Figure 70 – EAS 5 Reverse Current Voltage Tap Analysis: n-values

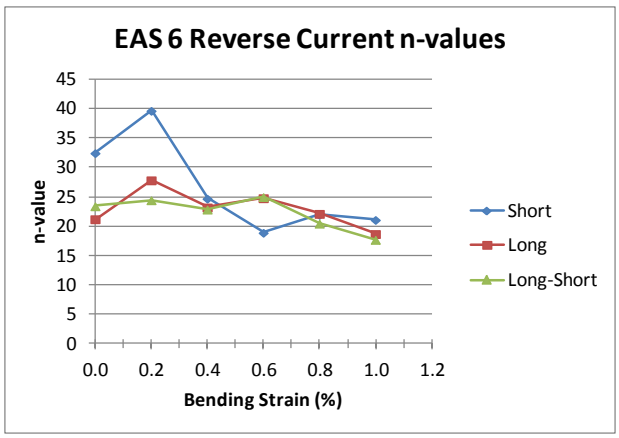

Figure 71 - EAS 6 Reverse Current Voltage Tap Analysis: n-values

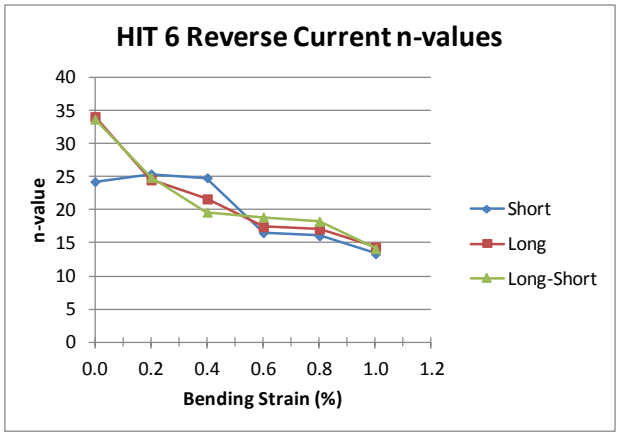

Figure 72 - HIT 6 Reverse Current Voltage Tap Analysis: n-values

Since the cycled and reverse current samples were tested across similar ranges, it might be worthwhile to compare the n-value results directly. The results for the EAS 5, EAS 6 and HIT 6 samples are plotted in Figure 73, Figure 74 and Figure 75, respectively. As can be seen in the plots, the n-values for both the cycled samples and the reverse current samples are very similar for all samples and bending strains except for a few strains around 0.2% for the EAS 5 and EAS 6 samples. Such consistency reinforces that the Lorentz load does not significantly alter the performance of the samples or the high bending sample holder.

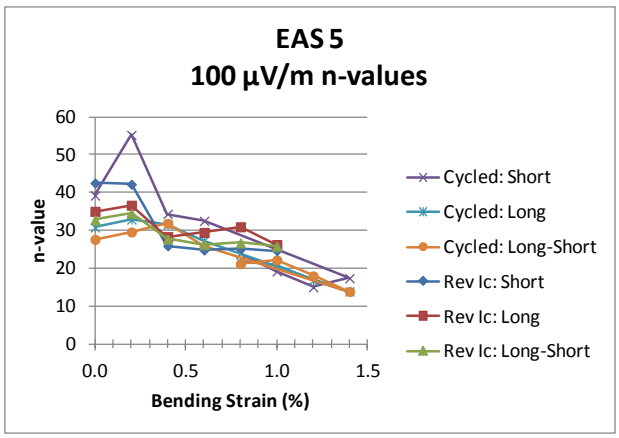

Figure 73 - EAS 5 Cycled and Reverse Current n-values

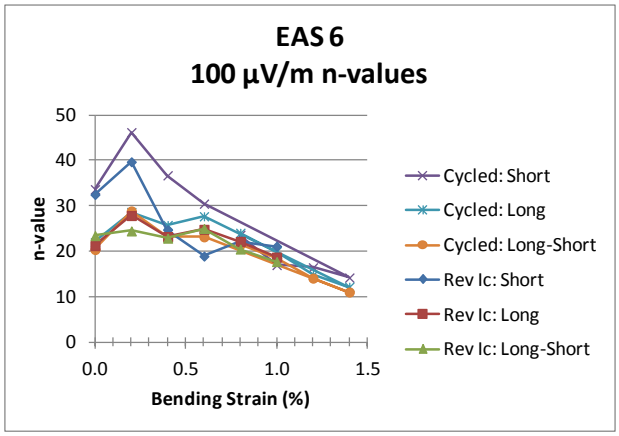

Figure 74 - EAS 6 Cycled and Reverse Current n-values

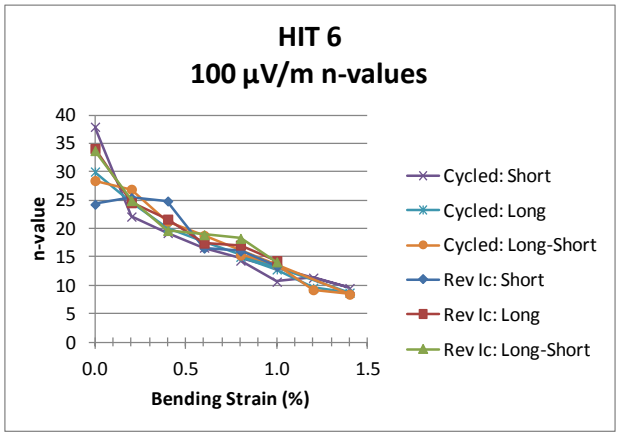

Figure 75 – HIT 6 Cycled and Reverse Current n-values

From the n-value, critical current and voltage results, it became clear that the Lorentz load was negligible for these high bending sample holders. There was no significant difference in critical current between current directions, therefore, the amount of bending or localized deformation from the Lorentz load was minimal. An important distinction to make, however, is that this was true for the specific bronze process Nb_3Sn strands tested in this study. Other samples, including internal tin Nb_3Sn strands, may have higher critical currents that could result in significant Lorentz load effects.

6. FINITE ELEMENT ANALYSIS

Along with the experimental data being used to characterize not just the superconducting Nb_3Sn strands, but also the sample holders, finite element analysis (FEA) is an ongoing effort to better understand the mechanics of the sample holder and how it affects the test wires. One known non-linear effect is the bowing or warping of the sample holder beam that can shift the neutral axis off the plane of symmetry [11]. Determining how significant this neutral axis shift is, as well as how uniformly the sample holder deforms can offer insight into experimental results and potentially prompt design modifications.

Models were prepared and run for each of the low, medium and high bending sample holders using the ANSYS software program. The models were slightly simplified in that the fillets at the base of each of the ribs were removed; making this change simplified the meshing process and reduced the required computing resources. Figure 76 shows an example of the model geometry used. In this case, the high bending sample holder is shown. Note that the major features of the

sample holders, specifically the ribs and channel, remained intact. The arms and connection between the sample holder and arms was simplified, however. Solid arms without current terminator blocks were used and the features at the end of the sample holders, where they mate with the current terminators, were eliminated to make a solid connection. The arms were cut into multiple volumes to make loading easier, providing edges to apply constraints and displacements. The final simplification was to cut the sample holder design in half and using a symmetry boundary condition. The arms were assigned linear elastic mechanical properties for stainless steel 316 at 4 K, with a Young's modulus of 2.014×10^5 MPa and a Poisson ratio of 0.33. The sample holder beam was assigned a bilinear isotropic material model for Ti-6Al-4V at 4 K, with a Young's modulus of 1.3259×10^5 MPa, a Poisson ratio of 0.34, a yield stress of 1758.2 MPa and a tangent modulus of 17237 MPa.

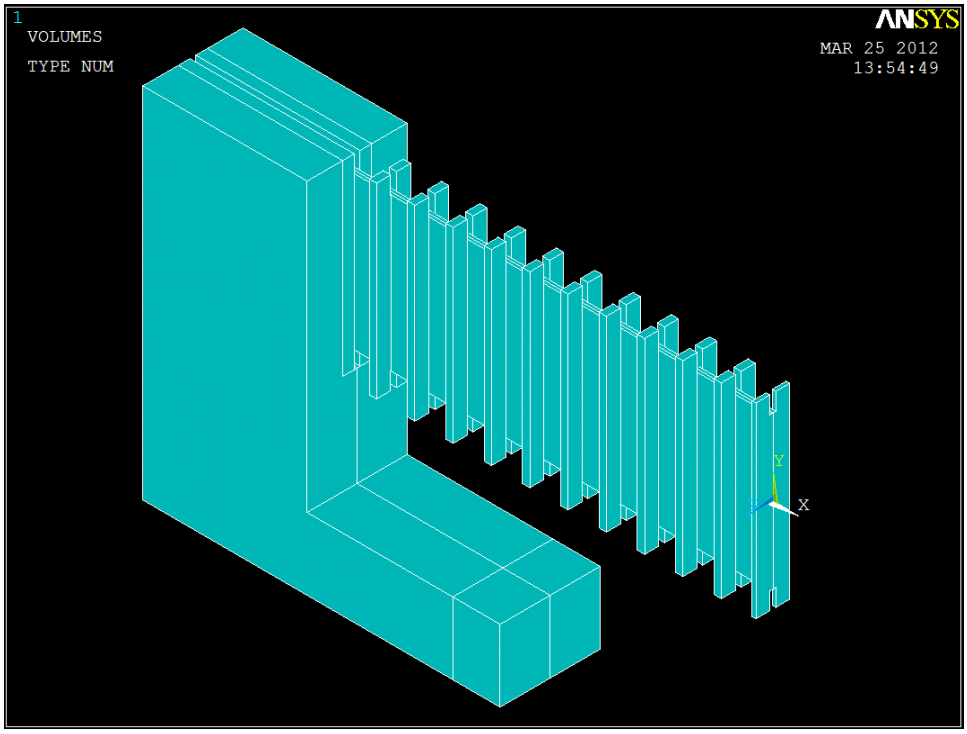

Figure 76 - High Bending Sample Holder Finite Element Model - Geometry

The strain along the beam at various locations in the channel was examined to determine how consistently the channel deformed and to determine the position of the neutral axis relative to the symmetry line. Additionally, the deformed shape of the sample holders was examined.

6.1 Meshing

Meshing used the SOLID95 tetrahedral elements in ANSYS. These are solid elements with 20 nodes at the element vertices and edge midpoints. Due to the complex nature of the geometry, featuring very small dimensions in some areas and larger, less critical areas elsewhere, a uniform mesh was neither necessary nor optimal. The large, featureless volumes, such as the arms, did not require a fine mesh, but the sample holder beam itself did. While a fine mesh could have been

used throughout, the number of elements would have become excessive and caused long computation times. Thus, instead of using a uniformly fine mesh throughout the model, only the most critical areas were finely meshed, while the rest of the model was coarsely meshed. A view of the overall mesh for the medium bending sample holder is shown in Figure 77.

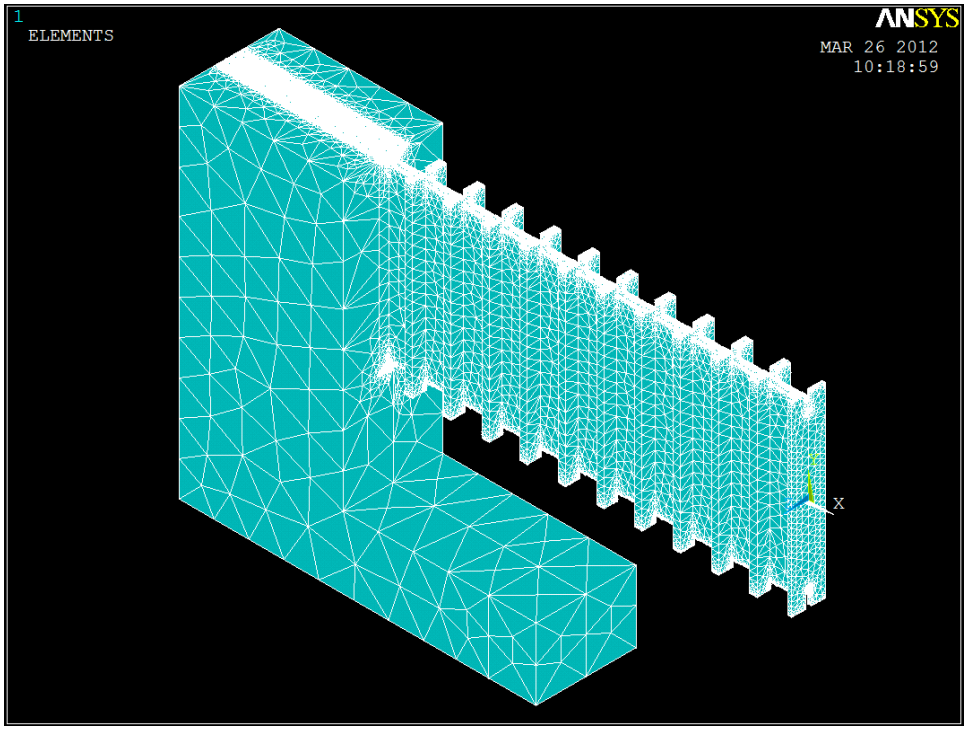

Figure 77 - Medium Bending Sample Holder Mesh

Since the areas of greatest interest and most complex geometry were around the channels at the top and bottom of the sample holders, these areas were most finely meshed. Using the mesh tools in ANSYS, the lines and surfaces in these regions were prescribed specific element sizes to ensure that at least two elements spanned the thinnest dimension of every feature. Although more elements through these thicknesses would have been ideal, the features were too small to obtain a finer mesh that would still result in reasonable computation times.

Transition parameters were then set to appropriately coarsen the mesh as it moved away from these critical regions. A detail of the mesh where the samples sit in the high bending sample holder can be seen in Figure 78.

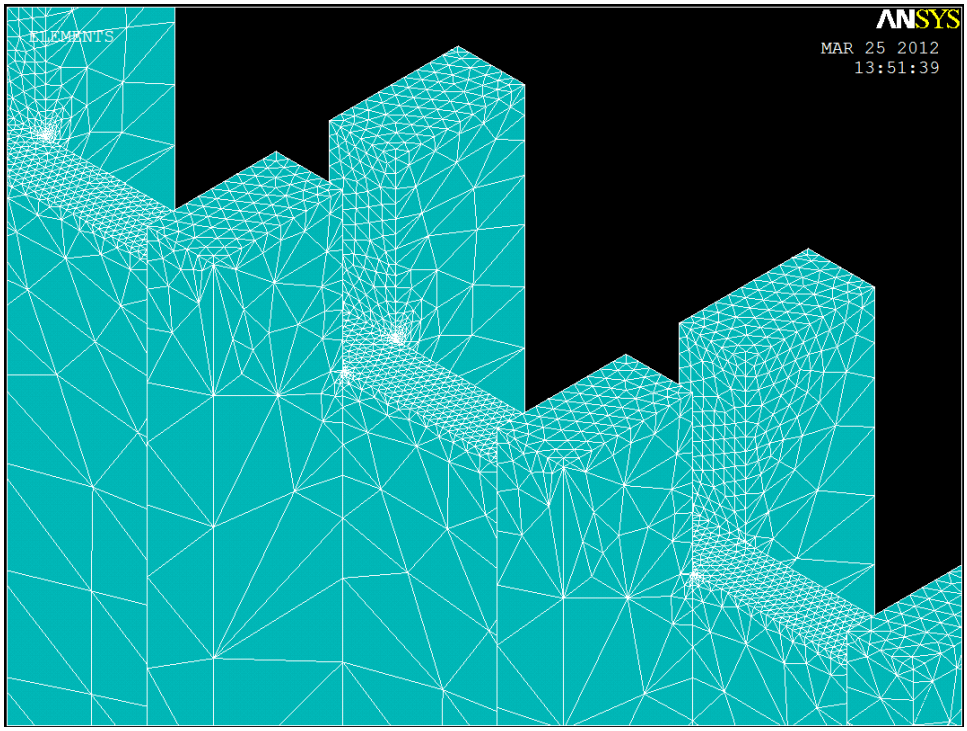

Figure 78 - High Bending Sample Holder Mesh Detail

6.2 Loading

The models for the low, medium and high bending sample holder were all analyzed at 0.6% bending strain. In order to apply this load, a few calculations needed to be completed and translated to a suitable form for ANSYS. The load application during experimentation is simply a rotation of the arms around the torque shaft; however, the solid elements in ANSYS cannot simply be given a rotational input. To work around this, the nodes along the axis of rotation were fixed in the translational degrees of freedom, but free to rotate. A displacement

was then prescribed to a line on the outer edge of the arm. This setup effectively allows the arms to rotate up to 90° from its original position. The required displacement to reach the 0.6% bending strain desired was calculated based on the length of the arm and the angle of rotation for 0.6% bending.

Additional loading and boundary conditions were necessary to fully define the model. Since only half of a sample holder was being modeled and analyzed, a symmetry boundary condition needed to be applied to the open face of the sample holder beam. This condition ensured that the surface remained in its original plane to maintain the continuity that would exist across this surface if the full sample holder was modeled. The bottom surface of the arms was constrained to remain in its plane to keep all deformation in a single plane.

In addition to the 0.6% bending strain load case, the high bending sample holder was also analyzed at 1.0% bending strain. The procedure for this load case was the same as for the 0.6% case, but with a larger displacement applied to the end of the arm.

A final run was made for the high bending sample holder at 1.4% bending strain. Since this case required the arms to be rotated more than 90°, a different means of applying bending strain was needed. While the symmetry plane and axis of rotation constraints remained the same as the previous models, the rotation was applied with a pilot node. A node was created with the TARGE170 element type at the base of the axis of rotation and rigidly connected to the bottom surface of the arms with CONTA174 elements. Rotation was then directly applied to the pilot node.

6.3 Results

Two key results were examined for the sample holder deformation. First, the variation in strain along the length of the sample holder was examined to better understand how uniformly the sample holder deformed and the position of its neutral axis relative to the symmetry line. This strain, in the direction along the length of the holder, will be referred to as longitudinal strain. Second, the deformation results were compared to the ideal circular deformation.

For all three sample holders, the longitudinal strain showed a periodic behavior along the length of the sample holder, caused by the ribs. The measurements were taken from three lines on the bottom surface of the channel: the symmetry line in the middle, the line forming the outer edge of the deformed channel and the line forming the inner edge of the deformed channel. An example of the graphical results in ANSYS from the medium bending sample holder can be seen in Figure 79.

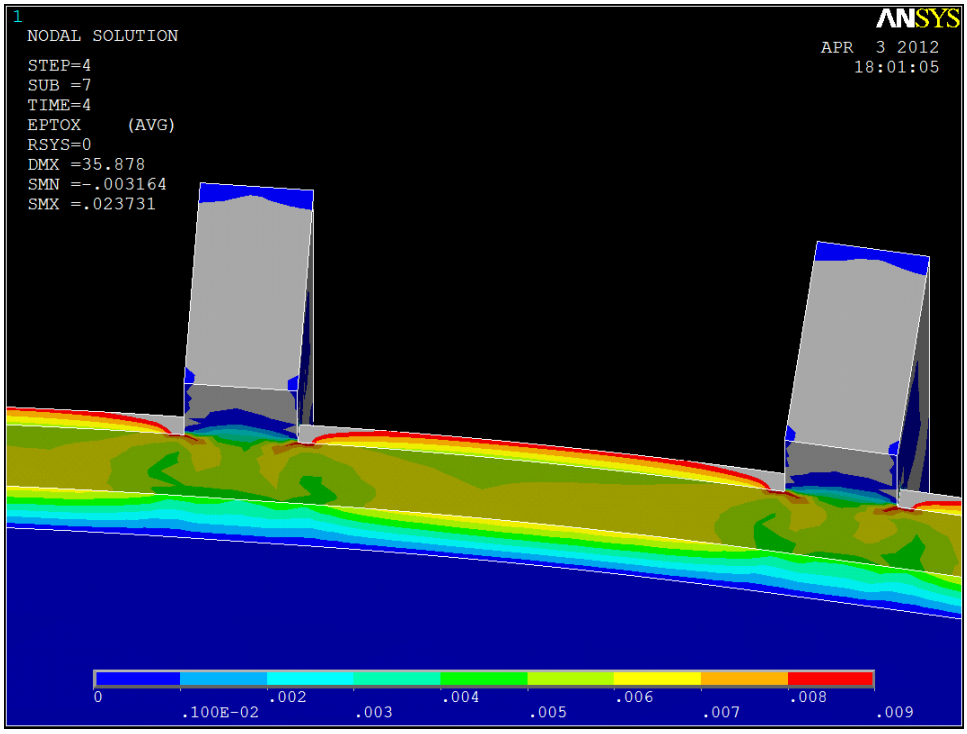

Figure 79 - Medium Bending Sample Holder Graphical Results

6.3.1 Longitudinal Strain Results

The results for the low bending sample holder are plotted in Figure 80; the strain results for the medium bending sample holder are presented in Figure 81; and the high bending sample holder results are plotted in Figure 82. A secondary detail plot of the symmetry line results is included in each figure.

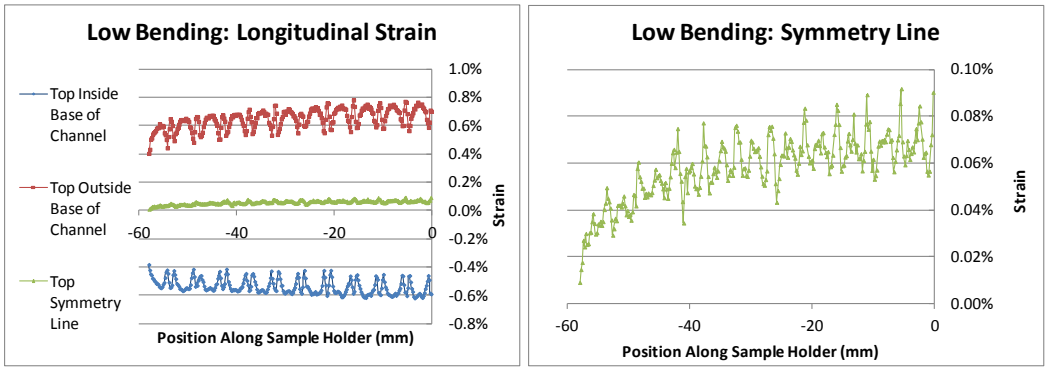

Figure 80 - Low Bending Sample Holder Strain Results - 0.6% Bending

The low bending sample holder exhibited a periodic strain fluctuation of approximately 0.2% in both the tensile and compressive regions. The strain fluctuation occurs due to the geometry of the ribs and channel walls along the length of the sample holder. The lowest magnitude strains are found at the edge of the ribs, with strain magnitudes peaking in the middle of the ribs and in the middle of the sections with only the thin channel wall. The magnitude of the strain decreases toward the connection to the arms. The strain on the outside curvature, or the tension side, has a magnitude ranging from 0.4% at the end of the beam to just under 0.8% closer to the symmetry plane. The strain on the inside curvature, or compression side, however, only ranges from 0.4% to just over 0.6%. This difference and the small amount of tension present along the geometric symmetry line are indications that bowing effects caused the neutral axis to shift toward the inside of the curvature. In the detail plot, it can be seen that the tension along the symmetry line is minor, with a maximum magnitude of less than 0.1%.

Within the span of the short voltage tap, ranging from the symmetry plane to the end location of the tap, or 0 to -25 on the horizontal axis of Figure 80, the strain magnitude range remains largely constant, for the tensile side, compressive side and symmetry line.

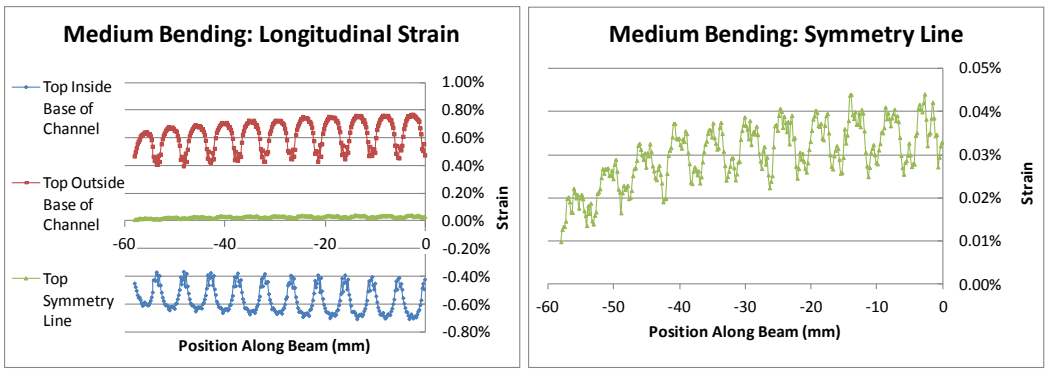

Figure 81 - Medium Bending Sample Holder Strain Results - 0.6% Bending

Similar trends developed for the medium bending sample holder with a few key differences. First, the strain fluctuation increased to 0.3%, displaying a range of 0.5-0.8% longitudinal strain near the symmetry plane. The larger range indicates that the dimensions of the medium bending sample holder's channel may have caused greater variation in the deformation of the samples along the length of the sample holder. A finite element model that includes a wire in the channel, currently in development, could further develop or disprove this concept by determining how the sample holder deformation translates to the sample wire. Also, the high magnitude peaks are only present between ribs; the strain remains at a low magnitude throughout the width of each rib. Similarly to the low bending sample holder, the strain for the medium bending sample holder decreases close to the connection to the arms, where the fluctuation decreases to just over 0.2%.

The strain along the geometric symmetry line is again on the tensile side, but at a lesser magnitude. As can be seen in Figure 81, the maximum strain along the symmetry line for the medium bending sample holder is slightly more than 0.04%, about half that of the low bending sample holder. A final similarity to the

low bending sample holder results is that the overall magnitude of the strain does not vary across the span of the short voltage tap.

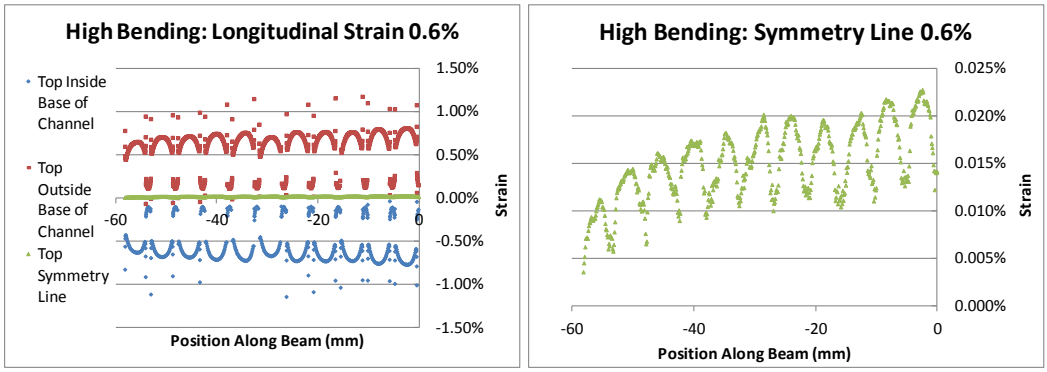

Figure 82 - High Bending Sample Holder Strain Results - 0.6% Bending

The high bending sample holder also showed the period trends that the low and medium bending sample holders exhibited. An important note regarding the geometry and results for the high bending sample holder relate to the peaks and valleys. Since the fillets along the ribs were removed for modeling ease, a small extra edge and sharp corner existed where the ribs meet the channel. This introduced a discontinuity and localization of strain that is not representative of the actual sample holder. Thus, the discontinuous peaks and valleys around the ribs plotted in Figure 82 and Figure 83 were artificially high. The rest of the results still provided valuable information, though.

The high bending sample holder showed a fluctuation of approximately 0.2% strain in the section between ribs. At the end of the sample holder, closer to the arm, the tensile range spanned from slightly more than 0.4% to more than 0.6%, while the range was approximately 0.6-0.8% close to the symmetry plane of the sample holder. Unlike the low bending sample holder, however, the compressive side exhibited strain magnitudes very similar to the tensile side. Additionally, the

magnitude of tension along the symmetry line was further reduced in comparison to both the low and medium bending sample holders. The combination of these two results indicates that the high bending sample holder maintains the position of the neutral axis closer to the symmetry line at 0.6% bending.

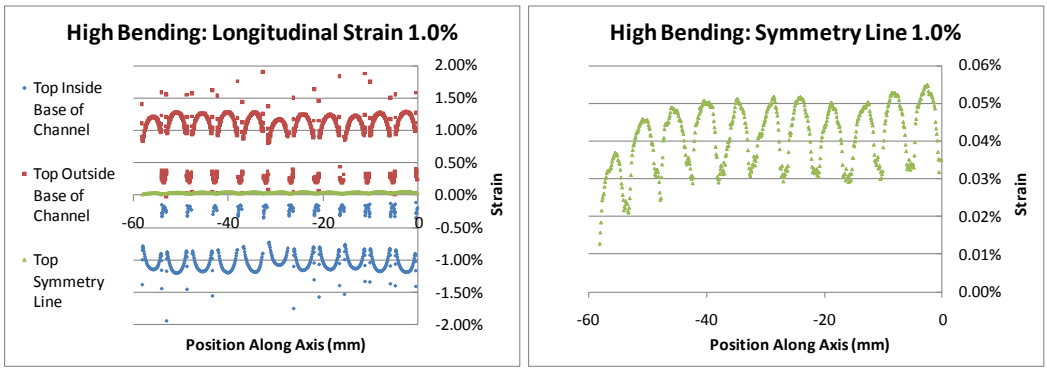

Figure 83 - High Bending Sample Holder Strain Results - 1.0% Bending

The general trends of the high bending sample holder results at 1.0% bending strain were in line with the results at 0.6%. The total strain magnitude was higher, but with a greater applied strain, those results were logical. The tensile strain range across the entire sample remained relatively consistent along the entire length of the sample holder at approximately 0.9-1.3% strain. The magnitude of the compressive strain range is again very similar to the tensile range, but slightly less at 0.8-1.2% strain. The strain magnitude along the symmetry line was also higher than the 0.6% results for the high and medium bending sample holders, but actually less than for the low bending sample holder. The strain remained mostly within the range of 0.03-0.05% along the symmetry line except at the end by the arms where the strain decreased to around 0.02%.

The strain results for the 1.4% bending strain load case, plotted in Figure 84, different from the lower bending load cases in one significant way. Unlike the 0.6% and 1.0% bending load cases, the strain increases in magnitude close to the connection to the arms. The higher strain values outside the span of the short voltage tap match well with the voltage tap analysis performed on the experimental results. Recall that experimental results consistently showed that the short voltage tap measured higher critical currents than the long and difference voltage taps in the 1.3-1.4% bending range, such as in Figure 47 and Figure 60. These experimental results indicated that the middle of the sample area deformed less than the edges, a concept that is supported by the FEA results for the 1.4% bending strain case. A strain fluctuation of 0.4% occurs close to the symmetry plane, ranging from approximately 1.2% to 1.6% on the tensile side. The strain fluctuation increases to about 0.7% close to the connection to the arms, covering a range of 1.3-2.0% on the tensile side.

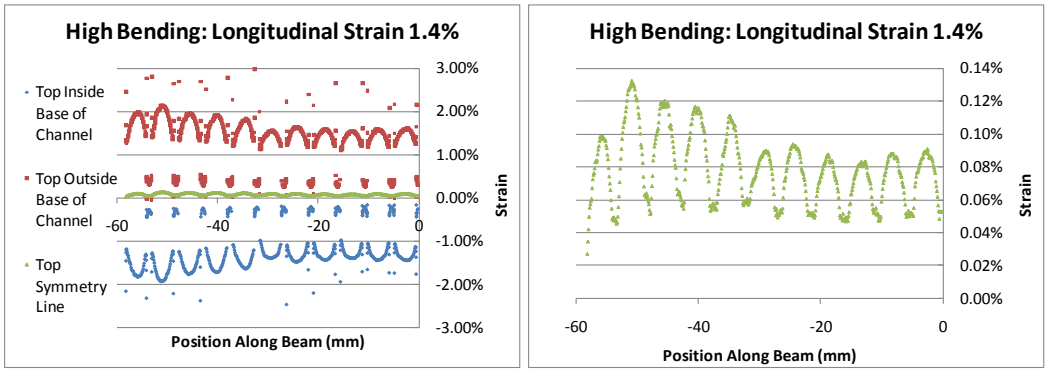

Figure 84 - High Bending Sample Holder Strain Results - 1.4% Bending

6.3.2 Circular Deformation Results

After analyzing the strain behavior along the length of each sample holder, the deformation of the symmetry line of each was compared to the expected circular deformation for 0.6% bending strain. The low bending deformation comparison is plotted in Figure 85; the medium bending sample holder results are shown in Figure 86; and the high bending sample holder results are displayed in Figure 87. In the plots, the vertical axis represents the location of the symmetry plane in the ANSYS models. All three sample holders demonstrated virtually identical deformation performance for 0.6% bending strain.

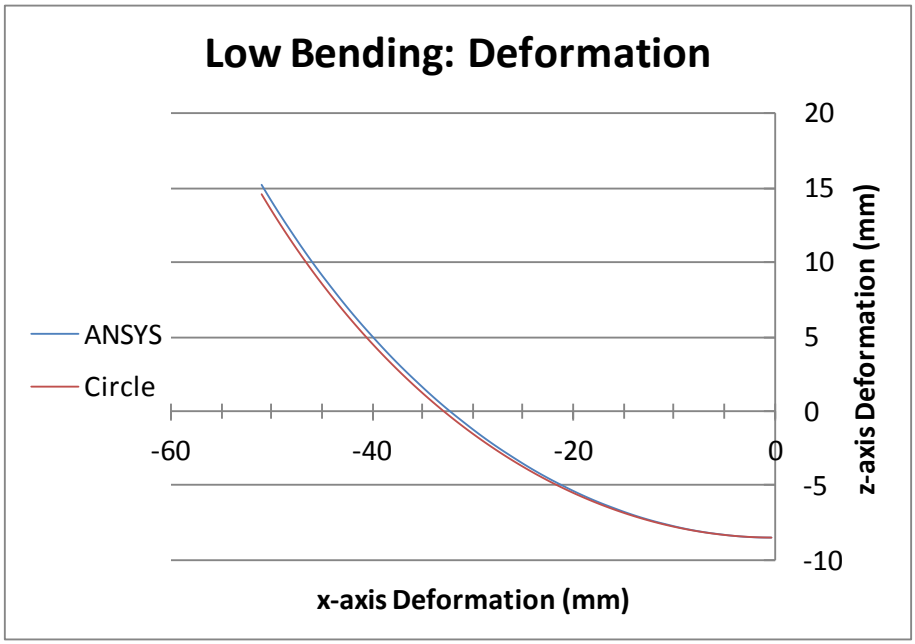

Figure 85 - Low Bending Sample Holder Circular Deformation Comparison

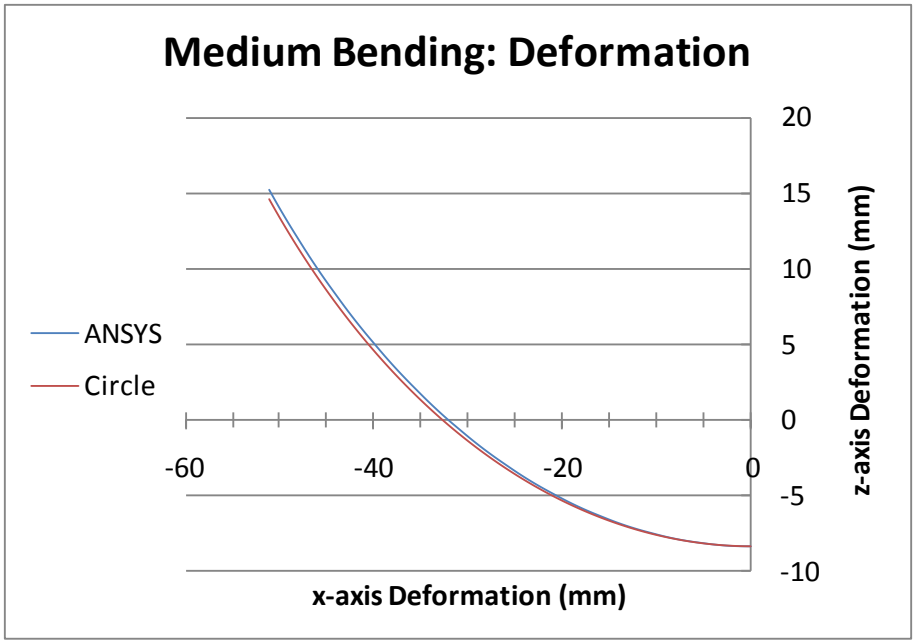

Figure 86 - Medium Bending Sample Holder Circular Deformation Comparison

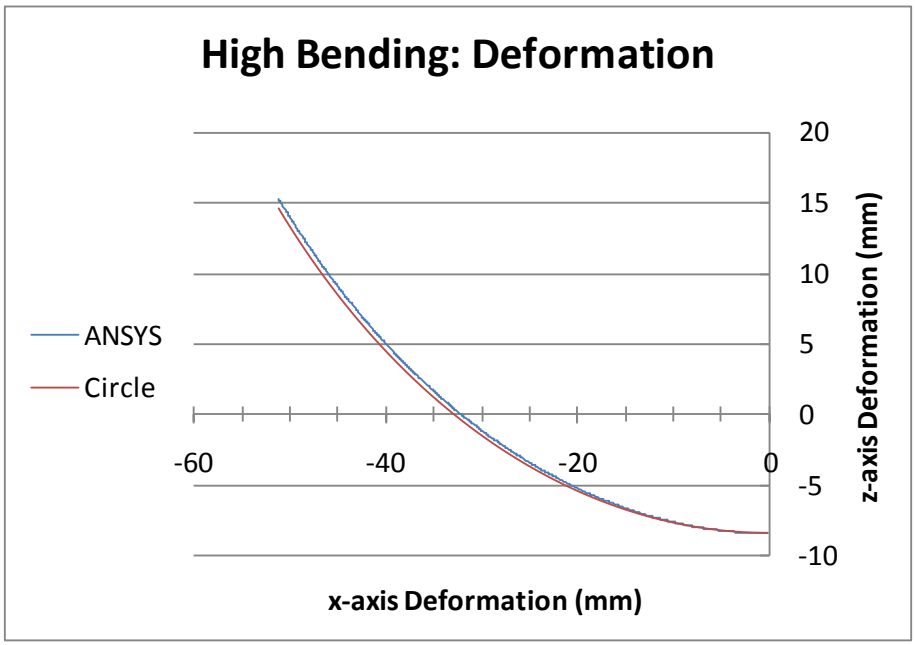

Figure 87 - High Bending Sample Holder Circular Deformation Comparison

For 0.6% bending strain, the greatest difference between the analytic deformation in ANSYS and the ideal circular deformation ranged between 0.642 and 0.676 mm; in all three cases, this largest displacement gap occurred at the very end of

the sample holders near the connection to the arms. All analytical deformation within the range of the short voltage tap, or approximately 25 mm from the symmetry plane, was within approximately 0.25 mm of the perfect circle deformation. Compared to the radius of curvature of 68.33 mm for 0.6% bending, these differences are minimal. Differences between the analytical z-deformation and the ideal circle z-deformation are plotted for the low bending sample holder in Figure 88, for the medium bending sample holder in Figure 89 and for the high bending sample holder in Figure 90.

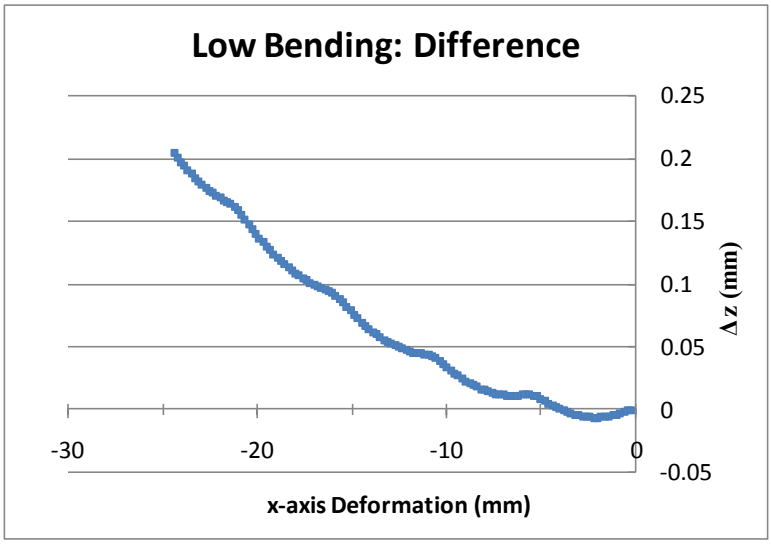

Figure 88 - Low Bending Sample Holder Circular Deformation Difference

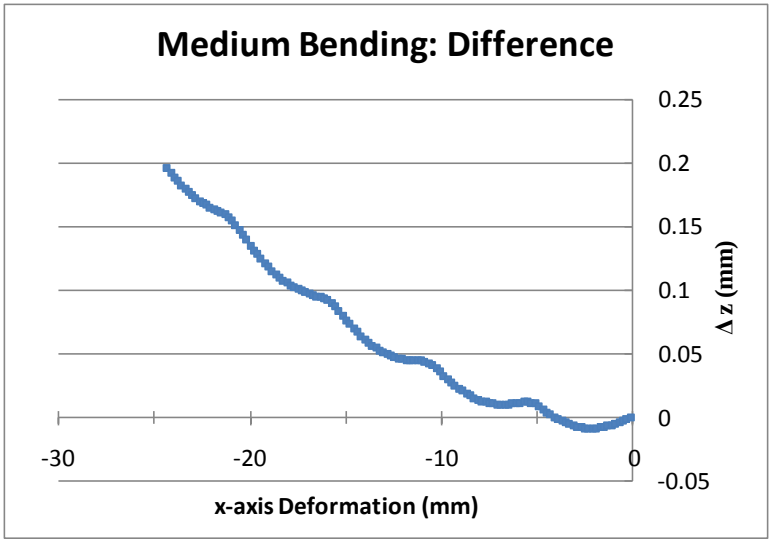

Figure 89 - Medium Bending Sample Holder Circular Deformation Difference

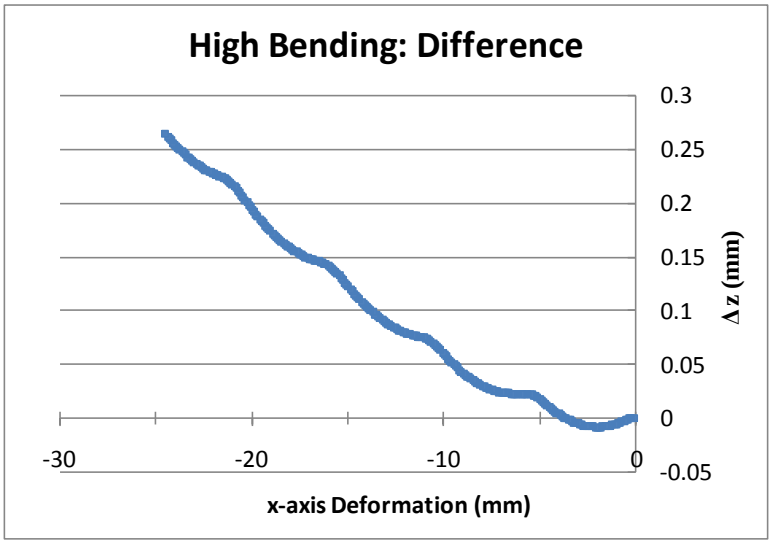

Figure 90 - High Bending Sample Holder Circular Deformation Difference

For the 1.4% bending strain load case, the difference between the ideal circular deformation and the deformation of the ANSYS model was significant. These results are plotted in Figure 91. The model showed less bending in the middle of the sample holder, elongating the deformed shape and showing more bending close to the connection to the arms. The maximum difference between the ideal

shape and the model's deformed shape was approximately 2 mm and occurred both within the span of the short voltage tap and toward the end of the sample holder. This 2 mm difference is approximately three times the magnitude of the maximum difference for the 0.6% bending load case, which did not occur close to the short voltage tap. Also factoring in that the radius of curvature for the 1.4% bending strain load case is just 29.29 mm, the magnitude of the difference in deformation is considerably more significant than for the 0.6% bending load case. These results further indicate that 1.4% bending strain exceeds the accurate bending range of the high bending sample holder.

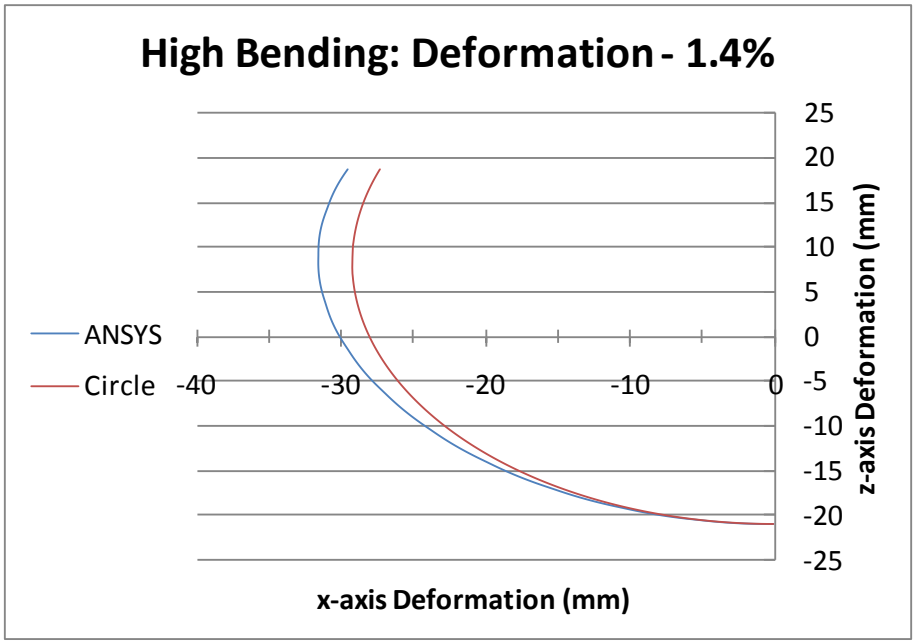

Figure 91 - High Bending Sample Holder Circular Deformation - 1.4%

7. CONCLUSIONS AND FUTURE WORK

This study of the effects of pure bending strain on the critical current performance of bronze route Nb_3Sn superconducting strands has yielded valuable information

about the strands themselves as well as the sample holders used for testing. Experimental results for EAS and Hitachi bronze route Nb_3Sn wires showed maximum critical currents at 15 T and 4.2 K to be approximately 135 A and 175 A, respectively. Only two samples, the EAS samples in the medium bending sample holder, seemed to show permanent degradation of critical current after a bending strain of 1.0%, while no other samples displayed permanent degradation even after reaching a nominal bending strain of 1.4%.

Critical current discrepancies between the medium and high bending range samples prompted a detailed study into the possible causes, including potential sensitivity to cycled loading and the performance of the sample holders. Additional testing showed that the EAS and Hitachi samples were not especially sensitive to the cycling of bending strain up to 1.4%, as additional cycling did not degrade the critical current performance of the samples. Testing the high bending sample holder below its design range and with a reverse current direction demonstrated that for the bronze route Nb_3Sn wires tested in this study, the high bending sample holder could deform and support the strands through a full bending range of 0.0-1.4% with minimal effects from the Lorentz loading. Further testing with the medium and high bending sample holder could help more precisely define and explain the critical current differences found in this research.

FEA has begun to shed light on the non-linear mechanical deformation of the sample holders. Early results indicate that all three sample holders deform in a mostly circular manner for 0.6% bending strain, but also that significant errors from the pure bending condition exist at 1.4% bending strain. The longitudinal

strain results indicate that the samples may not experience constant strain loading along the length of the sample holder, but future models that will include a sample strand should be able to provide more insight into how uniformly the test samples were deformed. In addition to finite element models that include the strands, future modeling efforts aim to include finer details of the sample holders, such as fillets, and to introduce potential design revisions to improve performance. Another goal is to make additional analytical runs at various bending strains to more completely characterize the behavior of the sample holders.

The testing and analytical modeling performed for this thesis has established a collection of quality data and a basis for design improvement. Additional testing could provide more data that would be of use in formulating empirical scaling laws to directly relate critical current performance to bending strain and testing conditions. Building a more comprehensive database of the strain effects on the critical current of Nb_3Sn wires will hopefully set the stage for design improvements for strand cross sections for their magnet applications.

8. APPENDIX

8.1 Low Bending Sample Holder ANSYS Code

```
! Load IGES file into ANSYS
/BATCH
/COM,ANSYS RELEASE 10.0    UP20050718       14:47:59    09/13/2011
/AUX15
IOPTN,IGES,NODEFEAT
!*
IOPTN,MERGE,YES
IOPTN,SOLID,YES
IOPTN,SMALL,NO
IOPTN,GTOLER, DEFA
IGESIN,'Bending_Model_LB_no_fillets','IGS',' '
VPLOT
!*
FINISH

/PREP7
ET,1,SOLID95   !Define element type
MPTEMP,1,4   !Define a temperature table, 4K
!Define material properties for Ti-6Al-4V
MPDATA,EX,1,1,132591.5  !MPa
MPDATA,PRXY,1,1,.34  !Poisson's Ratio
TB,BISO,1
TBDATA,1,1758.16,17237
!Define material properties for SS316
MPDATA,EX,2,1,201397.5
MPDATA,PRXY,2,1,.33

!Glue volumes
ALLS
VGLUE,ALL
!Divide volumes to create axes of rotation
WPCSYS
ALLS
VSBW,ALL
WPCSYS
WPOFFS,-37.79139,-36.970 !Move WP to left bending arm
WPROTA,,,-90
VSBW,1
VSBW,2

!Apply Ti material properties to sample holder
VSEL,S,,,5,6,1
VATT,1

!Apply SS material properties to bending arms
VSEL,S,,,1,3,2
VSEL,A,,,4,7,3
VATT,2

alls
```

```
vplo
save

!Mesh all parts with tetrahedral elements
ALLS
MSHAPE,1,3D
SMRTSIZE,1
SMRTSIZE, ,0.1,1,1.3,7,15,1.4,0,1,4,0

!Select lines to refine mesh on volume 5
LSEL,S,,,13,14
LSEL,A,,,45,47
LSEL,A,,,61,62
LSEL,A,,,82,96,14
LSEL,A,,,99,104,5
LSEL,A,,,107,124,17
LSEL,A,,,128
LSEL,A,,,136,137
LSEL,A,,,142
LSEL,A,,,154,155
LSEL,A,,,165,166
LSEL,A,,,176,177
LSEL,A,,,184,190,6
LSEL,A,,,218,230,12
LSEL,A,,,239,264,25
LSEL,A,,,267,268
LSEL,A,,,281,282
LSEL,A,,,289,290
LSEL,A,,,308,317,9
LSEL,A,,,327,333
LSEL,A,,,336,337
LESIZE,ALL,.2,,,,,,,1
!Select areas to refine mesh on vol 5
ASEL,S,,,18,20
ASEL,A,,,22
ASEL,A,,,117
ASEL,A,,,145
ASEL,A,,,149
AESIZE,ALL,.2
ASEL,S,,,3
ASEL,A,,,8
ASEL,A,,,25
AESIZE,ALL,.3
VSEL,S,,,5
VMESH,5

ALLS

!Select lines to refine mesh on volume 6
LSEL,S,,,3,8,5
LSEL,A,,,17,34,17
LSEL,A,,,38
LSEL,A,,,42,51,9
LSEL,A,,,54
LSEL,A,,,69,70
LSEL,A,,,77,83,6
```

```
LSEL,A,,,85,89,4
LSEL,A,,,95,101,6
LSEL,A,,,111,113,2
LSEL,A,,,132,161,29
LSEL,A,,,180,189,9
LSEL,A,,,196,197
LSEL,A,,,205,212,7
LSEL,A,,,217,226,9
LSEL,A,,,249,255,3
LSEL,A,,,288,294,6
LSEL,A,,,297,305,8
LSEL,A,,,307,326,19
LSEL,A,,,329
LSEL,A,,,332,333
LSEL,A,,,336
LSEL,A,,,340,343
LSEL,A,,,345
LESIZE,ALL,.2,,,,,,1
!Select areas to refine mesh on vol 6
ASEL,S,,,26,28
ASEL,A,,,30
ASEL,A,,,118
ASEL,A,,,146,148,2
AESIZE,ALL,.2
ASEL,S,,,4
ASEL,A,,,15
ASEL,A,,,32
AESIZE,ALL,.3
VSEL,S,,,6
VMESH,6

!Mesh remaining volumes
ALLS
VSEL,ALL
VSEL,U,,,5,6
VMESH,ALL

FINISH

!Define solution type
/SOLU
ANTYPE,STATIC
NLGEOM,ON                !Specify large deflection
NROPT,FULL               !Specify full Newton-Raphson option

NSUBST,20,200,0                  !Specify number of substeps
OUTRES,ALL,ALL                   !Write all data for all steps

!Fix axes
LSEL,S,,,261
DL,ALL,,UX,0
DL,ALL,,UY,0
DL,ALL,,UZ,0
ALLS

!Apply symmetry boundary condition
```

```
ASEL,S,,,24,31,7
DA,ALL,SYMM
ALLS

!Keep bases in-plane
ASEL,S,,,7
ASEL,A,,,33
ASEL,A,,,37
ASEL,A,,,42
DA,ALL,,UY,0
ALLS

!Apply displacement to outer line
LSEL,S,,,319
NSLL,S
D,ALL,UY,0
D,ALL,UZ,12.64          !WANT 32.64 mm DEFLECTION TOTAL FOR 0.6% BENDING
ALLS

!Apply zero load to load application line
LSEL,S,,,370
NSLL,S
F,ALL,FZ,0
ALLS

SOLVE

!Second load step
LSEL,S,,,319
NSLL,S
DCUM,ADD
D,ALL,UZ,10
ALLS
SOLVE

!Third load step
LSEL,S,,,319
NSLL,S
DCUM,ADD
D,ALL,UZ,10
ALLS
SOLVE

save

!Strain data collection
!Top inside
LSEL,S,,,3
NSLL,S
NLIST,ALL,,,COORD
PRNSOL,EPTO

Nsel,s,,,109389,109969,2
NLIST,ALL,,,COORD
PRNSOL,EPTO
ALLS
```

```
!Top outside
LSEL,S,,,107
NSLL,S
NLIST,ALL,,,COORD
PRNSOL,EPTO
ALLS

Nsel,s,,,1202,1782,2
NLIST,ALL,,,COORD
PRNSOL,EPTO
ALLS

!Top symmetry line
LSEL,S,,,329
NSLL,S
NLIST,ALL,,,COORD
PRNSOL,EPTO
ALLS

Nsel,s,,,17920,18498,2
NLIST,ALL,,,COORD
PRNSOL,EPTO
PRNSOL,U,COMP
ALLS

!Top inside mid line
LSEL,S,,,85
NSLL,S
NLIST,ALL,,,COORD
PRNSOL,EPTO

Nsel,s,,,142303,142881,2
NLIST,ALL,,,COORD
PRNSOL,EPTO
ALLS

!Top outside mid line
LSEL,S,,,290
NSLL,S
NLIST,ALL,,,COORD
PRNSOL,EPTO
ALLS

Nsel,s,,,4870,5450,2
NLIST,ALL,,,COORD
PRNSOL,EPTO
ALLS

!Bottom inside
LSEL,S,,,89
NSLL,S
NLIST,ALL,,,COORD
PRNSOL,EPTO
ALLS
```

```
!Bottom outside
LSEL,S,,,184
NSLL,S
NLIST,ALL,,,COORD
PRNSOL,EPTO
ALLS
```

8.2 Medium Bending Sample Holder ANSYS Code

```
! Load IGES file into ANSYS

/BATCH
/COM,ANSYS RELEASE 10.0    UP20050718       14:47:59    09/13/2011
/AUX15
IOPTN,IGES,NODEFEAT
!*
IOPTN,MERGE,YES
IOPTN,SOLID,YES
IOPTN,SMALL,NO
IOPTN,GTOLER, DEFA
IGESIN,'MB_half_ribs_no_fillets','IGS',' '
!*
FINISH

/PREP7
ASEL,S,,,267
ASEL,A,,,270,271
ASEL,A,,,387,395
VA,ALL
ALLS
ASEL,S,,,200,386
VA,ALL
alls
vplot

ET,1,SOLID95   !Define element type
MPTEMP,1,4   !Define a temperature table, 4K
!Define material properties for Ti-6Al-4V
MPDATA,EX,1,1,132591.5  !MPa
MPDATA,PRXY,1,1,.34  !Poisson's Ratio
TB,BISO,1
TBDATA,1,1758.16,17237
!Define material properties for SS316
MPDATA,EX,2,1,201397.5
MPDATA,PRXY,2,1,.33

!Glue volumes
ALLS
VGLUE,ALL
!Divide volumes to create axes of rotation
WPCSYS
ALLS
VSBW,ALL
WPCSYS
```

```
WPOFFS,-37.79139,-36.970 !Move WP to left bending arm
WPROTA,,,-90
VSBW,3
VSBW,4

!Apply Ti material properties to sample holder
VSEL,S,,,5,6
VATT,1

!Apply SS material properties to bending arms
VSEL,S,,,1,3
VSEL,A,,,7
VATT,2

alls
vplo

save

!Mesh all parts with tetrahedral elements
ALLS
MSHAPE,1,3D
SMRTSIZE,1
SMRTSIZE, ,0.1,1,1.3,7,15,1.4,0,1,4,0

!Select lines to refine mesh on volume 5
LSEL,S,,,6,12,2
LSEL,A,,,18,24,2
LSEL,A,,,78,84,2
LSEL,A,,,114,120,2
LSEL,A,,,150,156,2
LSEL,A,,,186,192,2
LSEL,A,,,222,228,2
LSEL,A,,,258,264,2
LSEL,A,,,294,300,2
LSEL,A,,,330,336,2
LSEL,A,,,366,372,2
LSEL,A,,,30
LSEL,A,,,46
LSEL,A,,,54,56,2
LSEL,A,,,60
LSEL,A,,,68,72,2
LSEL,A,,,90,378,36
LSEL,A,,,102,390,36
LSEL,A,,,104,392,36
LSEL,A,,,108,396,36
LESIZE,ALL,.1,,,,,,,1

LSEL,S,,,37,39
LSEL,A,,,816
LSEL,A,,,1100,1180,8
LSEL,A,,,1102,1182,8
LSEL,A,,,1114,1184,8
LSEL,A,,,1186
LSEL,A,,,1306
LSEL,A,,,1380
```

```
LSEL,A,,,1410
LSEL,A,,,2208,2892,76
LSEL,A,,,2228,2912,76
LSEL,A,,,2258,2942,76
LSEL,A,,,33,35
LSEL,A,,,824
LSEL,A,,,994
LSEL,A,,,1004,1084,8
LSEL,A,,,1006,1086,8
LSEL,U,,,1030
LSEL,A,,,1008,1088,8
LSEL,A,,,1300,1310,10
LSEL,A,,,1376
LSEL,A,,,1398
LSEL,A,,,2030
LSEL,A,,,2212,2224,12
LSEL,A,,,2246
LSEL,A,,,2288
LSEL,A,,,2322,2930,76
LSEL,A,,,2364,2896,76
LSEL,A,,,2376,2908,76
LSEL,A,,,1,3
LSEL,A,,,17,19,2
LSEL,A,,,834,838,4
LSEL,A,,,28,29
LSEL,A,,,31
LSEL,A,,,40
LSEL,A,,,41,45,2
LSEL,A,,,858,862,4
LESIZE,ALL,.2,,,,,,,1

ALLS
ASEL,S,,,1,22,7
AESIZE,ALL,.2,,,,,,,1

ALLS
VSEL,S,,,5
VMESH,5

ALLS

!Select lines to refine mesh on volume 6
LSEL,S,,,402,408,2
LSEL,A,,,414,420,2
LSEL,A,,,426,432,2
LSEL,A,,,454,778,36
LSEL,A,,,464,788,36
LSEL,A,,,466,790,36
LSEL,A,,,468,792,36
LSEL,A,,,474,762,36
LSEL,A,,,476,764,36
LSEL,A,,,478,766,36
LSEL,A,,,480,768,36
LESIZE,ALL,.1,,,,,,,1

LSEL,S,,,35,39,4
```

```
LSEL,A,,,47,49,2
LSEL,A,,,50,51
LSEL,A,,,812
LSEL,A,,,828
LSEL,A,,,896,976,8
LSEL,A,,,898,970,8
LSEL,A,,,900,972,8
LSEL,A,,,978,982,2
LSEL,A,,,1198
LSEL,A,,,1208,1288,8
LSEL,A,,,1210,1290,8
LSEL,A,,,1212,1292,8
LSEL,A,,,1318,1350,16
LSEL,A,,,1322,1354,16
LSEL,A,,,1436,1452,16
LSEL,A,,,1440,1456,16
LSEL,A,,,1470,2154,76
LSEL,A,,,1482,2166,76
LSEL,A,,,1512,2120,76
LSEL,A,,,1516,2124,76
LSEL,A,,,1528,2136,76
LSEL,A,,,1532,2140,76
LESIZE,ALL,.2,,,,,,1

ALLS
VSEL,S,,,6
VMESH,6

!Mesh remaining volumes
ALLS
VSEL,ALL
VSEL,U,,,5,6
VMESH,ALL

FINISH

!Define solution type
/SOLU
ANTYPE,STATIC
NLGEOM,ON                    !Specify large deflection
NROPT,FULL                   !Specify full Newton-Raphson option

NSUBST,20,200,0                    !Specify number of substeps
OUTRES,ALL,ALL                     !Write all data for all steps

!Fix axes
LSEL,S,,,58
NSLL,S
D,ALL,UX,0
D,ALL,UY,0
D,ALL,UZ,0
ALLS

!Apply symmetry boundary condition
ASEL,S,,,19,25,6
DA,ALL,SYMM
```

```
ALLS

!Keep bases in-plane
ASEL,S,,,2
ASEL,A,,,27,37,5
DA,ALL,UY,0
ALLS

!Apply displacement to outer line
LSEL,S,,,16
NSLL,S
D,ALL,UY,0
D,ALL,UZ,6.32              !WANT 32.64 mm DEFLECTION TOTAL FOR 0.6% BENDING
ALLS
SOLVE

!Second load step
LSEL,S,,,16
NSLL,S
DCUM,ADD
D,ALL,UZ,6.32
ALLS
SOLVE

!Second load step
LSEL,S,,,16
NSLL,S
DCUM,ADD
D,ALL,UZ,10
ALLS
SOLVE

!Third load step
LSEL,S,,,16
NSLL,S
DCUM,ADD
D,ALL,UZ,10
ALLS
SOLVE

save

!Strain data collection
!Top inside
LSEL,S,,,1198
NSLL,S
NLIST,ALL,,,COORD
PRNSOL,EPTO

Nsel,s,,,150067,150647,2
NLIST,ALL,,,COORD
PRNSOL,EPTO
ALLS

!Top outside
LSEL,S,,,1186
```

```
NSLL,S
NLIST,ALL,,,COORD
PRNSOL,EPTO
ALLS

Nsel,s,,,9445,10025,2
NLIST,ALL,,,COORD
PRNSOL,EPTO
ALLS

!Top middle of base
LSEL,S,,,39
NSLL,S
NLIST,ALL,,,COORD
PRNSOL,EPTO
ALLS

Nsel,s,,,1949,2529,2
NLIST,ALL,,,COORD
PRNSOL,EPTO
PRNSOL,U,COMP
ALLS
```

8.3 High Bending Sample Holder ANSYS Code – 0.6-1.0%

```
/BATCH
/COM,ANSYS RELEASE 10.0    UP20050718       14:47:59    09/13/2011
/AUX15
IOPTN,IGES,NODEFEAT
!*
IOPTN,MERGE,YES
IOPTN,SOLID,YES
IOPTN,SMALL,NO
IOPTN,GTOLER, DEFA
IGESIN,'HB_half_ribs_no_fillets','IGS',' '
!*
FINISH

/PREP7
ASEL,S,,,203,214
VA,ALL
ALLS
ASEL,S,,,214,404
ASEL,A,,,212
VA,ALL
alls
vplot

ET,1,SOLID95   !Define element type
MPTEMP,1,4   !Define a temperature table, 4K
!Define material properties for Ti-6Al-4V
MPDATA,EX,1,1,132591.5  !MPa
MPDATA,PRXY,1,1,.34  !Poisson's Ratio
TB,BISO,1
```

```
TBDATA,1,1758.16,17237
!Define material properties for SS316
MPDATA,EX,2,1,201397.5
MPDATA,PRXY,2,1,.33

!Glue volumes
ALLS
VGLUE,ALL
!Divide volumes to create axes of rotation
WPCSYS
ALLS
VSBW,ALL
WPCSYS
WPOFFS,-37.79139,-36.970 !Move WP to left bending arm
WPROTA,,,-90
VSBW,1
VSBW,4

!Apply Ti material properties to sample holder
VSEL,S,,,5,6
VATT,1

!Apply SS material properties to bending arms
VSEL,S,,,1,3
VSEL,A,,,7
VATT,2

alls
vplo

save

ALLS
MSHAPE,1,3D
SMRTSIZE,1
SMRTSIZE, ,0.1,1,1.3,7,15,1.4,0,1,4,0

LSEL,S,,,176,248,8
LSEL,A,,,352
LSEL,A,,,31
LSEL,A,,,364
LSEL,A,,,32
LSEL,A,,,468,540,8
LESIZE,ALL,.1,,,,,,1

LSEL,S,,,848,882,34
LSEL,A,,,1008,1118,110
LSEL,A,,,1120,1130,10
LSEL,A,,,1168
LSEL,A,,,3098,3100,2
LSEL,A,,,3112,3114,2
LSEL,A,,,3130,3168,38
LSEL,A,,,2192,2992,100
LSEL,A,,,2220,3020,100
LSEL,A,,,2244,3044,100
LSEL,A,,,2218,3018,100
```

```
LSEL,A,,,2234,3034,100
LSEL,A,,,2194,2994,100
LSEL,A,,,874,876,2
LSEL,A,,,1014,1016,2
LSEL,A,,,1112,1114,2
LSEL,A,,,1134,1144,10
LSEL,A,,,3092,3094,2
LSEL,A,,,3118,3120,2
LSEL,A,,,3134,3144,10
LSEL,A,,,2200,3000,100
LSEL,A,,,2212,3012,100
LSEL,A,,,2268,3068,100
LSEL,A,,,2214,3014,100
LSEL,A,,,2230,3030,100
LSEL,A,,,2198,2998,100
LESIZE,ALL,.2,,,,,,,1

ALLS
ASEL,S,,,24
AESIZE,ALL,.1,,,,,,,1

ALLS
VSEL,S,,,6
VMESH,6

ALLS
LSEL,S,,,260,340,8
LSEL,A,,,376,456,8
LESIZE,ALL,.1,,,,,,,1

LSEL,S,,,818,820,2
LSEL,A,,,824,826,2
LSEL,A,,,1002,1004,2
LSEL,A,,,1032,1034,2
LSEL,A,,,1050,1064,14
LSEL,A,,,1020,1022,2
LSEL,A,,,1038,1040,2
LSEL,A,,,1054,1088,34
LSEL,A,,,1220,2120,100
LSEL,A,,,1192,2092,100
LSEL,A,,,1244,2144,100
LSEL,A,,,1194,2094,100
LSEL,A,,,1230,2130,100
LSEL,A,,,1218,2118,100
LSEL,A,,,1212,2112,100
LSEL,A,,,1200,2100,100
LSEL,A,,,1268,2168,100
LSEL,A,,,1198,2098,100
LSEL,A,,,1234,2134,100
LSEL,A,,,1214,2114,100
LESIZE,ALL,.2,,,,,,,1

ALLS
ASEL,S,,,20
AESIZE,ALL,.1,,,,,,,1
```

```
ALLS
VSEL,S,,,5
VMESH,5

!Mesh remaining volumes
ALLS
VSEL,ALL
VSEL,U,,,5,6
VMESH,ALL

FINISH

!Define solution type
/SOLU
ANTYPE,STATIC
NLGEOM,ON                    !Specify large deflection
NROPT,FULL                   !Specify full Newton-Raphson option

NSUBST,20,500,1                    !Specify number of substeps
OUTRES,ALL,ALL                     !Write all data for all steps

!Fix axes
LSEL,S,,,46
NSLL,S
D,ALL,UX,0
D,ALL,UY,0
D,ALL,UZ,0
ALLS

!Apply symmetry boundary condition
ASEL,S,,,19,22,3
DA,ALL,SYMM
ALLS

!Keep bases in-plane
ASEL,S,,,1,4,3
ASEL,A,,,28,33,5
DA,ALL,UY,0
ALLS

!Apply displacement to outer line
LSEL,S,,,17
NSLL,S
D,ALL,UY,0
D,ALL,UZ,6.32          !WANT 32.64 mm DEFLECTION TOTAL FOR 0.6% BENDING
ALLS
SOLVE

!Second load step
LSEL,S,,,17
NSLL,S
DCUM,ADD
D,ALL,UZ,6.32
ALLS
SOLVE
```

```
!Third load step
LSEL,S,,,17
NSLL,S
DCUM,ADD
D,ALL,UZ,10
ALLS
SOLVE

!Fourth load step ----------------- 0.6%
LSEL,S,,,17
NSLL,S
DCUM,ADD
D,ALL,UZ,10
ALLS
SOLVE


!Fifth load step ----------------- 1.0%
LSEL,S,,,17
NSLL,S
DCUM,ADD
D,ALL,UZ,10.25
ALLS
SOLVE

save

!Strain data collection
!Top outside channel
LSEL,S,,,176,248,8
LSEL,A,,,352
NSLL,S
NLIST,ALL,,,COORD
PRNSOL,EPTO
ALLS

!Top outside ribs
LSEL,S,,,180,252,8
LSEL,A,,,356
NSLL,S
NLIST,ALL,,,COORD
PRNSOL,EPTO
ALLS

NSEL,S,,,3740,3842,2
NSEL,A,,,3880,3982,2
NSEL,A,,,4020,4122,2
NSEL,A,,,4156,4258,2
NSEL,A,,,4292,4386,2
NSEL,A,,,4414,4516,2
NSEL,A,,,4550,4652,2
NSEL,A,,,4674,4768,2
NSEL,A,,,4771,4873,2
NSEL,A,,,3880,3982,2
NSEL,A,,,4911,5013,2
NSEL,A,,,5222,5318,2
```

```
NSEL,A,,,3845,3877,2
NSEL,A,,,3985,4017,2
NSEL,A,,,4125,4153,2
NSEL,A,,,4261,4289,2
NSEL,A,,,4389,4411,2
NSEL,A,,,4519,4547,2
NSEL,A,,,4655,4671,2
NSEL,A,,,4876,4908,2
NSEL,A,,,5016,5030,2
NSEL,A,,,5321,5353,2
NSEL,A,,,21706,21724,2
NLIST,ALL,,,COORD
PRNSOL,EPTO
PRNSOL,U,COMP
ALLS

!Top middle of base
LSEL,S,,,31
NSLL,S
NLIST,ALL,,,COORD
PRNSOL,EPTO
ALLS

NSEL,S,,,259,1879,2
NLIST,ALL,,,COORD
PRNSOL,EPTO
PRNSOL,U,COMP
ALLS

!Top inside
LSEL,S,,,260,340,8
NSLL,S
NLIST,ALL,,,COORD
PRNSOL,EPTO
ALLS

NSEL,S,,,148541,148643,2
NSEL,A,,,148681,148783,2
NSEL,A,,,148821,148923,2
NSEL,A,,,148957,149059,2
NSEL,A,,,149093,149195,2
NSEL,A,,,149275,149369,2
NSEL,A,,,149397,149499,2
NSEL,A,,,149533,149629,2
NSEL,A,,,158329,158413,2
NSEL,A,,,158418,158502,2
NSEL,A,,,158507,158591,2
NLIST,ALL,,,COORD
PRNSOL,EPTO
PRNSOL,U,COMP
ALLS

LSEL,S,,,256,336,8
NSLL,S
NLIST,ALL,,,COORD
PRNSOL,EPTO
```

```
ALLS

NSEL,S,,,148524,148538,2
NSEL,A,,,148646,148678,2
NSEL,A,,,148786,148818,2
NSEL,A,,,148926,148954,2
NSEL,A,,,149062,149090,2
NSEL,A,,,149198,149226,2
NSEL,A,,,149229,149249,2
NSEL,A,,,149252,149272,2
NSEL,A,,,149372,149394,2
NSEL,A,,,149502,149530,2
NSEL,A,,,158595,158613,2
NLIST,ALL,,,COORD
PRNSOL,EPTO
PRNSOL,U,COMP
ALLS
```

8.4 High Bending Sample Holder ANSYS Code – 1.4%

```
/BATCH
/COM,ANSYS RELEASE 10.0    UP20050718       14:47:59    09/13/2011
/AUX15
IOPTN,IGES,NODEFEAT
!*
IOPTN,MERGE,YES
IOPTN,SOLID,YES
IOPTN,SMALL,NO
IOPTN,GTOLER, DEFA
IGESIN,'HB_half_ribs_no_fillets','IGS',' '
!*
FINISH

/PREP7
ASEL,S,,,203,214
VA,ALL
ALLS
ASEL,S,,,214,404
ASEL,A,,,212
VA,ALL
alls
vplot

ET,1,SOLID95   !Define element type
MPTEMP,1,4   !Define a temperature table, 4K
!Define material properties for Ti-6Al-4V
MPDATA,EX,1,1,132591.5  !MPa
MPDATA,PRXY,1,1,.34  !Poisson's Ratio
TB,BISO,1
TBDATA,1,1758.16,17237
!Define material properties for SS316
MPDATA,EX,2,1,201397.5
MPDATA,PRXY,2,1,.33
```

```
!Glue volumes
ALLS
VGLUE,ALL
!Divide volumes to create axes of rotation
WPCSYS
ALLS
VSBW,ALL
WPCSYS
WPOFFS,-37.79139,-36.970 !Move WP to left bending arm
WPROTA,,,-90
VSBW,1
VSBW,4

!Apply Ti material properties to sample holder
VSEL,S,,,5,6
VATT,1

!Apply SS material properties to bending arms
VSEL,S,,,1,3
VSEL,A,,,7
VATT,2

alls
vplo

save

ALLS
MSHAPE,1,3D
SMRTSIZE,1
SMRTSIZE, ,0.1,1,1.3,7,15,1.4,0,1,4,0

LSEL,S,,,176,248,8
LSEL,A,,,352
LSEL,A,,,31
LSEL,A,,,364
LSEL,A,,,32
LSEL,A,,,468,540,8
LESIZE,ALL,.1,,,,,,,1

LSEL,S,,,848,882,34
LSEL,A,,,1008,1118,110
LSEL,A,,,1120,1130,10
LSEL,A,,,1168
LSEL,A,,,3098,3100,2
LSEL,A,,,3112,3114,2
LSEL,A,,,3130,3168,38
LSEL,A,,,2192,2992,100
LSEL,A,,,2220,3020,100
LSEL,A,,,2244,3044,100
LSEL,A,,,2218,3018,100
LSEL,A,,,2234,3034,100
LSEL,A,,,2194,2994,100
LSEL,A,,,874,876,2
LSEL,A,,,1014,1016,2
LSEL,A,,,1112,1114,2
```

```
LSEL,A,,,1134,1144,10
LSEL,A,,,3092,3094,2
LSEL,A,,,3118,3120,2
LSEL,A,,,3134,3144,10
LSEL,A,,,2200,3000,100
LSEL,A,,,2212,3012,100
LSEL,A,,,2268,3068,100
LSEL,A,,,2214,3014,100
LSEL,A,,,2230,3030,100
LSEL,A,,,2198,2998,100
LESIZE,ALL,.2,,,,,,,1

ALLS
ASEL,S,,,24
AESIZE,ALL,.1,,,,,,,1

ALLS
VSEL,S,,,6
VMESH,6

ALLS
LSEL,S,,,260,340,8
LSEL,A,,,376,456,8
LESIZE,ALL,.1,,,,,,,1

LSEL,S,,,818,820,2
LSEL,A,,,824,826,2
LSEL,A,,,1002,1004,2
LSEL,A,,,1032,1034,2
LSEL,A,,,1050,1064,14
LSEL,A,,,1020,1022,2
LSEL,A,,,1038,1040,2
LSEL,A,,,1054,1088,34
LSEL,A,,,1220,2120,100
LSEL,A,,,1192,2092,100
LSEL,A,,,1244,2144,100
LSEL,A,,,1194,2094,100
LSEL,A,,,1230,2130,100
LSEL,A,,,1218,2118,100
LSEL,A,,,1212,2112,100
LSEL,A,,,1200,2100,100
LSEL,A,,,1268,2168,100
LSEL,A,,,1198,2098,100
LSEL,A,,,1234,2134,100
LSEL,A,,,1214,2114,100
LESIZE,ALL,.2,,,,,,,1

ALLS
ASEL,S,,,20
AESIZE,ALL,.1,,,,,,,1

ALLS
VSEL,S,,,5
VMESH,5

!Mesh remaining volumes
```

```
ALLS
VSEL,ALL
VSEL,U,,,5,6
VMESH,ALL

ET,2,170
ET,3,174
KEYOPT,3,12,5
KEYOPT,3,4,2
KEYOPT,3,2,2
KEYOPT,2,2,0
KEYOPT,2,4,111111
TYPE,2

KSEL,S,,,14
KMESH,14

ASEL,S,,,1,4,3
ASEL,A,,,28,33,5
TYPE,3
NSLA,S,1
ESLN,S,0
ESURF
ALLS

SAVE

FINISH

!Define solution type
/SOLU
ANTYPE,STATIC
NLGEOM,ON                !Specify large deflection
NROPT,FULL               !Specify full Newton-Raphson option

NSUBST,20,500,1                  !Specify number of substeps
OUTRES,ALL,ALL                   !Write all data for all steps

!Apply symmetry boundary condition
ASEL,S,,,19,22,3
DA,ALL,SYMM
ALLS

NSEL,S,,,288702
D,ALL,UX,0
D,ALL,UY,O
D,ALL,UZ,0
D,ALL,ROTX,0
D,ALL,ROTY,.25                   ! Applying 1.4% (1.99 radians), step 1 of 8
D,ALL,ROTZ,0
ALLS

SOLVE

!Second load step
NSEL,S,,,288702
```

```
DCUM,ADD
D,ALL,ROTY,.25                  !Applying 1.4% (1.99 radians), step 2 of 8
ALLS
SOLVE

!Third load step
NSEL,S,,,288702
DCUM,ADD
D,ALL,ROTY,.25                  !Applying 1.4% (1.99 radians), step 3 of 8
ALLS
SOLVE

!Fourth load step
NSEL,S,,,288702
DCUM,ADD
D,ALL,ROTY,.25                  !Applying 1.4% (1.99 radians), step 4 of 8
ALLS
SOLVE

!Fifth load step
NSEL,S,,,288702
DCUM,ADD
D,ALL,ROTY,.25                  !Applying 1.4% (1.99 radians), step 5 of 8
ALLS
SOLVE

!Sixth load step
NSEL,S,,,288702
DCUM,ADD
D,ALL,ROTY,.25                  !Applying 1.4% (1.99 radians), step 6 of 8
ALLS
SOLVE

!Seventh load step
NSEL,S,,,288702
DCUM,ADD
D,ALL,ROTY,.25                  !Applying 1.4% (1.99 radians), step 7 of 8
ALLS
SOLVE

!Eighth load step
NSEL,S,,,288702
DCUM,ADD
D,ALL,ROTY,.24                  !Applying 1.4% (1.99 radians), step 8 of 8
ALLS
SOLVE

save

!Strain data collection
!Top outside channel
LSEL,S,,,176,248,8
LSEL,A,,,352
NSLL,S
NLIST,ALL,,,COORD
PRNSOL,EPTO
```

```
ALLS

!Top outside ribs
LSEL,S,,,180,252,8
LSEL,A,,,356
NSLL,S
NLIST,ALL,,,COORD
PRNSOL,EPTO
ALLS

NSEL,S,,,3740,3842,2
NSEL,A,,,3880,3982,2
NSEL,A,,,4020,4122,2
NSEL,A,,,4156,4258,2
NSEL,A,,,4292,4386,2
NSEL,A,,,4414,4516,2
NSEL,A,,,4550,4652,2
NSEL,A,,,4674,4768,2
NSEL,A,,,4771,4873,2
NSEL,A,,,3880,3982,2
NSEL,A,,,4911,5013,2
NSEL,A,,,5222,5318,2
NSEL,A,,,3845,3877,2
NSEL,A,,,3985,4017,2
NSEL,A,,,4125,4153,2
NSEL,A,,,4261,4289,2
NSEL,A,,,4389,4411,2
NSEL,A,,,4519,4547,2
NSEL,A,,,4655,4671,2
NSEL,A,,,4876,4908,2
NSEL,A,,,5016,5030,2
NSEL,A,,,5321,5353,2
NSEL,A,,,21706,21724,2
NLIST,ALL,,,COORD
PRNSOL,EPTO
PRNSOL,U,COMP
ALLS

!Top middle of base
LSEL,S,,,31
NSLL,S
NLIST,ALL,,,COORD
PRNSOL,EPTO
ALLS

NSEL,S,,,259,1879,2
NLIST,ALL,,,COORD
PRNSOL,EPTO
PRNSOL,U,COMP
ALLS

!Top inside
LSEL,S,,,260,340,8
NSLL,S
NLIST,ALL,,,COORD
PRNSOL,EPTO
```

```
ALLS

NSEL,S,,,148541,148643,2
NSEL,A,,,148681,148783,2
NSEL,A,,,148821,148923,2
NSEL,A,,,148957,149059,2
NSEL,A,,,149093,149195,2
NSEL,A,,,149275,149369,2
NSEL,A,,,149397,149499,2
NSEL,A,,,149533,149629,2
NSEL,A,,,158329,158413,2
NSEL,A,,,158418,158502,2
NSEL,A,,,158507,158591,2
NLIST,ALL,,,COORD
PRNSOL,EPTO
PRNSOL,U,COMP
ALLS

LSEL,S,,,256,336,8
NSLL,S
NLIST,ALL,,,COORD
PRNSOL,EPTO
ALLS

NSEL,S,,,148524,148538,2
NSEL,A,,,148646,148678,2
NSEL,A,,,148786,148818,2
NSEL,A,,,148926,148954,2
NSEL,A,,,149062,149090,2
NSEL,A,,,149198,149226,2
NSEL,A,,,149229,149249,2
NSEL,A,,,149252,149272,2
NSEL,A,,,149372,149394,2
NSEL,A,,,149502,149530,2
NSEL,A,,,158595,158613,2
NLIST,ALL,,,COORD
PRNSOL,EPTO
PRNSOL,U,COMP
ALLS
```

9. REFERENCES

[1] J. Eck, “The History of Superconductors.” Available: http://www.superconductors.org/History.htm, Dec. 2011. [Mar. 2012].

[2] J. Bardeen, L. N. Cooper, J. R. Schrieffer, “Theory of Superconductivity,” Physical Review, v108, n5, Dec. 1957, p1175-1204.

[3] “Fundamentals of Superconductors.” Available: http://www.ornl.gov/info/reports/m/ornlm3063r1/pt3.html, Apr. 1, 1996. [Mar. 2012].

[4] “AC Loss and Stability of Superconducting Cables.” Available: http://www.utwente.nl/tnw/ems/Research/AC%20loss%20Twente%20Press/AC_loss_and_stability_of_superconducting_cables_for_fusion.docx/, Jan., 31 2012. [Mar 2012].

[5] P. Hoffman, “Superconductivity.” Available: http://users-phys.au.dk/philip/pictures/physicsfigures/node12.html, Mar. 12, 2009. [Mar. 2012]

[6] K. Dulon, “From 100 kg billets to millimeter-thin strand.” Available: http://www.iter.org/newsline/140/340, July 15, 2010. [Mar. 2012].

[7] ITER website, http://www.iter.org/. [Mar. 2012].

[8] A. Nijhuis, et al. “Impact of Spatial Periodic Bending and Load Cycling on the Critical Current of a Nb_3Sn Strand,” Superconductor Science and Technology, v18, n12, Nov. 2005, pS273-S283.

[9] Harris, D. “Characterization of Nb3Sn Superconducting Strand Under Pure Bending” Massachusetts Institute of Technology Master Thesis, September 2005.

[10] Allegritti, A. “Sviluppo E Speriment Azione Di Un Dispositivo Per La Misura Della Corrente Critica Di Fili Superconduttori In Condizioni Di Pura Flessione” Universita’ Degli Studi Di Bologna Bachelors Thesis, 2006.

[11] Mallon, P. “Characterization of Nb_3Sn Superconducting Strands under Wide Range Pure-Bending Strain,” Tufts University Master Thesis, November 2011.